Crystal engineering in functionalized materials: From fundamentals to applications

by

Kelly Nzwanai Shunje

B.S., Cape Peninsula University of Technology, 2015
M.S., Cape Peninsula University of Technology, 2017

AN ABSTRACT OF A DISSERTATION

submitted in partial fulfillment of the requirements for the degree

DOCTOR OF PHILOSOPHY

Department of Chemistry
College of Arts and Sciences

KANSAS STATE UNIVERSITY
Manhattan, Kansas

2023

Abstract

The carbamate-bearing molecules and their derivatives are versatile compounds for crystal engineering because they contain multiple acceptor and donor sites for directional intermolecular interactions. In order to better understand the structural landscape of the carbamate functionality, two thiazole-based carbamate families (each with five members), R((2-thiazoyl)carbamothioyl)carbamate (**1**) and R((2-thiazoyl-5-methyl)carbamothioyl)carbamate (R=methyl>hexyl) (**2**) were synthesized as described in Chapter 2. We examined (i) the effect of increasing chain length (R=methyl>hexyl), and (ii) the effect of adding a methyl substituent on the thiazole ring on molecular packing. For series **1** the targets interact via (carbamate)N-H---N(thiazole) forming infinite chains and molecules pack by aggregating into hydrophobic layers with alkyl chains facing each other and pi-stacked layers of the thiazole rings. Addition of a methyl substituent on the thiazole ring in series **2** resulted in similar H-bonding and packing pattern from methyl to isobutyl. However, for longer pentyl and hexyl chains, the N–H---S=C dimer formed but the packing has alternating stacks of alkyl chains facing each other and thiazole rings facing each other.

In Chapter 3, the structural influence of hydrogen bonding on structure was explored using diethyl *N*,*N*′-[(1,4-phenylenedicarbamothioyl)bis(carbamate)] (**14thiol**) as a core because it possesses various hydrogen bond donor and acceptor sites. Co-crystallization experiments were conducted using pyridine-based co-formers and two polymorphs, one dioxane solvate, three co-crystals and one co-crystal solvate (THF) were

obtained. Introduction of pyridine-based co-formers disrupted the robust homomeric N–H---S=C and N–H---O=C H-bonded dimers in **14thiol** with the formation of heteromeric N-H---N bonded co-crystals. Hirshfeld surface analysis was conducted to give insights into the nature of interactions, and it revealed that the high acceptor ability in the co-formers led to the increase in H-bonding interactions (N-H---N) and a decrease in (O---H) contacts in **14thiol** co-crystals. Molecular geometry analysis showed how the target was able to adopt several molecular conformations in order to accommodate various co-formers thus yielding multicomponent solid forms.

In Chapter 4, we investigated how the presence of multiple intermolecular interaction sites influence the heteromeric supramolecular assembly of three R-*N*-[(3-pyridinylamino) thioxomethyl] carbamates (R= methyl, ethyl, and isobutyl) with fluoroiodobenzenes. Three targets were synthesized and crystallized resulting in three parent structures, five co-crystals and one co-crystal solvate. MEP surfaces were employed to rank the relative importance of the binding sites (Npyr > C=S > C=O) in order to predict the dominant interactions. The N-H---H hydrogen bond (parent synthon) was replaced by I---Npyr in 3/6 cases by I---C=S in 4/6 cases and by I---O=C in one case. Interestingly, in two cases, the I---C=S halogen bond coexisted with I---Npyr and I---O=C halogen bonds. Overall, the MEPs were fairly reliable for predicting co-crystallization outcomes. Halogen-bond donors co-formers proved to be structurally competitive for acceptor sites even in the presence of strong hydrogen-bond donors.

To investigate structure-property relationships in carbamates, Chapter 5, the ability to control thermal expansion (TE) behavior in solid state materials was studied. We examined (i) the effect of intermolecular interactions and molecular packing, and (ii) the effect of varying molecular dimensions (di->tri->tetra) carbamate on TE. Five targets were designed and synthesized: three fluorinated dicarbamates with varying chain lengths, one tri-carbamate and one tetra-carbamate. A series of detailed SCXRD structural determinations at 20-K intervals (150-250) allowed us to analyze the thermal expansion at molecular level. All five targets showed TE and the lower dimensional dicarbamates exhibited the highest TE. The specific influence of intermolecular interactions was explored based on interaction energies (IEs) using energy framework analysis which confirmed that IEs were highest along the direction of the robust N-H---O=C interactions which subsequently restricted thermal expansion along those directions.

Finally, in Chapter 6, specific applications of crystal engineering were explored using hydrogen-bonded organic frameworks (HOF) as molecular containers/hosts for volatile fragrance compounds (cinnamyl alcohol and α-terpineol). In the first case, the HOF successfully captured α-terpineol in its pores via physical encapsulation, as indicated by thermal gravimetric analysis. In the second case, the HOF also captured cinnamyl alcohol by way of H-bonding to the volatile guest compound. We demonstrated that this supramolecular framework, based on trimesic acid, is very suitable for capture and slow release of volatile compounds.

Crystal engineering in functionalized materials: From fundamentals to applications

by

Kelly Nzwanai Shunje

B.S., Cape Peninsula University of Technology, 2015
M.S., Cape Peninsula University of Technology, 2017

A DISSERTATION

submitted in partial fulfillment of the requirements for the degree

DOCTOR OF PHILOSOPHY

Department of Chemistry
College of Arts and Sciences

KANSAS STATE UNIVERSITY
Manhattan, Kansas

2023

Approved by:

Major Professor

Dr. Christer B Aakeröy

Copyright

Abstract

The carbamate-bearing molecules and their derivatives are versatile compounds for crystal engineering because they contain multiple acceptor and donor sites for directional intermolecular interactions. In order to better understand the structural landscape of the carbamate functionality, two thiazole-based carbamate families (each with five members), R((2-thiazoyl)carbamothioyl)carbamate (**1**) and R((2-thiazoyl-5-methyl)carbamothioyl)carbamate (R=methyl>hexyl) (**2**) were synthesized as described in Chapter 2. We examined (i) the effect of increasing chain length (R=methyl>hexyl), and (ii) the effect of adding a methyl substituent on the thiazole ring on molecular packing. For series **1** the targets interact via (carbamate)N-H---N(thiazole) forming infinite chains and molecules pack by aggregating into hydrophobic layers with alkyl chains facing each other and pi-stacked layers of the thiazole rings. Addition of a methyl substituent on the thiazole ring in series **2** resulted in similar H-bonding and packing pattern from methyl to isobutyl. However, for longer pentyl and hexyl chains, the N–H---S=C dimer formed but the packing has alternating stacks of alkyl chains facing each other and thiazole rings facing each other.

In Chapter 3, the structural influence of hydrogen bonding on structure was explored using diethyl *N*,*N*′-[(1,4-phenylenedicarbamothioyl)bis(carbamate)] (**14thiol**) as a core because it possesses various hydrogen bond donor and acceptor sites. Co-crystallization experiments were conducted using pyridine-based co-formers and two polymorphs, one dioxane solvate, three co-crystals and one co-crystal solvate (THF) were

obtained. Introduction of pyridine-based co-formers disrupted the robust homomeric N–H---S=C and N–H---O=C H-bonded dimers in **14thiol** with the formation of heteromeric N-H---N bonded co-crystals. Hirshfeld surface analysis was conducted to give insights into the nature of interactions, and it revealed that the high acceptor ability in the co-formers led to the increase in H-bonding interactions (N-H---N) and a decrease in (O---H) contacts in **14thiol** co-crystals. Molecular geometry analysis showed how the target was able to adopt several molecular conformations in order to accommodate various co-formers thus yielding multicomponent solid forms.

In Chapter 4, we investigated how the presence of multiple intermolecular interaction sites influence the heteromeric supramolecular assembly of three R-*N*-[(3-pyridinylamino) thioxomethyl] carbamates (R= methyl, ethyl, and isobutyl) with fluoroiodobenzenes. Three targets were synthesized and crystallized resulting in three parent structures, five co-crystals and one co-crystal solvate. MEP surfaces were employed to rank the relative importance of the binding sites (Npyr > C=S > C=O) in order to predict the dominant interactions. The N-H---H hydrogen bond (parent synthon) was replaced by I---Npyr in 3/6 cases by I---C=S in 4/6 cases and by I---O=C in one case. Interestingly, in two cases, the I---C=S halogen bond coexisted with I---Npyr and I---O=C halogen bonds. Overall, the MEPs were fairly reliable for predicting co-crystallization outcomes. Halogen-bond donors co-formers proved to be structurally competitive for acceptor sites even in the presence of strong hydrogen-bond donors.

To investigate structure-property relationships in carbamates, Chapter 5, the ability to control thermal expansion (TE) behavior in solid state materials was studied. We examined (i) the effect of intermolecular interactions and molecular packing, and (ii) the effect of varying molecular dimensions (di->tri->tetra) carbamate on TE. Five targets were designed and synthesized: three fluorinated dicarbamates with varying chain lengths, one tri-carbamate and one tetra-carbamate. A series of detailed SCXRD structural determinations at 20-K intervals (150-250) allowed us to analyze the thermal expansion at molecular level. All five targets showed TE and the lower dimensional dicarbamates exhibited the highest TE. The specific influence of intermolecular interactions was explored based on interaction energies (IEs) using energy framework analysis which confirmed that IEs were highest along the direction of the robust N-H---O=C interactions which subsequently restricted thermal expansion along those directions.

Finally, in Chapter 6, specific applications of crystal engineering were explored using hydrogen-bonded organic frameworks (HOF) as molecular containers/hosts for volatile fragrance compounds (cinnamyl alcohol and α-terpineol). In the first case, the HOF successfully captured α-terpineol in its pores via physical encapsulation, as indicated by thermal gravimetric analysis. In the second case, the HOF also captured cinnamyl alcohol by way of H-bonding to the volatile guest compound. We demonstrated that this supramolecular framework, based on trimesic acid, is very suitable for capture and slow release of volatile compounds.

Table of Contents

List of Figures

List of Tables

Acknowledgements

I would like to express my deepest gratitude to my advisor and mentor, Professor Christer Aakeröy for his patience, encouragement, and support. Thank you for providing a kind and supportive environment, you made the group a family! I always felt that I could walk to your office for help without hesitation. I am grateful for the countless hours and effort you dedicated to making me a better individual both in and outside the lab.

I would like to thank my committee members Dr. Tendai Gadzikwa, Dr. David Poole, and Dr. Christine Aikens for their valuable time and constructive feedback.

I am also grateful to Dr. Boris Averkiev, Dr. Abhijeet Sinha, Dr. Victor Day and Dr. Christer Aakeröy for collecting my crystal structure data and solving them, without your efforts this work would not be complete. Specifically, I want to thank Dr. Boris Averkiev for devoting his valuable time and effort to making sure that all structures were collected and solved on time.

I am tremendously grateful to the current and past members of my group for their friendship and peer motivation, I will always cherish the moments we shared. I would like to acknowledge the Chemistry department staff, and the graduate school, at Kansas State University for making my research life smooth at K-State.

Finally, I want to thank my family and friends for their endless love and support. I would like to thank my Church family for their love and for being a family away from home. To my village, thank you for believing in me and cheering me on. Specially, I want

to thank my mom and partner, Kudzi. I would not be where I am without your support, encouragement, and endless love.

Dedication

To my village!

For their continuous support and believing in me….

Preface

Research carried out at Kansas State University for this dissertation led to the following publications in scientific journals.

Shunje, K.N.; Averkiev, B.B.; Aakeröy, C.B. Influence of Multiple Binding Sites on the Supramolecular Assembly of N-[(3-pyridinylamino) Thioxomethyl] Carbamates. *Molecules* 2022, 27, 3685. https://doi.org/10.3390/molecules27123685

Aakeröy, C.B.; **Shunje, K.N**, Supramolecular Porous Organic Frameworks for Storage and Delivery of Volatile Guests. **U.S. Provisional Patent** application No: 63/349,359. Filed June 6, 2022.

Shunje, K.N.; Averkiev, B.B.; Aakeröy, C.B. Modulating thermal expansion by fine-tuning the molecular dimensions and number of functional groups in alkyl carbamate molecules, under preparation.

Shunje, K.N.; Sinha, A.S.; Aakeröy, C.B. The interplay between electrostatics and molecular geometry in Diethyl *N*,*N*′-[1,4-phenylenebis(iminocarbonothioyl)] bis[carbamate] multicomponent solid forms, under preparation.

Chapter 1 - Introduction

1.1.Supramolecular Chemistry

Supramolecular chemistry is widely known as the chemistry beyond the molecule. The genesis of supramolecular chemistry can be traced back to the 1800s when Sir Humphry Davy discovered the inclusion compound chlorine hydrate, and some significant milestones in the field have been summarised by Steed and Atwood in 'Supramolecular Chemistry'.[1] Despite the prior existence of supramolecular chemistry, it did not gain attention in chemical research until the discovery of crown ethers by Donald J. Cram, Jean-Marie Lehn and Charles J. Pedersen who were awarded a Nobel Prize in chemistry in 1987 for their work. The term 'supramolecular chemistry', was officially defined by Jean-Marie Lehn, as the chemistry of molecular assemblies and of the intermolecular bond.[2] Supramolecular chemistry focuses on the design and synthesis of functional materials using non-covalent interactions of well-defined subunits.[3] This utilization of non-covalent synthesis of target molecules in supramolecular chemistry is what differentiates it from covalent synthesis which involves formation of covalent bonds in synthesizing target molecules (Figure 1-1).

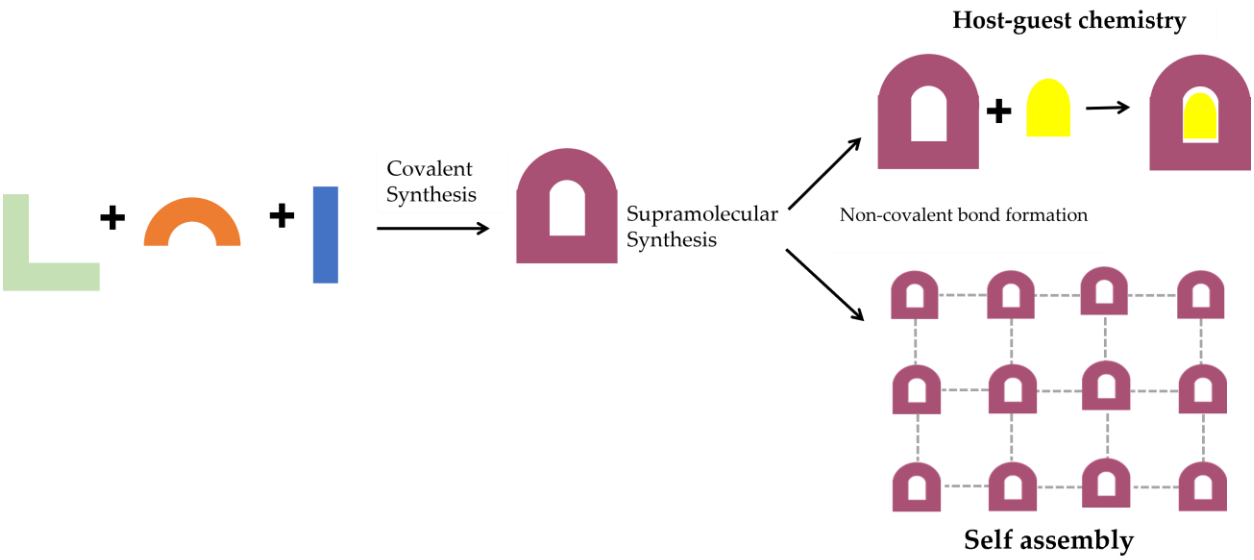

Figure 1-1 Covalent vs non-covalent synthesis

Supramolecular chemistry can be divided into two classes, i.e. host-guest chemistry and self-assembly. The latter is achieved and maintained through interaction of molecules which are relatively of the same size via non-covalent interactions such as hydrogen bonding[4-8], halogen bonding[9-12], dipole-dipole interactions[13, 14], and π-π interactions.[15, 16] On the other hand, in host-guest chemistry molecules still connect via non-covalent interactions but there is a significant difference in the size and shape of the host and guest molecules. Typically, the host molecule is larger and can wrap around the smaller molecule, the guest, which becomes enclosed.[17]

1.1.1. Molecular recognition and self-assembly

In molecular recognition, molecules interact with complementary functional groups using non-covalent intermolecular interactions in an organized manner.

Complementarity is well demonstrated by the 'lock and key' principle.[18] Most biological systems are driven by molecular recognition and self-assembly. Another example of self-assembly is the antibiotic vancomycin (Figure 1-2) that selectively binds with terminal D-Ala-D-Ala dipeptide in bacterial cells through hydrogen bonding along with hydrophobic forces and van der Waals forces.[19] Vancomycin is lethal to the bacteria and upon binding to the peptides it hinders the activity and construction of the bacteria's cell wall.

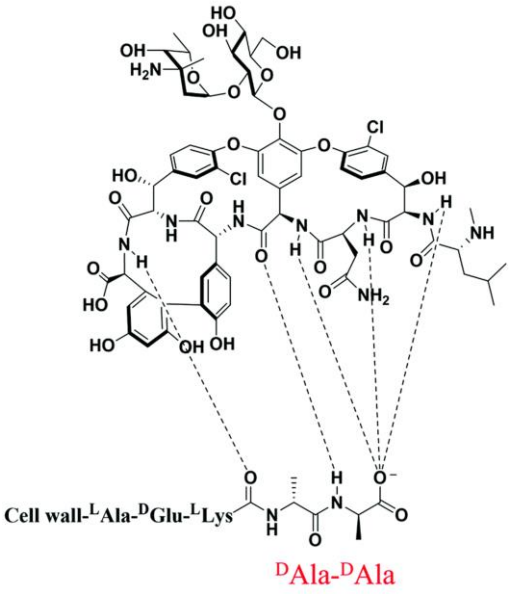

Figure 1-2 Molecular recognition and self-assembly in vancomycin and dipeptide via five H-bonds.

1.1.2. Host guest chemistry

The pioneering work of supramolecular host was a crown ether which was synthesized by Lehn and co-workers.[2] Subsequently, more inclusion compounds/ supramolecular

hosts have been discovered such as calixarenes[20], cavitands[21, 22], and cyclodextrins[23], and curcubiturils.[24] Most inclusion compounds contain pre-organized binding cavities and as such, the host compounds have high affinity and binding selectivity and non-covalent interactions play role as the driving forces for molecular recognition. Examples of different host-guest binding via non-covalent interactions are shown in (Figure 1-3).[25-27]

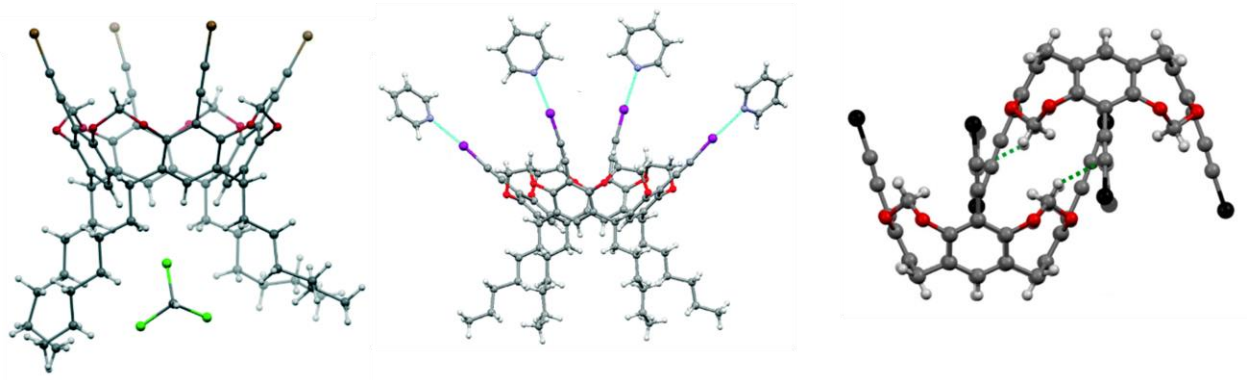

Figure 1-3 Host guest binding via non-covalent interactions C-H---Cl, I---N, and C-H---π.

1.2. Crystal engineering

Crystal engineering focuses on design and synthesis of predictable and controllable crystalline materials based on knowledge of known structures of the building blocks. Desiraju defined crystal engineering as "*the understanding of intermolecular interactions in the context of crystal packing and in the utilization of such understanding in the design of new solids with desired physical and chemical properties*".[28] In order to achieve predictable structure-property relationships in materials, it is imperative to study the arrangement of molecules in solid-state and understand how to manipulate and deliberately control

materials properties. Crystal engineering covers a wide array of scientific disciplines from the synthesis of smart materials,[29] gas storage,[30] organocatalysis,[31] to pharmaceutics.[32]

1.3.Non-covalent intermolecular interactions

Crystalline materials can be held together in a crystal lattice by different types of non-covalent interactions; either repulsive or attractive in nature.[33] The non-covalent molecular forces (intermolecular interactions) are mainly electrostatic in nature. Their general properties are dependent on strength, direction, and distance.

1.3.1. Hydrogen bonding

The hydrogen bond is defined as an *"….attractive interaction between a proton donor and a proton acceptor in the same or different molecules…"*.[8] The donor atom (D) is covalently bonded to the hydrogen atom (H) and has a high electronegativity. As a result, the electrons which the donor shares with the hydrogen are unequally distributed and this causes the hydrogen to take a slight positive charge. On the other hand, the acceptor atom (A), e.g. (N, O, F) has a pair of unshared electrons, which gives the atom a slight negative charge (Figure 1-4). H-bonds are electrostatic and directional, i.e. the D-H---A angles lean towards linearity. An example of intermolecular hydrogen bonding can be found in the co-crystal of (1,1′-bis(pyridin-4-ylmethyl)-2,2′-biimidazole and glutaric acid (Fig 1-5).[34]

Figure 1-4 A schematic of hydrogen bonding.

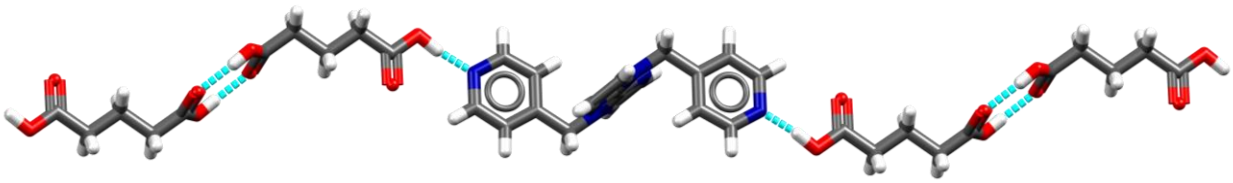

Figure 1-5 Hydrogen bonding in a co-crystal of 1,1′-bis(pyridin-4-ylmethyl)-2,2′-biimidazole and glutaric acid.

Another remarkable contribution in the study of H-bonding came from Margaret C. Etter who postulated systematic H-bonding patterns in multicomponent systems.[35] Etter proposed that:

1. All good proton donors and acceptors in a molecule will be used in hydrogen bonding.
2. Six-membered intramolecular hydrogen bonds are preferred over intermolecular hydrogen-bonds.
3. The best acidic donors and acceptors remaining after intramolecular hydrogen-bond will form intermolecular hydrogen bonds to one another.

Additionally, Etter and co-workers[36] introduced the Graph Set Notation, a tool used to describe and explain H-bonding patterns in crystals.

1.3.2. Halogen bonding

The halogen bond has recently gained attention in supramolecular chemistry because of its directional nature and comparable in strength to hydrogen-bonds (~4-200kJ/mol).[10] It occurs *"when there is a net attractive interaction between an electrophilic region associated with a halogen atom in a molecular entity and a nucleophilic region in another, or the same, molecular entity"*.[37] The halogen bond is signified by the presence of the electron-poor tip of the halogen atom (σ hole) which interacts with the nucleophilic region of the neighboring molecule (Figure 1-6).[9] Figure 1-7 shows a halogen bond formed between iodine and nitrogen in a co-crystal of 4-bromo-octafluoro-4-iodobiphhenyl with 4-(*N*,*N*-dimethyl amino)pyridine.[38]

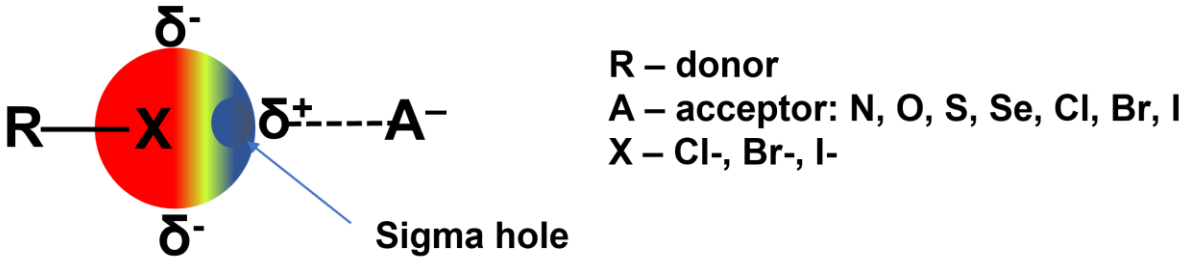

Figure 1-6 A schematic of halogen bonding.

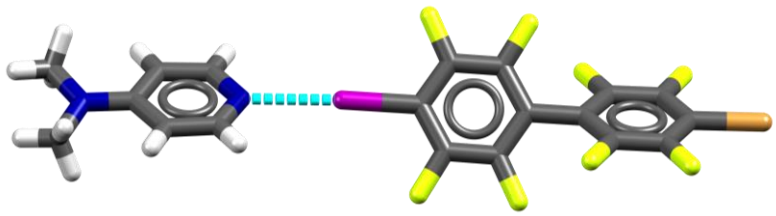

Figure 1-7 Halogen bonding in co-crystal of 4-bromo-octafluoro-4iodobiphhenyl with 4-(N,N-dimethyl amino)pyridine.

1.4.Supramolecular synthons

Supramolecular synthons were defined by Desiraju as "*structural units within supermolecules which can be formed and/or assembled by known or conceivable synthetic operations involving intermolecular interactions*".[39] The supramolecular synthons dictate structure and so the design of robust transferable interactions that can be used to logically guide the aggregation of molecules from one system to the other is crucial.[40] Supramolecular synthons may be classified in two categories: homosynthons and heterosynthons. The homosynthon is formed between identical functional groups, while the heterosynthon is built from different functional groups or complementary donor and acceptor groups.[41] Figure 1-8 shows some examples of supramolecular synthons.

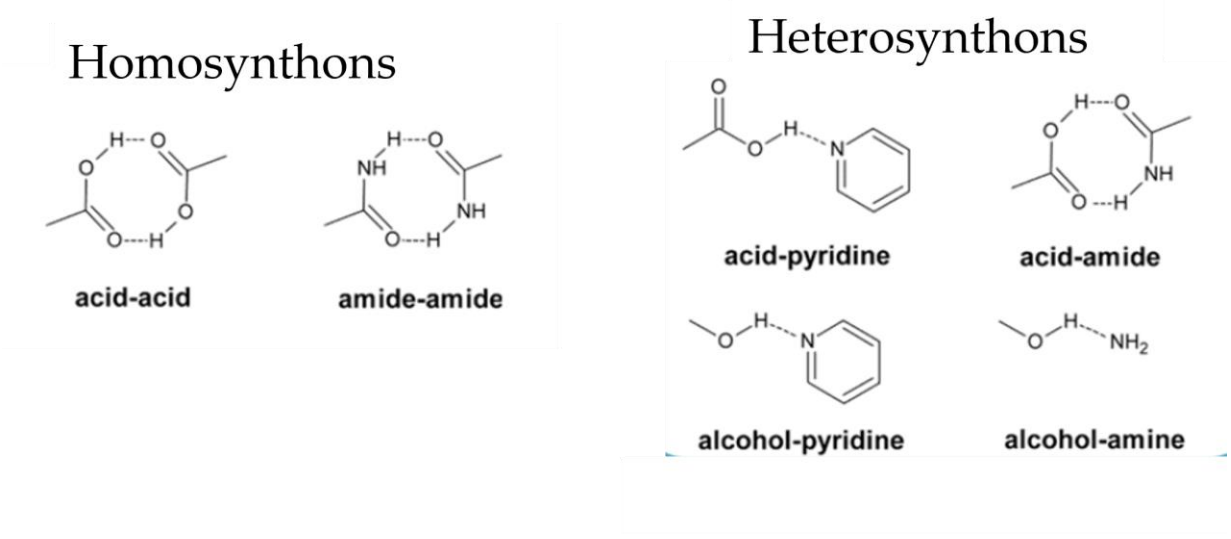

Figure 1-8 Examples of supramolecular synthons

1.5. Multicomponent solid forms

Co-crystallization is the process of combining a target with molecular partner, into the same crystal lattice via heteromeric interactions. Co-crystallization experiments can yield several types of solids: cocrystals, salts, hydrates, solvates or polymorphs.[42] A polymorph is a crystalline solid phase of a given compound resulting from the possibility of at least two crystalline arrangements of the molecules of a given compound in the solid state.[43] Solvates/hydrates can be defined as crystalline solids formed when a compound includes a solvent/water into its structure either in stoichiometric or non-stoichiometric ratio.[44] A co-crystal is *"a solid crystalline single phase material which composed of two or more different neutral molecules in a stoichiometric ratio".*[45] Co-crystals are formed by breaking the homomeric interactions and subsequently replacing them with heteromeric interactions.

1.6. Goals of the thesis

Non-covalent interactions such as hydrogen and halogen bonding will be addressed from a fundamental viewpoint. Additionally, the rational use of non-covalent interactions in design and control of supramolecular architectures will be addressed in this thesis. The scientific challenges addressed in this thesis can be split into three parts; (i) Evaluating supramolecular binding and aggregation in the organic solid state, (ii) Evaluating the role of geometry in driving co-crystallization, (iii) Evaluating binding preference between competing intermolecular forces (HB/XB components) in the organic solid state, (iv)

Establishing structure-property relationships in thermally responsive crystals based on molecular dimension and intermolecular forces, and (v) Using non-covalent interactions for practical crystal engineering of hydrogen-bonded organic frameworks.

In order to address these specific areas, this dissertation will focus on the following goals:

Chapter 2 examines the effect of increasing chain length on thiazole-based carbamates as well as the effect of adding a methyl substituent on the thiazole ring on molecular packing.

Chapter 3 evaluates the structural influence of hydrogen bonding on co-crystal formation using a dicarbamate target.

Chapter 4 deals with establishing halogen-bond preferences in molecules with multiple acceptor sites.

Chapter 5 analyzes the structure-property relationships in a group of thermally responsive targets, and the ability to control thermal expansion will be discussed.

Chapter 6 explores the design of hydrogen-bonded organic frameworks (HOF) for applications of crystal engineering as molecular containers/hosts for volatile compounds.

1.7.References

1. Steed, J. W.; Atwood, J. L., *Supramolecular Chemistry*. Wiley: 2013.
2. Lehn, J.-M., Supramolecular Chemistry—Scope and Perspectives Molecules, Supermolecules, and Molecular Devices (Nobel Lecture). *Angewandte Chemie International Edition in English* **1988,** *27* (1), 89-112.
3. Dunitz, J. D., Thoughts on Crystals as Supermolecules. In *Perspectives in Supramolecular Chemistry*, John Wiley & Sons, Ltd.: 2007; pp 1-30.
4. Kollman, P. A.; Allen, L. C., Theory of the hydrogen bond. *Chemical Reviews* **1972,** *72* (3), 283-303.
5. Perdigão, L. M. A.; Champness, N. R.; Beton, P. H., Surface self-assembly of the cyanuric acid–melamine hydrogen bonded network. *Chemical Communications* **2006,** (5), 538-540.
6. Chakrabarty, R.; Mukherjee, P. S.; Stang, P. J., Supramolecular Coordination: Self-Assembly of Finite Two- and Three-Dimensional Ensembles. *Chemical Reviews* **2011,** *111* (11), 6810-6918.
7. Aakeröy, C. B.; Seddon, K. R., The hydrogen bond and crystal engineering. *Chemical Society Reviews* **1993,** *22* (6), 397-407.
8. Bruton, E. A.; Brammer, L.; Christopher Pigge, F.; Aakeröy, C. B.; Leinen, D. S., Hydrogen bond patterns in aromatic and aliphatic dioximes. *New Journal of Chemistry* **2003,** *27* (7), 1084-1094.
9. Desiraju, G. R.; Ho, P. S.; Kloo, L.; Legon, A. C.; Marquardt, R.; Metrangolo, P.; Politzer, P.; Resnati, G.; Rissanen, K., Definition of the halogen bond (IUPAC Recommendations 2013). *Pure and Applied Chemistry* **2013,** *85* (8), 1711-1713.
10. Cavallo, G.; Metrangolo, P.; Milani, R.; Pilati, T.; Priimagi, A.; Resnati, G.; Terraneo, G., The Halogen Bond. *Chemical Reviews* **2016,** *116* (4), 2478-2601.
11. Meazza, L.; Foster, J. A.; Fucke, K.; Metrangolo, P.; Resnati, G.; Steed, J. W., Halogen-bonding-triggered supramolecular gel formation. *Nature Chemistry* **2013,** *5* (1), 42-47.
12. Aakeröy, C. B.; Schultheiss, N.; Desper, J.; Moore, C., Attempted assembly of discrete coordination complexes into 1-D chains using halogen bonding or halogen···halogen interactions. *CrystEngComm* **2007,** *9* (5), 421-426.
13. Madura, I. D.; Czerwińska, K.; Jakubczyk, M.; Pawełko, A.; Adamczyk-Woźniak, A.; Sporzyński, A., Weak C–H···O and Dipole–Dipole Interactions as Driving Forces in Crystals of Fluorosubstituted Phenylboronic Catechol Esters. *Crystal Growth & Design* **2013,** *13* (12), 5344-5352.
14. Würthner, F., Dipole–Dipole Interaction Driven Self-Assembly of Merocyanine Dyes: From Dimers to Nanoscale Objects and Supramolecular Materials. *Accounts of Chemical Research* **2016,** *49* (5), 868-876.

15. Chang, Y.-C.; Chen, Y.-D.; Chen, C.-H.; Wen, Y.-S.; Lin, J. T.; Chen, H.-Y.; Kuo, M.-Y.; Chao, I., Crystal Engineering for π−π Stacking via Interaction between Electron-Rich and Electron-Deficient Heteroaromatics. *The Journal of Organic Chemistry* **2008,** *73* (12), 4608-4614.
16. Hunter, C. A.; Sanders, J. K. M., The nature of .pi.-.pi. interactions. *Journal of the American Chemical Society* **1990,** *112* (14), 5525-5534.
17. Kobayashi, K.; Shirasaka, T.; Yamaguchi, K.; Sakamoto, S.; Horn, E.; Furukawa, N., Molecular capsule constructed by multiple hydrogen bonds: self-assembly of cavitand tetracarboxylic acid with 2-aminopyrimidine. *Chemical Communications* **2000,** (1), 41-42.
18. Ball, P., The shapes of things to come. *Nature* **1994,** *371* (6494), 202-203.
19. McComas, C. C.; Crowley, B. M.; Boger, D. L., Partitioning the Loss in Vancomycin Binding Affinity for d-Ala-d-Lac into Lost H-Bond and Repulsive Lone Pair Contributions. *Journal of the American Chemical Society* **2003,** *125* (31), 9314-9315.
20. Lavendomme, R.; Zahim, S.; De Leener, G.; Inthasot, A.; Mattiuzzi, A.; Luhmer, M.; Reinaud, O.; Jabin, I., Rational Strategies for the Selective Functionalization of Calixarenes. *Asian Journal of Organic Chemistry* **2015,** *4* (8), 710-722.
21. Mezo, A. R.; Sherman, J. C., Water-Soluble Cavitands: Synthesis of Methylene-Bridged Resorcin[4]arenes Containing Hydroxyls and Phosphates at Their Feet and Bromomethyls and Thiomethyls at Their Rims. *The Journal of Organic Chemistry* **1998,** *63* (20), 6824-6829.
22. Pinalli, R.; Dalcanale, E., Supramolecular Sensing with Phosphonate Cavitands. *Accounts of Chemical Research* **2013,** *46* (2), 399-411.
23. Numanoğlu, U.; Şen, T.; Tarimci, N.; Kartal, M.; Koo, O. M. Y.; Önyüksel, H., Use of cyclodextrins as a cosmetic delivery system for fragrance materials: Linalool and benzyl acetate. *AAPS PharmSciTech* **2007,** *8* (4), 85.
24. Kim, K.; Selvapalam, N.; Ko, Y. H.; Park, K. M.; Kim, D.; Kim, J., Functionalized cucurbiturils and their applications. *Chemical Society Reviews* **2007,** *36* (2), 267-279.
25. Turunen, L.; Pan, F.; Beyeh, N. K.; Trant, J. F.; Ras, R. H. A.; Rissanen, K., Bamboo-like Chained Cavities and Other Halogen-Bonded Complexes from Tetrahaloethynyl Cavitands with Simple Ditopic Halogen Bond Acceptors. *Crystal Growth & Design* **2018,** *18* (1), 513-520.
26. Turunen, L.; Beyeh, N. K.; Pan, F.; Valkonen, A.; Rissanen, K., Tetraiodoethynyl resorcinarene cavitands as multivalent halogen bond donors. *Chemical Communications* **2014,** *50* (100), 15920-15923.
27. Turunen, L.; Pan, F.; Beyeh, N. K.; Cetina, M.; Trant, J. F.; Ras, R. H. A.; Rissanen, K., Halogen-bonded solvates of tetrahaloethynyl cavitands. *CrystEngComm* **2017,** *19* (35), 5223-5229.
28. Desiraju, G. R., *Crystal engineering: the design of organic solids*. Elsevier: 1989.

29. Zhang, C.; Yan, Y.; Sun, L.; Liang, Z.; Li, J., Solvent-induced construction of two zinc metal-organic frameworks for highly selective detection of nitroaromatic explosives. *CrystEngComm* **2016,** *18* (22), 4102-4108.
30. Sozzani, P.; Bracco, S.; Comotti, A.; Ferretti, L.; Simonutti, R., Methane and carbon dioxide storage in a porous van der Waals crystal. *Angewandte Chemie International Edition* **2005,** *44* (12), 1816-1820.
31. Alegre-Requena, J. V.; Marques-Lopez, E.; Herrera, R. P.; Diaz, D. D., Metal-organic frameworks (MOFs) bring new life to hydrogen-bonding organocatalysts in confined spaces. *CrystEngComm* **2016,** *18* (22), 3985-3995.
32. Khan, M.; Enkelmann, V.; Brunklaus, G., Crystal engineering of pharmaceutical co-crystals: application of methyl paraben as molecular hook. *Journal of the American Chemical Society* **2010,** *132* (14), 5254-5263.
33. Berry, D. J.; Steed, J. W., Pharmaceutical cocrystals, salts and multicomponent systems; intermolecular interactions and property based design. *Advanced Drug Delivery Reviews* **2017**.
34. Aakeröy, C. B.; Wijethunga, T. K.; Desper, J., Molecular electrostatic potential dependent selectivity of hydrogen bonding. *New Journal of Chemistry* **2015,** *39* (2), 822-828.
35. Etter, M. C., Encoding and decoding hydrogen-bond patterns of organic compounds. *Accounts of Chemical Research* **1990,** *23* (4), 120-126.
36. Etter, M. C.; MacDonald, J. C.; Bernstein, J., Graph-set analysis of hydrogen-bond patterns in organic crystals. *Acta Crystallographica Section B* **1990,** *46* (2), 256-262.
37. Metrangolo, P.; Resnati, G., Type II halogen...halogen contacts are halogen bonds. *IUCrJ* **2014,** *1* (1), 5-7.
38. Aakeröy, C. B.; Chopade, P. D.; Desper, J., Establishing a Hierarchy of Halogen Bonding by Engineering Crystals without Disorder. *Crystal Growth & Design* **2013,** *13* (9), 4145-4150.
39. Desiraju, G. R., Supramolecular Synthons in Crystal Engineering—A New Organic Synthesis. *Angewandte Chemie International Edition in English* **1995,** *34* (21), 2311-2327.
40. Almarsson, O.; Zaworotko, M. J., Crystal engineering of the composition of pharmaceutical phases. Do pharmaceutical co-crystals represent a new path to improved medicines? *Chemical Communications* **2004,** (17), 1889-1896.
41. Steed, J. W.; Gale, P. A., *Supramolecular Chemistry, 8 Volume Set: From Molecules to Nanomaterials*. Wiley: 2012.
42. Aitipamula, S.; Banerjee, R.; Bansal, A. K.; Biradha, K.; Cheney, M. L.; Choudhury, A. R.; Desiraju, G. R.; Dikundwar, A. G.; Dubey, R.; Duggirala, N.; Ghogale, P. P.; Ghosh, S.; Goswami, P. K.; Goud, N. R.; Jetti, R. R. K. R.; Karpinski, P.; Kaushik, P.; Kumar, D.; Kumar, V.; Moulton, B.; Mukherjee, A.; Mukherjee, G.; Myerson, A. S.; Puri, V.; Ramanan, A.; Rajamannar, T.; Reddy, C. M.; Rodriguez-Hornedo, N.; Rogers, R. D.; Row, T. N. G.; Sanphui, P.; Shan, N.; Shete, G.; Singh, A.; Sun, C. C.; Swift, J. A.; Thaimattam, R.; Thakur, T. S.; Kumar Thaper, R.; Thomas, S. P.;

Tothadi, S.; Vangala, V. R.; Variankaval, N.; Vishweshwar, P.; Weyna, D. R.; Zaworotko, M. J., Polymorphs, Salts, and Cocrystals: What's in a Name? *Crystal Growth & Design* **2012,** *12* (5), 2147-2152.
43. Brittain, H. G.; Grant, D. J. W.; Myrdal, P., Effects of Polymorphism and Solid-State Solvation on Solubility and Dissolution Rate. *Polymorphism in Pharmaceutical Solids* **2018**.
44. Braun, D. E.; Griesser, U. J., Why Do Hydrates (Solvates) Form in Small Neutral Organic Molecules? Exploring the Crystal Form Landscapes of the Alkaloids Brucine and Strychnine. *Crystal Growth & Design* **2016,** *16* (11), 6405-6418.
45. Bond, A. D., What is a co-crystal? *CrystEngComm* **2007,** *9* (9), 833-834.

Chapter 2 - Evaluating intermolecular binding and crystal packing behavior in thiazole-based carbamates

2.1. Introduction

The thiazole and carbamate functionalities are present in several commercially important compounds such as pharmaceutical entities[1, 2] energetic materials[3, 4], and pesticides[5, 6] *etc*. Having insights into intermolecular interactions is critical for designing and developing solid-state materials as it provides fundamental knowledge required for the bottom-up design of molecular materials with controllable structures and desirable bulk properties. Sandhu[7] *et al* analyzed the structural chemistry of thiazole-based amide target molecules using structural informatics as a way of predicting which intermolecular interactions are likely to appear in the solid state. Likewise, the binding preference in pyridyl based carbamates was recently explored and it was found that the N–H---N_{pyr} hydrogen bond is the dominant intermolecular interaction as it appears in all of the reported target crystal structures.[8] Despite the commercial and practical interests in carbamates and thiazoles, there are very few reports on the structural balance and competition between intermolecular compounds containing both functional groups simultaneously.

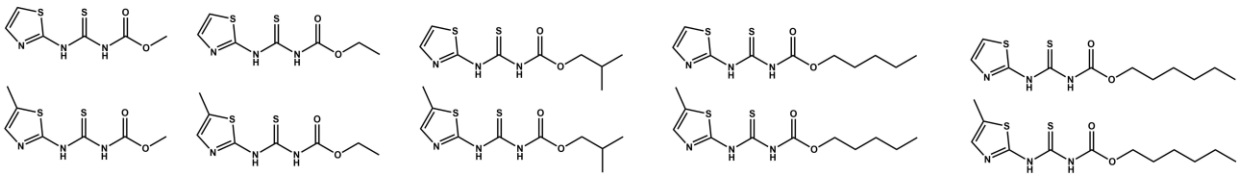

Scheme 2-1 Molecular structures of the targets used in this study (top row) series 1 TZI-TZ5 from left to right and (bottom row) series 2 TZ6-TZ10 from left to right.

In this Chapter, we want to establish and rank the intermolecular interaction preferences among our selected targets. The target molecules **TZ1**-**TZ10** (scheme 2-1) are divided into two groups based on the thiazole backbone R((2-thiazoyl)carbamothioyl)carbamate and R((2-thiazoyl-5-methyl)carbamothioyl)carbamate (R=methyl>hexyl). The expected interactions between the hydrogen-bond donor and the acceptors could lead to two possible synthons (scheme 2-2).

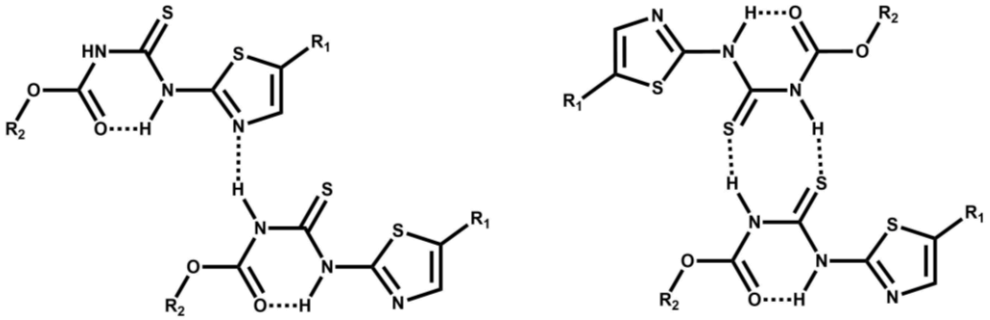

Scheme 2-2 Postulated synthons for both series 1 and series 2 based on the target functional groups.

The study is performed in order to answer the following questions,

1. Which is the most optimal (dominant) synthon in the two series of compounds?
2. What is the structural impact of varying chain length (R= methyl>hexyl) on the packing of target molecules (Scheme 2-2)?
3. How does adding a methyl substituent on the thiazole ring affect the overall assembly?

2.2. Experimental

2.2.1. Reagents and General Methods

All reagents were used as received without any further purification. All the NMRs were recorded on a Bruker 400 MHz spectrometer. Single crystal X-ray diffraction (SCXRD) data were obtained using a Rigaku XtaLAB Synergy-S with a CuKα source. The melting points were collected using a TA instrument DSC Q20 differential scanning calorimeter. Targets were synthesized using modified versions of reported procedures[9, 10].

2.2.2. Synthesis of methyl-*N*-[(2-thiazolylamino) thioxomethyl] carbamate

Methyl chloroformate (0.78 mL, 10mmol) was added dropwise to a solution of ethyl acetate containing potassium thiocyanate (1.17 g, 12 mmol). The reaction mixture was heated at 75 °C for 3 hours. Potassium chloride (KCl) was filtered off and 2-aminothiazole (0.94 g, 10 mmol) was added to the filtrate. The reaction mixture was heated under reflux

for a further 5 hours. The mixture was then cooled to room temperature followed by vacuum filtration. After evaporating the solvent in vacuum, the product was purified by column chromatography. The product was a faint brown solid with a yield of 58 %. Mp 156-158 °C. ^{1}H NMR (400 MHz, Chloroform-d) δ 12.74 (s, 1H), 8.26 (s, 1H), 7.58 (d, J = 3.5 Hz, 1H), 7.02 (d, J = 3.5 Hz, 1H), 3.89 (s, 3H).

2.2.3. Synthesis of methyl-*N*-[(5-methyl-2-thiazolylamino) thioxomethyl] carbamate

Methyl chloroformate (0.78 mL, 10mmol) was added dropwise to a solution of ethyl acetate containing potassium thiocyanate (1.17 g, 12 mmol). The reaction mixture was heated at 75 °C for 3 hours. KCl was filtered off and 5-methyl-2-aminothiazole (10 mmol) was added to filtrate. The reaction mixture was heated under reflux for a further 5 hours. The mixture was cooled to room temperature followed by vacuum filtration. After evaporating the solvent in vacuum, the product was purified by column chromatography. The product was a yellow solid with a yield of 46 %. Mp 80-81 °C. ^{1}H NMR (400 MHz, Chloroform-d) δ 12.50 (s, 1H), 8.30 (s, 1H), 7.21 (q, J = 1.6 Hz, 1H), 3.88 (s, 3H), 2.53 (d, J = 1.3 Hz, 3H).

2.2.4. Synthesis of ethyl-*N*-[(2-thiazolylamino) thioxomethyl] carbamate

Ethyl chloroformate (0.96 mL, 10mmol) and ethyl acetate were mixed in a round bottomed flask. To this solution, potassium thiocyanate (1.17 g, 12 mmol) and N,N,N′,N′-

tetramethylethylenediamine (TMEDA) (0.02 mL, 0.1 mmol) were added and the reaction mixture was stirred at room temperature for 5 hours. 2-aminothiazole (0.94 g, 10 mmol) was then slowly added to the mixture with constant stirring. The reaction mixture was stirred at room temperature for another 5 hours. The progress of the reaction was monitored using TLC. After evaporating the solvent in vacuum, the product was purified by column chromatography. The product was a yellow solid with a yield of 75%. Mp 171-173 °C. ^{1}H NMR (400 MHz, Chloroform-d) δ 12.82 (s, 1H), 8.16 (s, 1H), 7.60 (dd, J = 3.6, 1.5 Hz, 1H), 7.28 (s, 0H), 7.04 (dd, J = 3.6, 1.4 Hz, 1H), 4.35 (qd, J = 7.2, 1.5 Hz, 2H), 1.38 (td, J = 7.1, 1.5 Hz, 3H).

2.2.5. Synthesis of ethyl-*N*-[(5-methyl-2-thiazolylamino) thioxomethyl] carbamate

Ethyl chloroformate (0.96 mL, 10mmol) and ethyl acetate were mixed in a round bottomed flask. To this solution, potassium thiocyanate (1.17 g, 12 mmol) and N,N,N′,N′-tetramethylethylenediamine (TMEDA) (0.02 mL, 0.1 mmol) were added and the reaction mixture was stirred at room temperature for 5 hours. 2-aminothiazole (10 mmol) was then slowly added to the reaction mixture with constant stirring. The reaction mixture was stirred at room temperature for another 5 hours. The progress of the reaction was monitored using TLC. After evaporating the solvent in vacuum, the product was purified by column chromatography. The product was a white solid with a yield of 79%. Mp 167-

169 °C. ^{1}H NMR (400 MHz, Chloroform-d) δ 12.53 (s, 1H), 8.18 (s, 1H), 7.23 (q, J = 1.2 Hz, 1H), 4.34 (q, J = 7.1 Hz, 2H), 2.43 (d, J = 1.3 Hz, 3H), 1.37 (t, J = 7.1 Hz, 3H).

2.2.6. Synthesis of isobutyl-*N*-[(2-thiazolylamino) thioxomethyl] carbamate

Isobutyl chloroformate (1.30 mL, 10mmol) and ethyl acetate were mixed in a round bottomed flask. To this solution, potassium thiocyanate (1.17 g, 12 mmol) and TMEDA (0.02 mL, 0.1 mmol) were added, and the reaction mixture was stirred at room temperature for 5 hours. 2-aminothiazole (10 mmol) was then slowly added to the reaction mixture with constant stirring. The reaction mixture was stirred at room temperature for another 5 hours. After evaporating the solvent in vacuum, the product was purified by column chromatography. The product was a white solid with a yield of 65%. Mp 137-139 °C. ^{1}H NMR (400 MHz, Chloroform-d) δ 12.84 (s, 1H), 8.27 (s, 1H), 7.60 (t, J = 2.9 Hz, 1H), 7.04 (d, J = 3.1 Hz, 1H), 4.07 (dd, J = 6.9, 2.3 Hz, 2H), 2.07 – 2.03 (m, 1H), 1.00 (dd, J = 6.8, 2.3 Hz, 6H).

2.2.7. Synthesis of isobutyl-*N*-[(5-methyl-2-thiazolylamino) thioxomethyl] carbamate

Isobutyl chloroformate (1.30 mL, 10mmol) and ethyl acetate were mixed in a round bottomed flask. To this solution, potassium thiocyanate (1.17 g, 12 mmol) and TMEDA (0.02 mL, 0.1 mmol) were added, and the reaction mixture was stirred at room temperature for 5 hours. 2-aminothiazole (0.94 g, 10 mmol) was then slowly added to the

reaction mixture with constant stirring. The reaction mixture was stirred at room temperature for another 5 hours. After evaporating the solvent in vacuum, the product was purified by column chromatography. The product was a white solid with a yield of 68%. Mp 197-198 °C. 1H NMR (400 MHz, Chloroform-d) δ 12.63 (s, 1H), 8.14 (s, 1H), 7.23 (s, 1H), 4.06 (d, J = 6.6 Hz, 2H), 2.03 (dq, J = 13.5, 6.6 Hz, 1H), 0.99 (d, J = 6.7 Hz, 6H), 0.94 – 0.87 (m, 1H).

2.2.8. Synthesis of pentyl-*N*-[(2-thiazolylamino) thioxomethyl] carbamate

Pentyl chloroformate (1.30 mL, 10mmol) and ethyl acetate were mixed in a round bottomed flask. To this solution, potassium thiocyanate (1.17 g, 12 mmol) and TMEDA (0.02 mL, 0.1 mmol) were added, and the reaction mixture was stirred at room temperature for 5 hours. 2-aminothiazole (10 mmol) was then slowly added to the reaction mixture with constant stirring. The reaction mixture was stirred at room temperature for another 5 hours. After evaporating the solvent in vacuum, the product was purified by column chromatography. The product was a white solid with a yield of 71%. 1H NMR (400 MHz, Chloroform-d) δ 12.85 (s, 1H), 8.15 (s, 1H), 7.63 – 7.57 (m, 1H), 7.29 (s, 1H), 7.07 – 7.01 (m, 1H), 4.32 – 4.24 (m, 2H), 1.73 (p, J = 7.1 Hz, 2H), 1.39 (h, J = 3.6 Hz, 4H), 0.99 – 0.91 (m, 3H).

2.2.9. Synthesis of pentyl-*N*-[(5-methyl-2-thiazolylamino) thioxomethyl] carbamate

Pentyl chloroformate (1.30 mL, 10mmol) and ethyl acetate were mixed in a round bottomed flask. To this solution, potassium thiocyanate (1.17 g, 12 mmol) and TMEDA (0.02 mL, 0.1 mmol) were added, and the reaction mixture was stirred at room temperature for 5 hours. 2-aminothiazole (10 mmol) was then slowly added to the reaction mixture with constant stirring. The reaction mixture was stirred at room temperature for another 5 hours. After evaporating the solvent in vacuum, the product was purified by column chromatography. The product was a white solid. NMR (400 MHz, Chloroform-d) δ 12.56 (s, 1H), 8.18 (s, 1H), 7.23 (d, J = 1.5 Hz, 1H), 4.27 (t, J = 6.6 Hz, 2H), 2.46 – 2.38 (m, 3H), 1.73 (q, J = 7.0 Hz, 1H), 1.39 (dh, J = 7.4, 3.7 Hz, 4H), 0.99 – 0.91 (m, 3H).

2.2.10. Synthesis of hexyl-*N*-[(2-thiazolylamino) thioxomethyl] carbamate

Hexyl chloroformate (1.30 mL, 10mmol) and ethyl acetate were mixed in a round bottomed flask. To this solution, potassium thiocyanate (1.17 g, 12 mmol) and TMEDA (0.02 mL, 0.1 mmol) were added, and the reaction mixture was stirred at room temperature for 5 hours. 2-aminothiazole (10 mmol) was then slowly added to the reaction mixture with constant stirring. The reaction mixture was stirred at room temperature for another 5 hours. After evaporating the solvent in vacuum, the product was purified by column chromatography. The product was a white solid. ^{1}H NMR (400

MHz, Chloroform-d) δ 12.85 (s, 1H), 8.12 (s, 1H), 7.60 (d, J = 3.5 Hz, 1H), 7.04 (d, J = 3.5 Hz, 1H), 4.28 (t, J = 6.7 Hz, 2H), 1.72 (p, J = 6.7 Hz, 2H), 1.40 (t, J = 7.9 Hz, 3H), 1.35 (s, 4H), 1.37 – 1.31 (m, 1H), 0.97 – 0.89 (m, 3H).

2.2.11. Synthesis of hexyl-*N*-[(5-methyl-2-thiazolylamino) thioxomethyl] carbamate

Hexyl chloroformate (1.30 mL, 10mmol) and ethyl acetate were mixed in a round bottomed flask. To this solution, potassium thiocyanate (1.17 g, 12 mmol) and TMEDA (0.02 mL, 0.1 mmol) were added, and the reaction mixture was stirred at room temperature for 5 hours. 2-aminothiazole (10 mmol) was then slowly added to the reaction mixture with constant stirring. The reaction mixture was stirred at room temperature for another 5 hours. After evaporating the solvent in vacuum, the product was purified by column chromatography. The product was a white solid. 1H NMR (400 MHz, Chloroform-d) δ 12.68 (s, 1H), 8.13 (s, 1H), 7.26 – 7.21 (m, 1H), 4.27 (t, J = 6.7 Hz, 2H), 2.44 (d, J = 1.2 Hz, 3H), 1.72 (q, J = 7.0 Hz, 2H), 1.36 (ddq, J = 11.4, 8.3, 5.2, 3.7 Hz, 6H), 0.97 – 0.89 (m, 3H).

2.2.12. Crystal growth

In order to obtain crystals suitable for single-crystal X-ray diffraction, slow evaporation was used. Each target was dissolved in 3-5mL of selected solvent (Table 2-1), the resulting

solution was covered with parafilm perforated with holes and left to evaporate at room temperature until crystal appeared (from days to weeks).

Table 2-1 Solvents used for crystal growth.

Compound	Code	Solvent
methyl-*N*-[(2-thiazolylamino) thioxomethyl] carbamate	TZ1	Ethyl Acetate
ethyl-*N*-[(2-thiazolylamino) thioxomethyl] carbamate	TZ2	Ethyl Acetate
isobutyl-*N*-[(2-thiazolylamino) thioxomethyl] carbamate	TZ3	Ethyl Acetate
pentyl-*N*-[(2-thiazolylamino) thioxomethyl] carbamate	TZ4	Hexane:ethyl acetate
hexyl-*N*-[(2-thiazolylamino) thioxomethyl] carbamate	TZ5	Hexane:ethyl acetate
methyl-*N*-[(5-methyl-2-thiazolylamino) thioxomethyl] carbamate	TZ6	Methanol
ethyl-*N*-[(5-methyl-2-thiazolylamino) thioxomethyl] carbamate	TZ7	Ethyl Acetate
isobutyl-*N*-[(5-methyl-2-thiazolylamino) thioxomethyl] carbamate	TZ8	Ethyl Acetate
pentyl-*N*-[(5-methyl-2-thiazolylamino) thioxomethyl] carbamate	TZ9	Hexane:ethyl acetate
hexyl-*N*-[(5-methyl-2-thiazolylamino) thioxomethyl] carbamate	TZ10	Hexane:ethyl acetate

2.3.Results and Discussion

2.3.1. Crystal structure analysis

We obtained crystals suitable for SCXRD analysis of **TZ1**-**TZ10**. Two thiazole-based carbamate families (each with five members), R((2-thiazoyl)carbamothioyl)carbamate and R((2-thiazoyl-5-methyl)carbamothioyl)carbamate (R=methyl>hexyl) are discussed.

In the crystal structures of **TZ1**, the primary intermolecular interactions were N-H···S=C dimers (Fig 2-1a). Structures **TZ2-TZ5** are held together by N–H---Nthiazole complemented by an intramolecular N–H---O hydrogen bond (Fig. 2-1c, e, g, i). Overall, connectivity in the crystal structures of series 1 molecules show a (N-H···N) primary interaction resulting in chain-like assemblies.

For the methyl substituted analogues (Series 2) the target **TZ6** crystallizes as a methanol solvate. The structures interact via Nthiazole---H-O(methanol) and (carbamate)N-H---O(methanol) hydrogen bonds (Fig 2-1b). In **TZ7** and **TZ8**, similar to **TZ2-TZ5** structures form N–H---Nthiazole interactions (Fig. 2-1d, f). For **TZ9** and **TZ10** (Fig. 2-1h, j), C-H···S=C dimer formation is observed. Unlike for series 1 where the N–H---Nthiazole interaction was dominant, for series 2 the N–H---Nthiazole interaction is observed for shorter chain length targets whereas dimer formation is preferred for the pentyl and hexyl **TZ9** and **TZ10** compounds that are based on the methyl-thiazole ring.

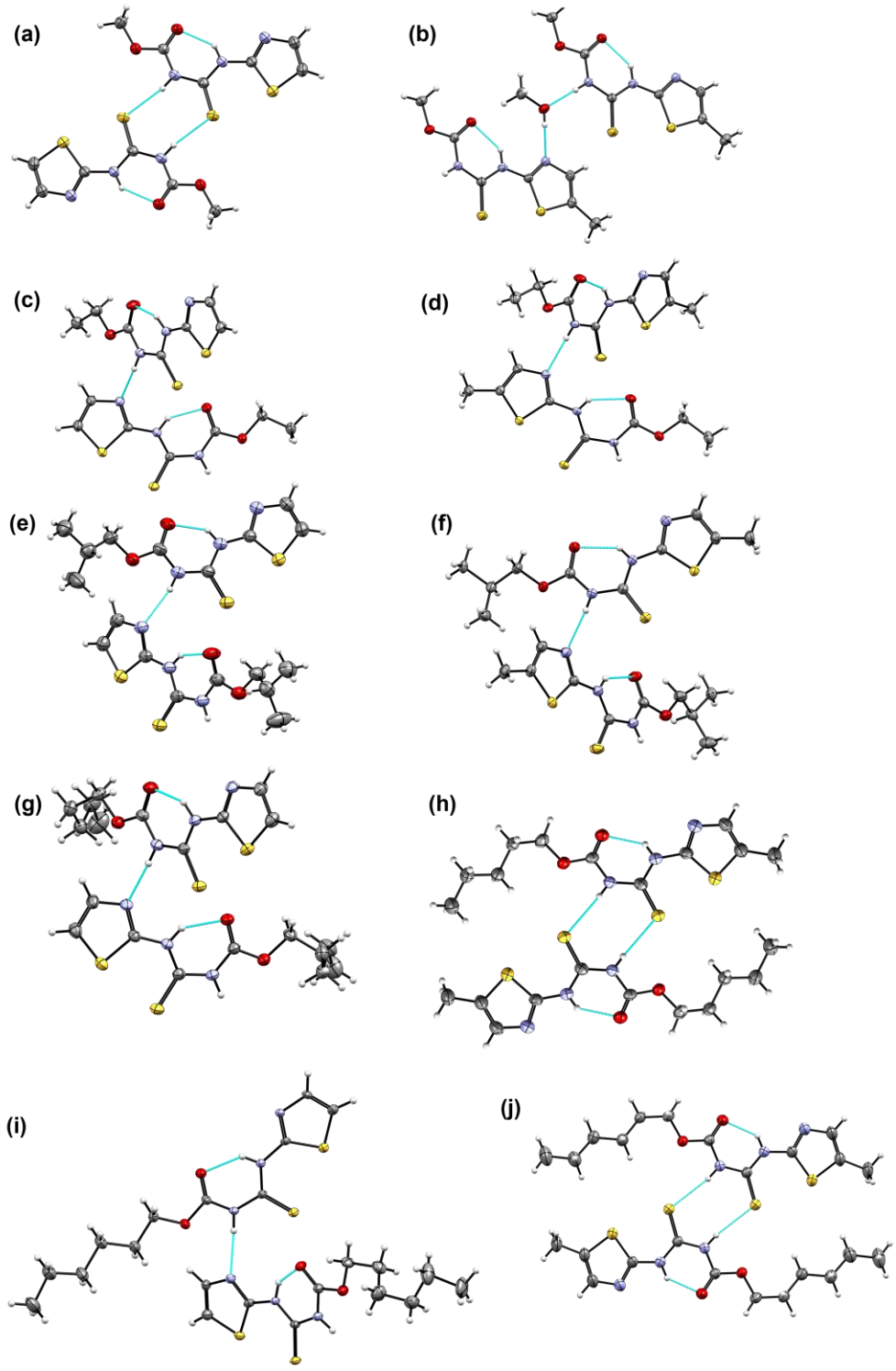

Figure 2-1 Primary non-covalent interactions (in blue) in the crystal structures of (a) TZ1 (c) TZ2 (e) TZ3 (g) TZ4 (i) TZ5, and (b) TZ6 (d) TZ7 (f) TZ8 (h) TZ9 (j) TZ10.

2.3.2. CSD Analysis

A search was done using CSD database (Version 2021.1.0)[11], by drawing the thioxomethyl carbamate group as shown in (Figure 2-2) and using that as a target fragment for a torsion angle search on CSD database (only purely organic compounds were included). The purpose of the analysis was to gain an understanding of how the thioxomethyl carbamate functional group interacts based on reported crystal structures. A total of 89 hits was obtained, and the synthons involved in the structures are summarized in (Figure 2-2). 54 of the 89 structures are held together by the C=S---H-N dimer depicted as synthon **3**. Based on the data found in the systematic search, it is clear that in structures that involved the thioxomethyl carbamate and N-based aromatic rings such as -pyridine and -triazine, other synthons 4, 5, 6 and 10 prevail (Figure 2-2). In our series, synthon 4 was prevalent and our ring was thiazole-based instead of the triazine. This outcome is corroborated by the CSD findings which showed similar synthons with triazole-based rings.

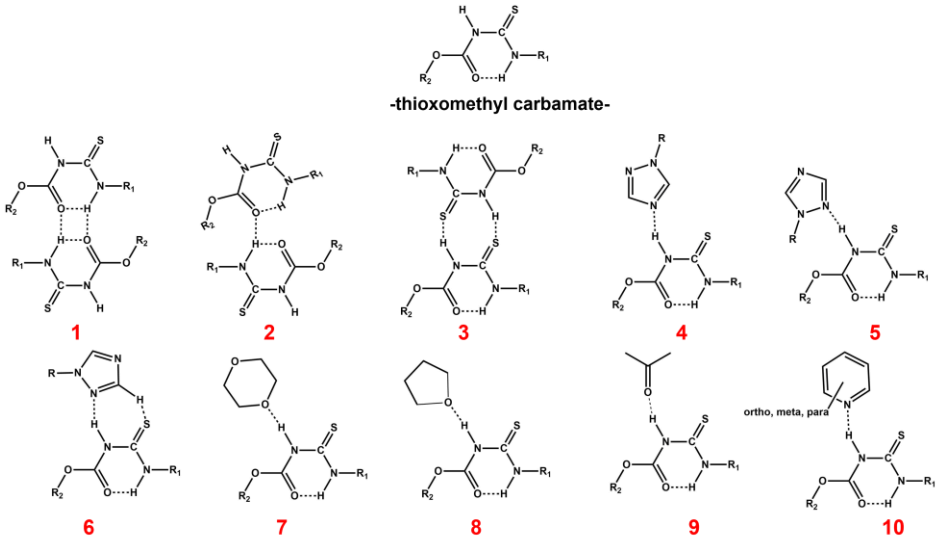

Figure 2-2 Synthons involving thioxomethyl carbamate as per CSD search.

2.3.3. How does an additional ring substituent and increasing chain length affect overall crystal assembly?

Six of the crystal structures of the target compounds showed identical hydrogen-bond motifs (N-H---N), and three other crystals formed (N-H---C=S) dimers. A packing analysis was carried out to investigate (i) the effect that aliphatic chains with varying lengths (R= methyl, ethyl, isobutyl, pentyl and hexyl) may have on crystal lattice and (ii) how the addition of a methyl substituent on the thiazole affects overall crystal packing. For series 1, the crystal structure of **T1** forms layers that stack on top of each other with no notable interlayer interactions (Fig 2-3a). In addition, for **T2-T5**, the targets form infinite chains and the alkyl groups (in purple) point towards each other as seen in the packing units of (Fig 2-3c, e,g,i.). The hydrophobic chains point away from the thiazole ring part of the molecule, similar to what is observed in lipid bilayer.[12, 13] Overall, in series 1 the targets follow a similar packing pattern and increasing the chain length does not alter packing behavior. Consequently, we can deduce that the stronger and more directional hydrogen bonds are capable of resisting any changes in crystal packing preferred by hydrophobic interactions.

In series 2, the target **T6** forms a methanol solvate, which is an outlier in both series. The methanol molecule acts as a bridge between neighboring **T6** molecules, allowing the structure to form infinite chains as in **T2-T5**. For **T7** and **T8**, similar to **T2-T5,** the ethyl and isobutyl groups point toward each other as well and the molecules aggregate into

hydrophobic layers of the alkyl chain and pi-stacked layers of the thiazole rings (Fig 2-3c).

Interestingly, for the longer chain length molecules, pentyl and hexyl, a change in packing behavior is observed. In the presence of a methyl substituent, the infinite chains are replaced by the dimers and in turn the packing has alternating stacks of alkyl chains facing each other and methyl-thiazole rings facing each other (Fig 2-3h, j). Overall, the packing was similar in the target structures with shorter alkyl chain length (methyl-isobutyl) and increasing the alkyl chain length (pentyl and hexyl), results in a noticeable change packing behavior Additionally, the effect of the methyl substituent on the ring is observed in the in the structures of the compounds containing higher chain length, pentyl and hexyl groups. This indicates that at a certain point, hydrophobic interactions can begin to compete, structurally, with the influence of intermolecular interactions that, individually, may be stronger.

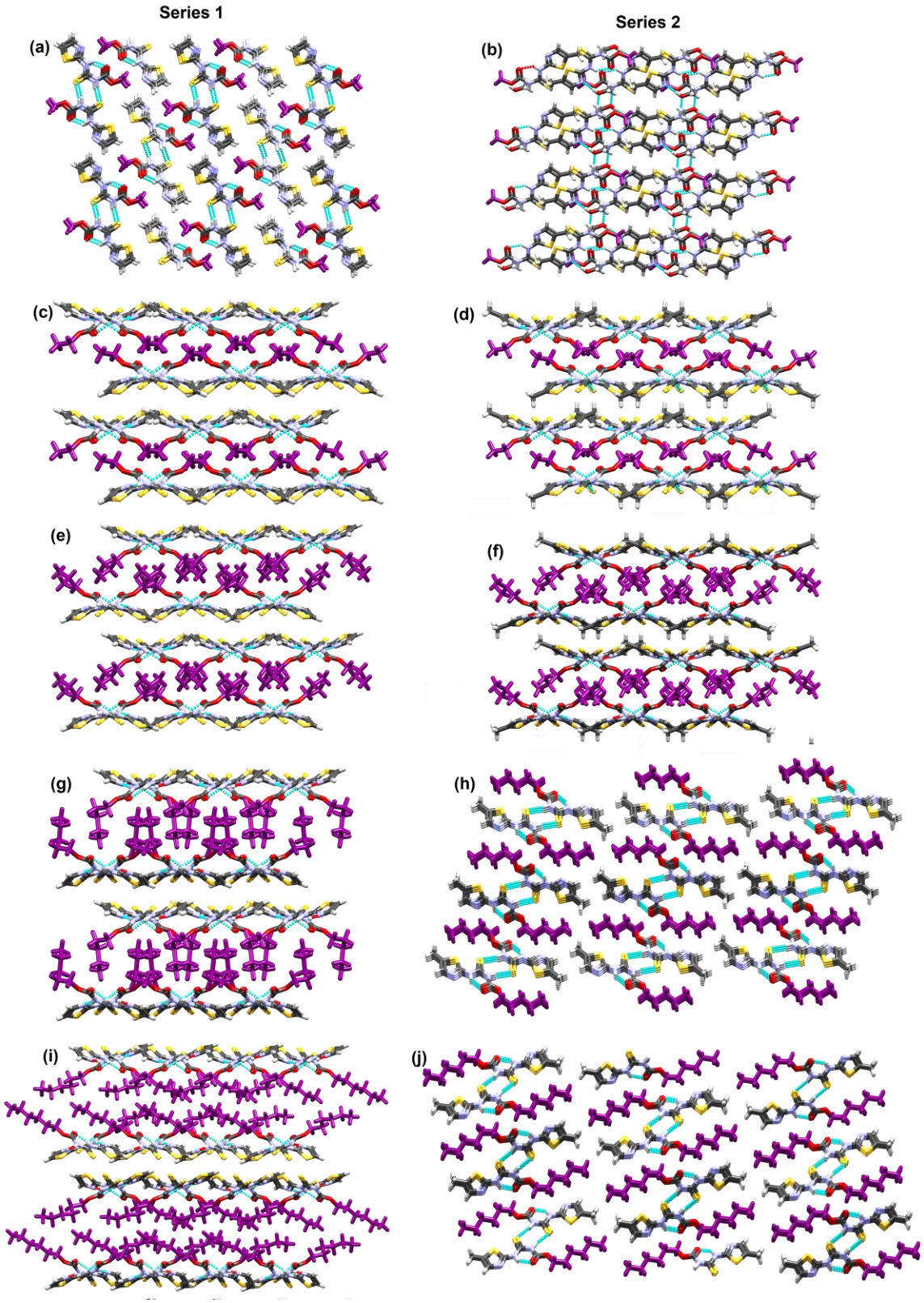

Figure 2-3 Packing in the crystal structures of (a) TZ1 (c) TZ2 (e) TZ3 (g) TZ4 (i) TZ5, (b) TZ6 (d) TZ7 (f) TZ8 (h) TZ9 (j) TZ10.

2.4.Conclusions

1. For series **1**, molecules show the following preferred mode of interaction: (N-H---N) as primary interaction generating chain-like assembly whereas for series **2**, (N-H---N) synthon is preferred in the shorter chain length ethyl and isobutyl while the dimer is preferred for pentyl and hexyl targets.
2. Overall, the targets follow a similar packing pattern and increasing the chain length does not seem to impact packing behavior which means that polarity dominates over hydrophobic interactions.
3. Adding a methyl substituent to the thiazole ring does not seem to impact packing in the target structures with shorter alkyl chain length (methyl-isobutyl). However, for targets containing the alkyl chain length (pentyl and hexyl), the presence of methyl substituent clearly results in a changed packing behavior.

The ability to predict how several types of coexisting functionalities can bind and assemble in solid-state is of fundamental importance because this ultimately dictates the property and function of materials.

2.5.References

1. Tumanov, N. A.; Myz, S. A.; Shakhtshneider, T. P.; Boldyreva, E. V., Are meloxicam dimers really the structure-forming units in the 'meloxicam–carboxylic acid'

co-crystals family? Relation between crystal structures and dissolution behaviour. *CrystEngComm* **2012,** *14* (1), 305-313.
2. Suresh, K.; Mannava, M. K. C.; Nangia, A., Cocrystals and alloys of nitazoxanide: enhanced pharmacokinetics. *Chemical Communications* **2016,** *52* (22), 4223-4226.
3. Axthammer, Q. J.; Klapötke, T. M.; Krumm, B.; Reith, T., Energetic Sila-Nitrocarbamates: Silicon Analogues of Neo-Pentane Derivatives. *Inorganic Chemistry* **2016,** *55* (9), 4683-4692.
4. Axthammer, Q. J.; Krumm, B.; Klapötke, T. M., Synthesis of Energetic Nitrocarbamates from Polynitro Alcohols and Their Potential as High Energetic Oxidizers. *The Journal of Organic Chemistry* **2015,** *80* (12), 6329-6335.
5. Aly, O. M.; El-Dib, M. A., Studies of The Persistence of Some Carbamate Insecticides in The Aquatic Environment. In *Fate of Organic Pesticides in the Aquatic Environment*, AMERICAN CHEMICAL SOCIETY: 1972; Vol. 111, pp 210-243.
6. Shamim, M.; Meléndez, J.; Sappington, K.; Ruhman, M., Conducting Ecological Risk Assessments of Urban Pesticide Uses. In *Describing the Behavior and Effects of Pesticides in Urban and Agricultural Settings*, American Chemical Society: 2014; Vol. 1168, pp 207-274.
7. Sandhu, B.; McLean, A.; Sinha, A. S.; Desper, J.; Sarjeant, A. A.; Vyas, S.; Reutzel-Edens, S. M.; Aakeröy, C. B., Evaluating Competing Intermolecular Interactions through Molecular Electrostatic Potentials and Hydrogen-Bond Propensities. *Crystal Growth & Design* **2018,** *18* (1), 466-478.
8. Shunje, K. N.; Averkiev, B. B.; Aakeröy, C. B., Influence of Multiple Binding Sites on the Supramolecular Assembly of N-[(3-pyridinylamino) Thioxomethyl] Carbamates. *Molecules* **2022,** *27* (12), 3685.
9. Wei, T. B.; Lin, Q.; Zhang, Y. M.; Wang, H., Efficient and Novel Synthesis of N-Aryl-N′-ethoxycarbonylthiourea and Arene-bis-ethoxycarbonylthiourea Derivatives Catalyzed by TMEDA. *Synthetic Communications* **2004,** *34* (12), 2205-2213.
10. Ren, Y.-H.; Song, J.-R.; Xu, K.-Z.; Ma, H.-X.; Huang, J.; Fu, D.-W.; Hu, H.-M., Preparation, Crystal Structure and Theoretical Calculation of N-(Pyrimidin-2-yl)-N′-methoxycarbonyl-thiourea. *Chinese Journal of Chemistry* **2007,** *25* (4), 510-514.
11. Groom, C. R.; Bruno, I. J.; Lightfoot, M. P.; Ward, S. C., The Cambridge Structural Database. *Acta Crystallographica Section B* **2016,** *72* (2), 171-179.
12. Edidin, M., Lipids on the frontier: a century of cell-membrane bilayers. *Nature Reviews Molecular Cell Biology* **2003,** *4* (5), 414-418.
13. Lingwood, D.; Simons, K., Lipid Rafts As a Membrane-Organizing Principle. *Science* **2010,** *327* (5961), 46-50.

Chapter 3 - Multicomponent crystals of Diethyl *N*,*N*′-[1,4-phenylenebis(iminocarbonothioyl)]bis[carbamate]: A versatile hydrogen-bonded system

3.1.Introduction

Crystal engineering deals with designing and synthesizing solid-state structures with desired properties.[1] The use of crystal engineering strategies has sparked huge interest in the design of multicomponent crystalline materials[2, 3] such as co-crystals, salts, hydrates/solvates.[4] Multicomponent crystals offer many possibilities when it comes to crystal engineering since there are various coformers which can be assembled with target compounds by a range of intermolecular forces.[5, 6]

A common strategy for crystal engineering is based on the supramolecular synthon approach, where intermolecular interactions such as hydrogen-bonding interactions, π–π interactions, halogen bonds, are viewed as tools for the construction of supermolecules, *i.e.*, crystals.[7-10]

Among different noncovalent intermolecular interactions, we are particularly interested in hydrogen bonds. The hydrogen bond is an *"….attractive interaction between a proton donor and a proton acceptor in the same or different molecules…"*.[11] Conventional hydrogen bonds represent the strongest interactions[12] (D–H---A), where A and D can be elements such as (N, O, or F), while C–H---O/N and C-H---π belong to non-conventional hydrogen

bonds, which are weaker than conventional hydrogen bonds.[13, 14] The donor atom (D) is covalently bonded to the hydrogen atom (H) and it also has a high electronegativity. As a result, the electrons, which the donor shares with the hydrogen, are unequally shared and this causes the hydrogen to display a slight positive charge. On the other hand, the acceptor atom (A), *e.g*. (N, O, F) has a pair of unshared electrons, which gives the atom a slight negative charge hence the electrostatic and directional nature of the hydrogen bond.

Several computational techniques such as molecular electrostatic potential surfaces (MEPSs)[15], Hirshfeld surface analysis[16] and quantum theory of atoms-in-molecules (QTAIM) analysis[17] have been developed to explain the intermolecular interactions in crystalline solids. The Hirshfeld surface is a unique tool to investigate and visualize different types of intermolecular interactions in multicomponent crystals. The two-dimensional fingerprint plots can provide quantitative information on these interactions/ contacts. For example, Yang et al. performed Hirshfeld surface analysis of 3,4-dinitropyrazole in salts and co-crystals and compared the quantitative information on intermolecular interactions with their crystal structures. Their study revealed how different coformers can influence the different contacts in the structures.[18]

Allophanates represent an important class of thiourea compounds widely known as systemic fungicides, applied to the soil to control a variety of fruit diseases. In order to learn more about structure-property correlations in such compounds, the 'structural landscape' of some thiophanates has been explored to date.[19] For instance, Nauha *et al.*[20] synthesized a series of polymorphs, solvates of thiophanate-methyl (TM) and thiophanate-ethyl (TE) (Scheme 3-1) and investigated the synthons, packing incentives and conformation in different polymorphs, solvates and co-crystals of the molecules. To our knowledge, TM has two polymorphs, fourteen solvates and three co-crystals reported structures while TE has four polymorphs, three co-crystals and seven solvates reported.[21] Interestingly, similar behavior is observed for crystal structures of both TE and TM in that both willingly form solvates and polymorphs, but with varying combinations of hydrogen bonding motifs and conformations of molecules.[19-21] The conformational flexibility of these compounds is such a special feature as the molecules can adjust conformation to accommodate various co-formers as evidenced by the existence of plenty of reported solvates.

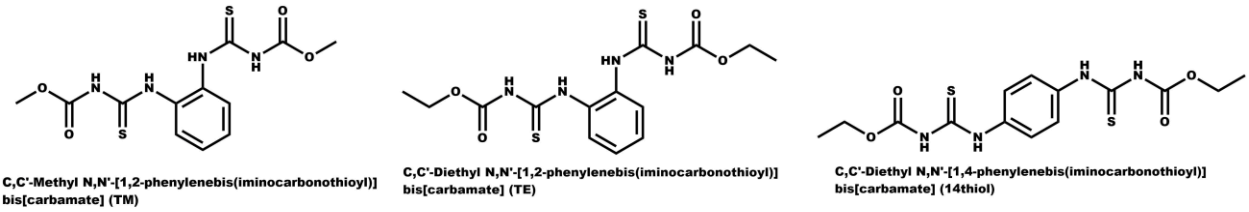

Scheme 3-1 Molecular structure of thiophanate-methyl (TM), thiophanate-ethyl (TE) and 14thiol

In this study we wanted to explore ***C,C′*-Diethyl *N,N′*-[1,4-phenylenebis(iminocarbonothioyl)]bis[carbamate]** (14thiol) as a target molecule and its crystal structure landscape. **14thiol** is structurally similar to TE and TM and the main difference is that the latter are ortho substituted while **14thiol** is para substituted. The amino group, sulfonyl group, and carbonyl group of the **14thiol** molecule can participate in hydrogen-bond interactions as donor and/or acceptor sites and form a variety of supramolecular synthons, which creates the possibility of forming new solid forms of **14thiol** with different co-formers. To the best of our knowledge, the crystal form landscape of **14thiol** has not been explored yet. Four co-formers 4-phenylpyridine, 4,4-bipyridine, trans (1,2-bis(4-pyridyl) ethene), and 4,4-trimethylene bipyridine (Scheme 3-2) were selected to investigate the H-bonding capability of **14thiol**. The pyridine-based acceptor molecules were chosen because they introduce a competitive acceptor and increase the possibility of driving successful co-crystallizations.

This study addressed the following questions:

1. Will the co-formers be capable of disrupting self-complementary homomeric interactions?
2. Can we design multicomponent crystals in our system?
3. Can Hirshfeld surface analysis give insight into the nature of hydrogen-bonding interactions?
4. Does the molecular geometry of 14thiol change in different crystal structures?

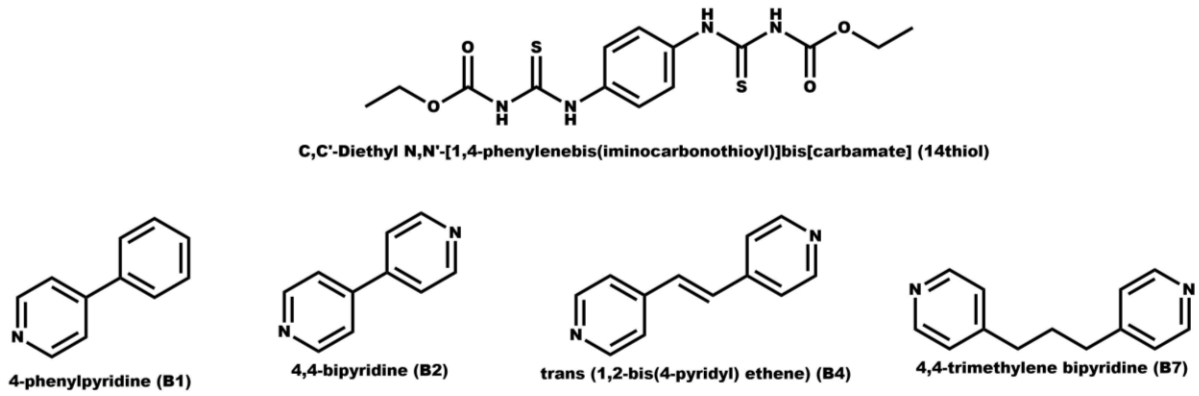

Scheme 3-2 Molecular structures of 14 thiol, and co-formers that successfully yielded new solid forms in this study.

3.2.Experimental

3.2.1. Reagents and General Methods

All reagents were used as received without any further purification. Hirshfeld surface analysis and two-dimensional fingerprint plots were generated and analyzed by using the CrystalExplorer 21.5 program.[16] All the NMR data was recorded on a Bruker 400 MHz spectrophotometer. Single crystal X-ray diffraction (SCXRD) data were obtained using a Rigaku XtaLAB Synergy-S with a CuKα source. The melting points were collected using a TA instrument DSC Q20 differential scanning calorimeter.

3.2.2. Synthesis of diethyl (1,4-phenylenedicarbamothyl) dicarbamate (14thiol)

The synthesis of **14thiol** was achieved by adding powdered potassium thiocyanate (12 mmol), to an ethyl acetate solution of ethyl chloroformate (10 mmol) and TMEDA (0.1

mmol). The reaction mixture was stirred at room temperature for 5 hr. Then the 1,4-phenylene diamine (5 mmol) was slowly added to the reaction mixture with constant stirring. The reaction mixture was stirred at room temperature for another 5 hrs. The product was concentrated using rotavapor and the product was obtained from washing with 10 mL 75% ethanol three times and 15 mL water three times. Yield: 80%. Mp 221-223 °C. ^{1}H NMR (400 MHz, DMSO-d6): δ 11.55 (s, 2H), δ 11.28 (s, 2H), 8.77 (d, J = 5.8 Hz, 2H), 8.47 (d, J = 2.6 Hz, 1H), 8.23 (d, J = 8.9 Hz, 1H), 7.99 (dd, J = 8.9, 2.7 Hz, 1H), 7.90 (d, J = 5.9 Hz, 2H).

3.2.3. Crystallization experiments

3.2.3.1. Synthesis of 1,4-phenylenedicarbamothyl) dicarbamate (14thiol-*form I*)

Stoichiometric amounts of **14thiol** (5 mg) and 4,4-trimethylene bipyridine, **B7** (23 mg) were ground in a 1:2 molar ratio using liquid assisted grinding (LAG) and the resulting solids were analyzed using IR spectroscopy. The resulting solid was dissolved in a 6:4 v/v mixture of ethyl acetate and nitromethane (**S3**) and kept in a small vial for slow evaporation at room temperature to get single crystals. Crystals suitable for single-crystal X-ray diffraction were obtained after 7-10 days and yielded **14thiol-*form I***. The melting point of the crystal was 216-217°C.

3.2.3.2. Synthesis of 1,4-phenylenedicarbamothyl) dicarbamate (14thiol-*form II*)

Stoichiometric amounts of **14thiol** (5 mg) and 1,2,4,5-tetrafluoro-3,6-diiodobenzene **H5** (23 mg) were ground in a 1:2 molar ratio using SAG and the resulting solids were analyzed using IR spectroscopy. The resulting solid was dissolved in a 6:4 v/v mixture of ethyl acetate and nitromethane (**S3**) and kept in a small vial for slow evaporation at room temperature to get single crystals. Crystals suitable for single-crystal X-ray diffraction were obtained after 7-10 days and yielded **14thiol-*form II***. The melting point of the crystal was 226-229°C.

3.2.3.3. Synthesis of 1,4-phenylene(dicarbamothyl) dicarbamate dioxane solvate (14thiol·S5)

Stoichiometric amounts of **14thiol** (5 mg) and 4,4-dimethyl-2,2-bipyridine, (5 mg) were ground in a 1:2 molar ratio using SAG and the resulting solids were analyzed using IR spectroscopy. The solid mixture was dissolved in 1,4-dioxane and the solvate was obtained from a failed co-crystallization. The melting point of the crystals was 171-172°C.

3.2.3.4. Synthesis of 1,4-phenylenedicarbamothyl) dicarbamate Di-(4-phenylpyridine) co-crystal 14thiol·$(B11)_2$

Stoichiometric amounts of **14thiol** (5 mg) and **B11** (5.4 mg) were ground in a 1:2 molar ratio using SAG and the resulting solids were analyzed using IR spectroscopy. The resulting solid was dissolved in a 6:4 v/v mixture of ethyl acetate and nitromethane (**S3**)

and kept in a small vial for slow evaporation at room temperature to get single crystals. Crystals suitable for single-crystal X-ray diffraction were obtained after 7-10 days. The melting point of the crystals was 216-217°C.

3.2.3.5. Synthesis of 1,4-phenylenedicarbamothyl) dicarbamate bis-(4,4-bipyridine) co-crystal 14thiol·$(B2)_2$

Stoichiometric amounts of **14thiol** (5 mg) and **B2** (8.4 mg) were ground in a 1:4 molar ratio using SAG and the resulting solids were analyzed using IR spectroscopy. The resulting solid was dissolved in a 6:4 v/v mixture of ethyl acetate and nitromethane (**S3**) and kept in a small vial for slow evaporation at room temperature to get single crystals. Crystals suitable for single-crystal X-ray diffraction were obtained after 7-10 days. The melting point of the crystal was 179-181°C.

3.2.3.6. Synthesis of bis[(1,4-phenylenedicarbamothyl) dicarbamate)] (trans)1,2-bis(4-pyridyl ethene) co-crystal ($14thiol)_2$·B4

Stoichiometric amounts of **14thiol** (5 mg) and **B4** (5 mg) were ground in a 1:4 molar ratio using SAG and the resulting solids were analyzed using IR spectroscopy. The resulting solid was dissolved in a 6:4 v/v mixture of ethyl acetate and nitromethane (**S3**) and kept in a small vial for slow evaporation at room temperature to get single crystals. Crystals suitable for single-crystal X-ray diffraction were obtained after 7-10 days. The melting point of the crystals was 193-195°C.

3.2.3.7. Synthesis of 1,4-phenylenedicarbamothyl) dicarbamate 4,4-trimethylene bipyridine co-crystal solvate (14thiol·B7)

Stoichiometric amounts of **14thiol** (5 mg) and 4,4-trimethylene bipyridine, **B7** (5.4 mg) were ground in a 1:2 molar ratio using SAG and the resulting solids were analyzed using IR spectroscopy. The solvate was produced by dissolving the solid mixture in 3-4mL tetrahydrofuran (THF). The melting point of the crystals was 125-129°C.

3.3. Theory: Hirshfeld analysis

The Hirshfeld surface analysis arose from an attempt to define the space filled by a molecule in a crystal structure in order to separate the crystal electron density into molecular fragments.[22, 23] Hirshfeld surfaces were named after F.L Hirshfeld. He proposed a method to describe the environment of an atoms in a molecule.[24] In his work, he constructed a weight function, $w_a(\mathrm{r})$, for each atom in a molecule as calculated by equation 3.3.1:

$$w_a(\mathrm{r}) = \rho_i^{at}(r) \,/ \sum_{i\epsilon\, molecule} \rho_i^{at}(r) \qquad (3.3.1)$$

where $\rho_i^{at}(r)$ are spherically averaged electron densities of the various atoms. In order to make this strategy applicable to molecules in a crystal lattice, Spackman and Byrom[25] adopted and extended this principle to define a weight function ($w_A(\mathrm{r})$) for a molecule in a crystal as:

$$w_A(\mathrm{r}) = \sum_{i\epsilon\ molecule\ A} \rho_i^{at}(r) \ / \sum_{i\epsilon\ crystal} \rho_i^{at}(r) \qquad (3.3.2)$$

$$= \rho_{promolecule}(r) \ / \ \rho_{procrystal}(r)$$

where $\rho_i^{at}(r)$ is a spherical atomic electron distribution located at the ith nucleus. The Hirshfeld surface is defined by an isosurface $w_A(\mathrm{r})$ of 0.5 and describes the volume of space where the promolecule electron density exceeds that of all neighbouring molecules. The distance between the Hirshfeld surface and the nearest atom outside the surface is marked by d*e*, and the distance between the surface and the nearest atom within the surface is denoted by d*i*. These distances may be projected onto the Hirshfeld surface to produce a three-dimensional representation of the intermolecular interactions in a crystal structure, but their application has limits. Consequently, a normalised contact distance, d_{norm}, is used to overcome these limitations.[26] The contact distance is normalised according to the formula:

$$d_{\mathrm{norm}} = \frac{d_i - r_i^{vdW}}{r_i^{vdW}} + \frac{d_e - r_e^{vdW}}{r_e^{vdW}} \qquad (\mathrm{eq.}\,11)$$

where r^{vdW} is the van der Waals radius of the specified atom inside or outside the surface, and d_{i} and d_{e} are the distances from the surface to the nearest atom inside and outside respectively. Since its inception, d_{norm} has been applied to investigate the intermolecular interactions in a crystal structure.[27-30] The 3D Hirshfield surface is represented as 2D fingerprint plots, which provide a breakdown of the intermolecular interactions as well as their contributions to the total Hirshfield surface. The form of the

2D plots, together with the percentage contributions of the intermolecular interaction, have been used to analyze crystal packing.[31, 32] Here we apply the same principle to correlate the observed physical properties of the multicomponent crystals to the intermolecular interactions in the crystal structure.

3.4.Results and Discussions

3.4.1. Crystal structure analysis

A total of five novel co-crystals and two polymorphs were isolated by conventional solvent evaporation methods. Crystal structure analysis of the two polymorphs (form I and II) showed that **14thiol-*form I*** crystallizes in a monoclinic space group while **14thiol-*formII*** crystallizes in the triclinic space group. The two polymorphic forms exhibit similar types of intermolecular interactions. First, an intramolecular N–H···O C hydrogen bond is observed within both 'arms' of the molecule. The lattice formation is stabilized by two types of dimers: first, the N–H···S=C hydrogen bonded dimer as well as the N–H···O=C hydrogen bonded dimer. In both polymorphs each **14thiol** molecule is hydrogen bonded with 8 hydrogen bonds in all to four adjacent **14thiol** molecules (Fig. 3-1(a), 3-1(b)). These arrangements produce infinite two-dimensional sheets of **14thiol** molecules that then stack on each other like those in form I with hydrophobic interactions between the ethyl and benzene groups (Fig. 3-1(c), 3-1(d)). It is interesting that synthons and crystal packing are very similar in both polymorphs despite crystallizing in different crystal systems.

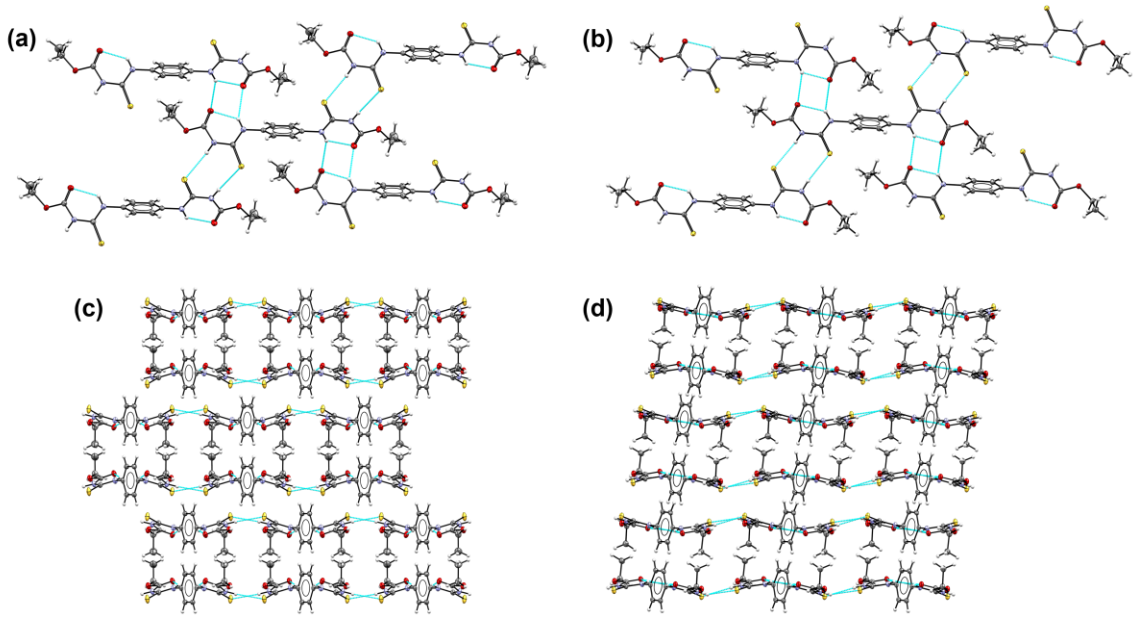

Figure 3-1 Single crystal structure of **14thiol-*formI*** and **14thiol-*formII*** showing (a) extended H-bonding motif in **14thiol-*formI***, (b) extended H-bonding motif in **14thiol-*formII***, (c) packing of the infinite chains in **14thiol-*formI***, (d) packing of the infinite chains in **14thiol-*formII***.

Table 3-1 Crystal structure data of the polymorphs

Compounds	**14thiol-*formI***	**14thiol-*formII***
Molecular formula	$C_{14}H_{18}N_4O_4S_2$	$C_{14}H_{18}N_4O_4S_2$
Formula weight (g mol^{-1})	370.44	370.44
Crystal system	monoclinic	triclinic
Space group (No.)	C 2yc (No. 15)	P-1 (No. 2)
a (Å)	11.6168(5)	8.9101(2)
b (Å)	18.3781(7)	9.3926(3)
c (Å)	9.2249(4)	10.7184(3)
α (°)	90	110.731(3)
β (°)	120.5770(10)	98.306(2)
γ (°)	90	93.097(2)
V ($Å^3$)	1695.60(12)	824.76(4)
Z	4	2
ϱ_{calc} (g cm^{-3})	1.451	1.492
μ (Cu Kα) (mm^{-1})	3.095	3.181
F (000)	776	388
Crystal size (mm)	0.3x0.1x0.03	0.2x0.12x0.06
Temperature (K)	200 (2)	100.00(16)
Radiation (Å)	CuKα, 1.54178	CuKα, 1.54184
Theta min/max (°)	4.812, 70.137	4.480, 77.237
Dataset	-13:13; -21:21; -9:10	-11:11; -10:11; -13:13
Final R indices [I>2.0 σ(I)]	R_1=0.0432 wR_2=0.1104	R1=0.0372 wR2=0.1063
R indices [all data]	R_1=0.0440 wR_2= 0.1114	R_1=0.0389 wR_2=0.1074
Tot., uniq. data, R (int)	7434,1491, 0.0435	11150, 3204, 0.0270
N_{ref}, N_{par}	1543; 119	3416; 219
S	1.101	1.082
Max. and av. Shift/error	0.000, 0.000	0.001, 0.000
Min. and max. resd. Dens ($Å^3$)	-0.435, 0.479	-0.349, 0.368

Table 3-2 Crystal structure data of the multicomponent crystals obtained.

Compounds	**14thiol·(B1)$_2$**	**14thiol·(B2)$_2$**	**(14thiol)$_2$·B4**	**14thiol·S5**	**14thiol·B7**
Molecular formula	$C_{36}H_{36}N_6O_4S_2$	$C_{34}H_{34}N_8O_4S_2$	$C_{26}H_{28}N_6O_4S_2$	$C_{22}H_{34}N_4O_4S_2$	$C_{31}H_{38}N_6O_5S_2$
Formula weight (g mol^{-1})	680.83	684.81	552.66	546.65	638.79
Crystal system	monoclinic	triclinic	triclinic	triclinic	triclinic
Space group (No.)	*P*2$_1$/c (No. 14)	*P- 1* (No. 2)	*P- 1* (No. 2)	*P- 1* (No. 2)	*P- 1* (No. 2)
a (Å)	12.2999(2)	7.1278(3)	7.5301(18)	6.9655(2)	10.5977(3)
b (Å)	18.5792(3)	9.5251(4)	12.785(3)	9.4937(2)	11.1277(3)
c (Å)	7.2675(10)	12.2227(5)	14.019(3)	11.0764(3)	13.9507(3))
α (°)	90	97.8640(10)	99.273(5)	99.1430(10)	88.3708(19)
β (°)	91.610(10)	91.0290(10)	97.920(5)	95.3730(10)	73.003(2)
γ (°)	90	97.8450(10)	91.815(5)	109.7300(10)	83.8766(19)
V (Å^3)	1660.13 (4)	813.77(6)	1317.3(5)	672.10(3)	1564.33(7)
Z	2	1	2	1	2
ϱ_{calc} (g cm^{-3})	1.362	1.393	1.393	1.351	1.356
μ (Cu Kα) (mm^{-1})	1.862				1.957
F (000)	716	358	580	290	676
Crystal size (mm)	0.14x0.12x0.105	0.175x0.13x0.045	0.19x0.17x0.15	0.19x0.095x0.09	0.52x0.30x0.15
Temperature (K)	200 (2)	200 (2)	200 (2)	200 (2)	100 (10)
Radiation (Å)	CuKα, 1.54178	CuKα, 1.54178	CuKα, 1.54178	CuKα, 1.54178	CuKα, 1.54178
Theta min/max (°)	3.595, 70.442	3.653, 68.092	3.228, 68.414	4.094, 69.724	6.626, 154.83
Dataset	-11:11; 0:25; 0:15	-	-8:8; -14:15; -15:16	-7:8; -11:11; -13:13	-13:13; -14:13; -17:13
Final R indices [I>2.0 σ(I)]	R_1=0.0337, wR_2=0.0853	R_1=0.0329 wR_2=0.0888	R_1=0.0465 wR_2=0.1408	R_1=0.0538 wR_2=0.1465	R_1 = 0.0600, wR_2 = 0.1629
R indices [all data]	R_1=0.0345 wR_2= 0.0858	R_1=0.0350 wR_2= 0.0907	R_1=0.0500 wR_2=0.1551	R_1=0.0544 wR_2=0.1469	R_1 = 0.0622, wR_2 = 0.1648
Tot., uniq. data, R (int)	14940, 2960, 0.0256	9846, 2741, 0.0277	10771, 4167, 0.0344	9036, 2307, 0.0290	24086,6501, 0.0348
N_{ref}, N_{par}	3076; 227	2930; 226	4501, 362	2369; 193	6501; 400
S	1.080	1.042	1.119	1.163	1.108
Max. and av. Shift/error	0.002, 0.000	0.000, 0.000	0.000, 0.000	0.000, 0.000	0.000, 0.000
Min. and max. resd. Dens (Å^3)	-0.229, 0.330	-0.266, 0.199	-0.329, 0.609	-0.318, 0.798	1.02/-0.76

The **14thiol-S5** solvate crystallizes in the monoclinic space group $P\bar{1}$. The asymmetric unit consists of one 14thiol molecule and two dioxane molecules. As shown in (Figure 3-2a), the two components interact with each other via the N7–H7---O14 hydrogen bond, and the same 14thiol molecule connects with another adjacent S5 molecule through the N4–H4---O16 hydrogen bond. As expected, the *intramolecular* N–H---O=C hydrogen bond is observed but not the N–H---S and N–H---O=C dimers previously seen in the two polymorphs. There are two types of dioxanes (red and green) by symmetry equivalence as shown by the 2D hydrogen-bonding network, which extends to form sheets (Figure 3-2b). The overall packing shows the stacking of the sheets as well as how the dioxane solvent molecules occupy the voids between the 14thiol molecules to maximize packing efficiency (Figure 3-2c).

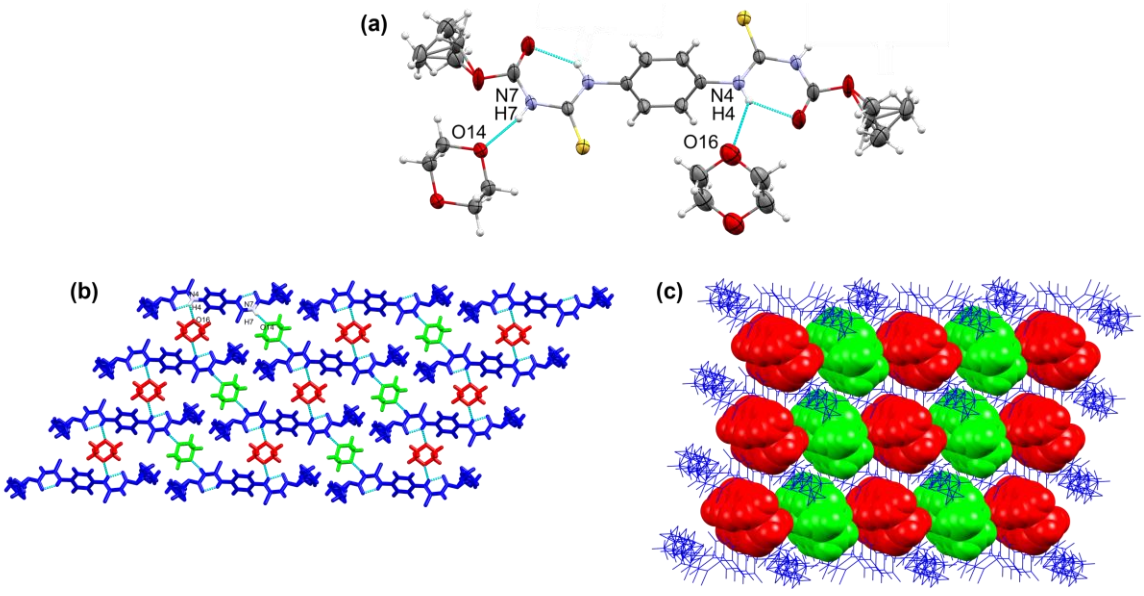

Figure 3-2 Single crystal structure of **14thiol·S5** showing (a) hydrogen bonding between the target and dioxane molecules (b) extended H-bonding showing the molecules colored by symmetry equivalence 14thiol (blue), dioxane (red and green) (c) crystal packing of the structure with dioxane molecules in space fill.

14thiol·(B1)$_2$ co-crystallizes in the *P*2$_1$/*c* space group, with one 14thiol molecule and two B11 molecules in the asymmetric unit, which interact via the N7–H7---O16 hydrogen bond (Figure 3-3a). As shown in (Figure 3-3b), the extended H-bonding bonding network shows formation of a layer comprising cross-linked chains (highlighted in blue). The crystal packing is completed by stacking of layers, but no specific interlayer interactions are observed. (Figure 3-3c).

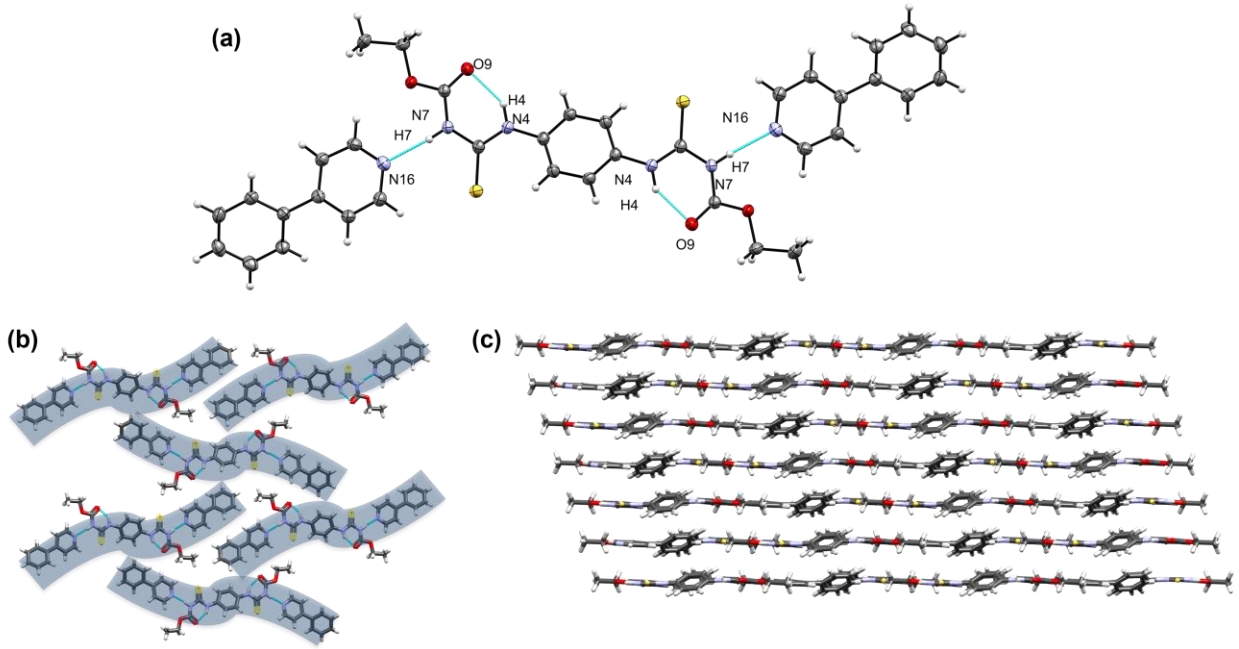

Figure 3-3 Single crystal structure of **14thiol·(B1)$_2$** co-crystal showing (a) primary hydrogen bonding (b) extended H-bonding forming discrete chains (c) packing of co-crystal into stacked layers.

The **14thiol·(B2)$_2$** crystallizes in the space group *P*$\bar{1}$. The asymmetric unit consists of one **14thiol** molecule and two **B2** molecules. As shown in (Figure-3-4a), the two components interact with each other via the N7–H7---N16 hydrogen bond. It was interesting to

observe that while the co-former, B2, is a bipyridine only one acceptor, N16 participated in H-bonding while N22 did not interact at all. The trimeric units assemble into parallel chains (in blue and red) as shown by the 2D hydrogen-bonding network (Figure 3-4b). The overall packing shows the stacking of the chains and weak C=S---H-C(ring) interactions are present between the chains (Figure 3-4c).

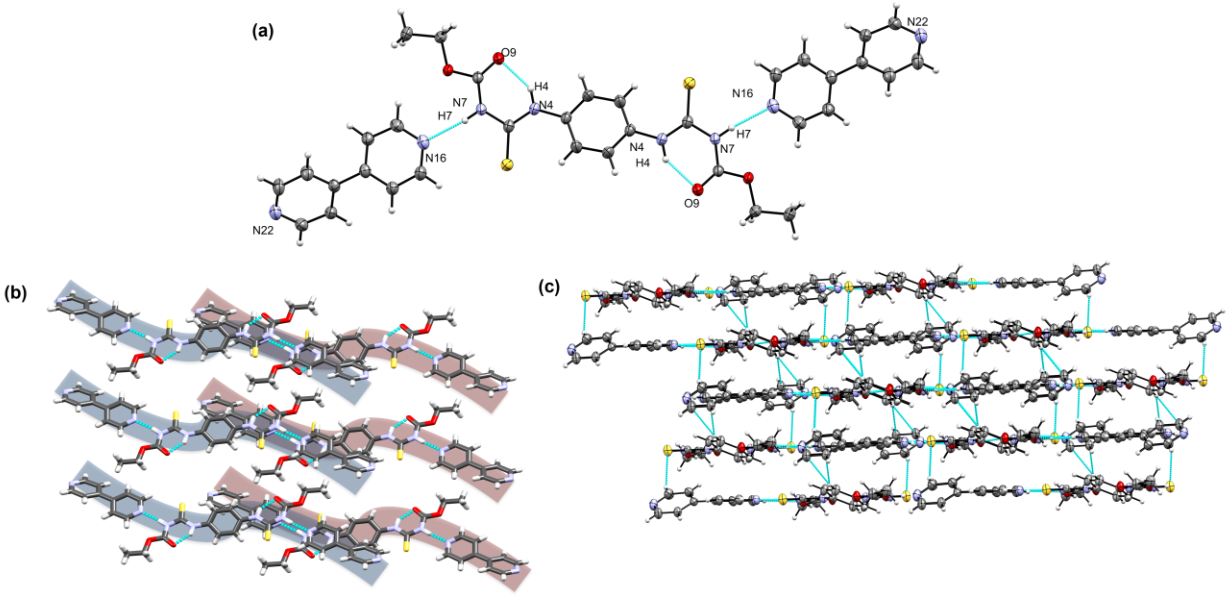

Figure 3-4 Single crystal structure of 1**4thiol·(B2)**$_2$ co-crystal showing (a) primary hydrogen bonding (b) extended H-bonding forming discrete chains (c) packing of co-crystal into stacked layers showing interlayer interactions.

Co-crystallization of **14thiol** and **B4** yielded (**14thiol**)$_2$**·B4** in the triclinic space group $P\bar{1}$. The asymmetric unit consists of two **14thiol** molecules and one **B4** molecule. Unlike in **14thiol·(B2)**$_2$ where only one N_{pyr} acceptor participated, here both acceptors of the co-former are involved in hydrogen bonding. As shown in (Figure 3-5a), one N_{pyr} interacts

with **14thiol** via N7–H7---N16 while the other connects with an adjacent **14thiol** molecule through the N19–H19---N30 hydrogen bond. The extended H-bonding network forms infinite wavelike chains as (Figure 3-5b). The crystal lattice shows the aggregation of intertwined wavelike chains (Figure 3-5c). (**14thiol)$_2$·B4** has a unique packing compared to all other cocrystals/solvates in this series in that the chains formed *between* the target and co-former are infinite wavelike fashion whereas discrete chains are observed for all other structures.

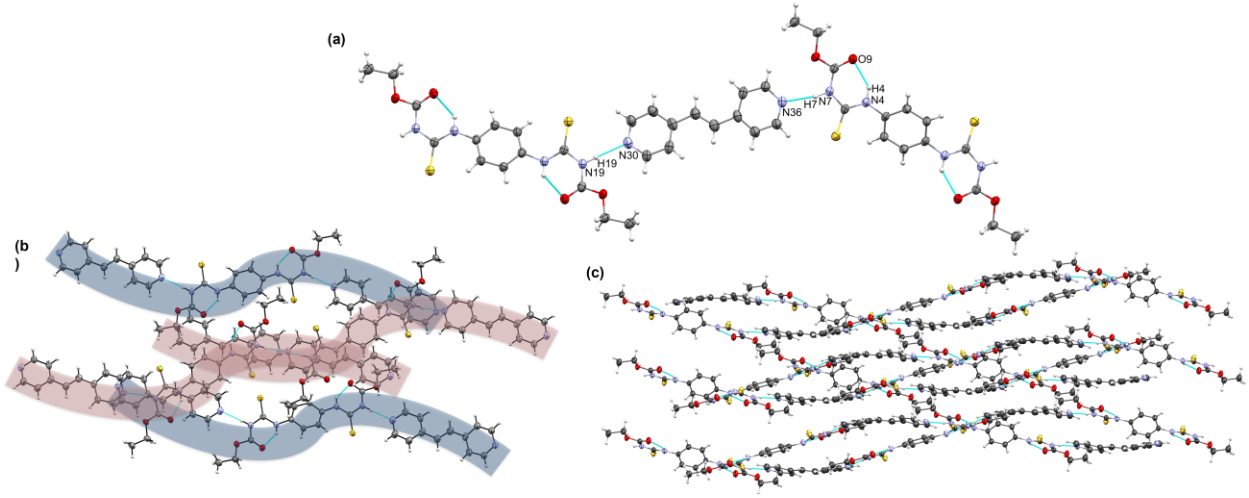

Figure 3-5 Single crystal structure of (**14thiol)$_2$·B4** co-crystal showing (a) primary hydrogen bonding (b) extended H-bonding forming infinite chains (c) packing of co-crystal into intertwined chains.

The **14thiol·B7** crystallizes in the triclinic space group $P\bar{1}$. The asymmetric unit consists of one **14thiol** molecule, one **B7** molecule and one tetrahydrofuran (THF) molecule. In this structure, both co-former N_{pyr} acceptors interact with the target through N18–H18---N25 and N9–H9---N34 hydrogen bond interactions (Figure3-6a). A notable structural

difference in **14thiol·B7** is that the sulfur atoms are *syn-*, lying to one-side of the plane of the central aromatic ring while in **all other structures** the sulfur atoms occupy the *anti-* position. Similar to **(14thiol)$_2$·B4,** the extended H-bonding network in **14thiol·B7** forms infinite wavelike chains as in (Figure 3-6b). The wavelike chains assemble to form layers that stack and no interlayer interactions are observed. Also, unlike in **14thiol·S5** solvate where the dioxane molecules form hydrogen bonding with the **14thiol**, here the THF molecules do not interact but just occupy void space (Figure 3-6c).

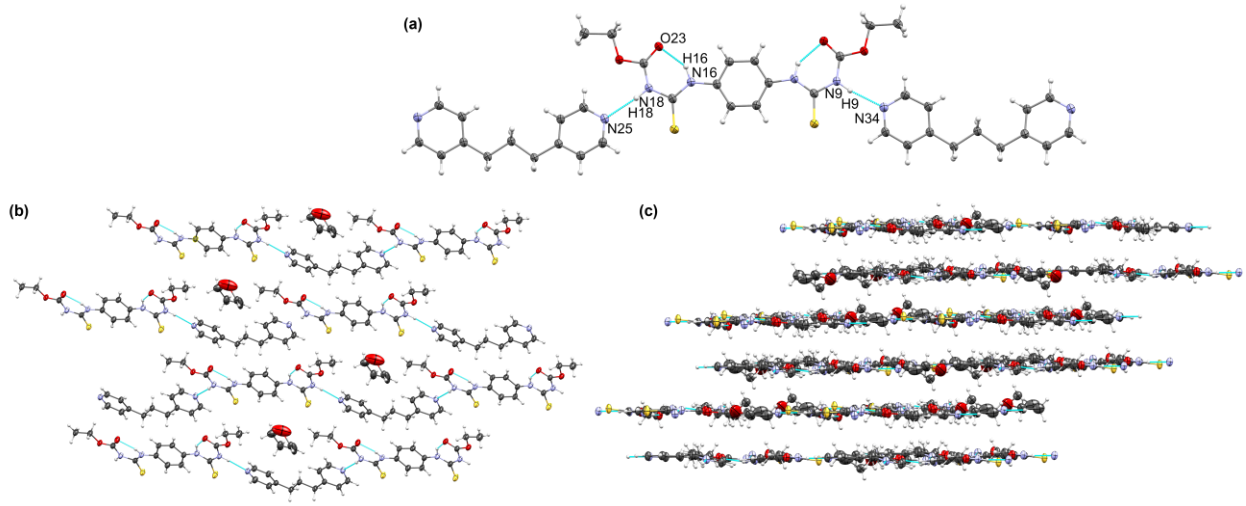

Figure 3-6 Single crystal structure of **14thiol·B7** co-crystal solvate showing (a) primary hydrogen bonding (b) extended H-bonding forming infinite chains (c) packing of co-crystal into stacked layers.

3.4.2. Conformational Analysis

Previously reported structures of thiophanates exhibited conformational flexibility which inspired us to investigate the conformations of the molecules in the different structures since these molecules can potentially adopt different conformations. The two

polymorphs isolated in this study exhibited same synthon arrangements and very similar crystal packings and a comparison in the bond rotation was completed to get a more precise measure of the conformational differences of the molecules in the two polymorphs. Furthermore, the torsion angles of the target molecule (**14thiol**) in each co-crystal/solvate was also measured. Designators **τ1** (orange) and **τ2** (red) were used to differentiate two torsion angles between left and right 'wings' of the **14thiol** molecule, which mainly differ in the conformation of the two wings relative to the phenyl ring (Figure 3.7).

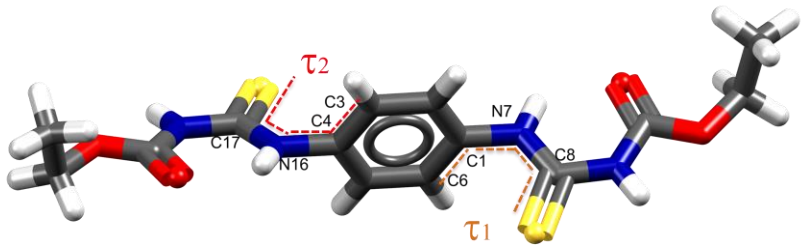

Figure 3-7 Graphical representation of the torsion angles of **14thiol.**

In form I, both wings exhibit the same conformation with both **τ1** and **τ2** angles around ~71(2)° (Figure 3-8). Interestingly, unlike form I there is notable difference in torsions of the two wings in form II with **τ1** around ~79(2)°and **τ2** angle ~73(2)°. The conformational flexibility of the two wings allows for a significant conformational and geometrical change of the molecule. The torsion angles of the two polymorphs suggest that **14thiol** exhibits conformational polymorphism.

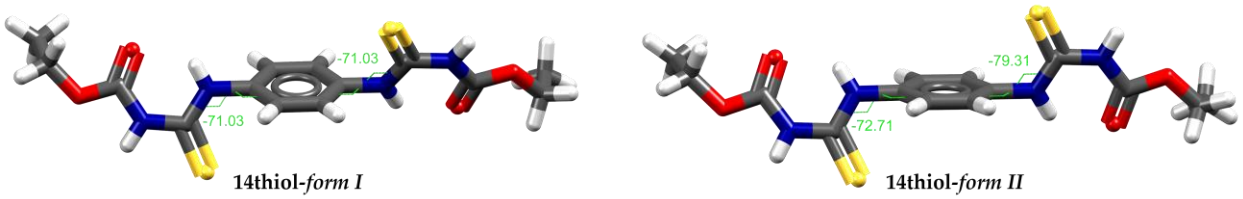

Figure 3-8 Measured torsion angles in **14thiol-*form I*** and **14thiol-*form I***.

Further analysis was performed on the other multicomponent crystals obtained in this study. The values of the torsion angles for the seven multicomponent crystals presented in this work are listed in (Table 3.3). The torsion angles of the **14thiol** molecules suggest that the molecules in the multicomponent crystals adopt three types of conformations. First, the **14thiol-*form I***, **14thiol-*form II***, and dioxane solvate **14thiol·S5** have torsion angles within 71-80° range. This orientation of molecules has the two wings of the molecules almost perpendicular (90°) to the central phenyl ring as indicated by the torsion angles. Second, the co-crystals with the pyridine co-formers **14thiol·(B1)$_2$,** **14thiol·(B2)$_2$**, and **(14thiol)$_2$·B4** have torsion angles within the 28-45° range. The final orientation observed was for the co-crystal solvate of **14thiol·B7.** In this structure the 14thiol adopted a unique geometry whereby both the thiocarbamate wings were syn positioned (facing the same direction) with torsion angles of 11 and 7°. The **14thiol** molecules are near-planar with respect to the phenyl ring and this example shows the extent to which the target molecule can be flexible to accommodate the THF solvent and

4,4-trimethylene bipyridine coformer in the crystal lattice. Figure 3.9 shows the molecular overlay of **14thiol** molecules from structures formed which shows all conformations.

Table 3-3 Related torsion angles and standard deviation in parenthesis of **14thiol** from all the multicomponent crystals reported in this study.

Structure	τ1 (°)	τ2 (°)
14thiol-*form I*	71(2)	71(2)
14thiol-*form II*	79(2)	72(2)
14thiol·S5	71(3)	71(3)
14thiol·(B1)$_2$	35(2)	35(2)
14thiol·(B2)$_2$	28(2)	28(2)
(14thiol)$_2$·B4	42(4) 26(4)	42(4) 26(4)
14thiol·B7	11(4)	7(4)

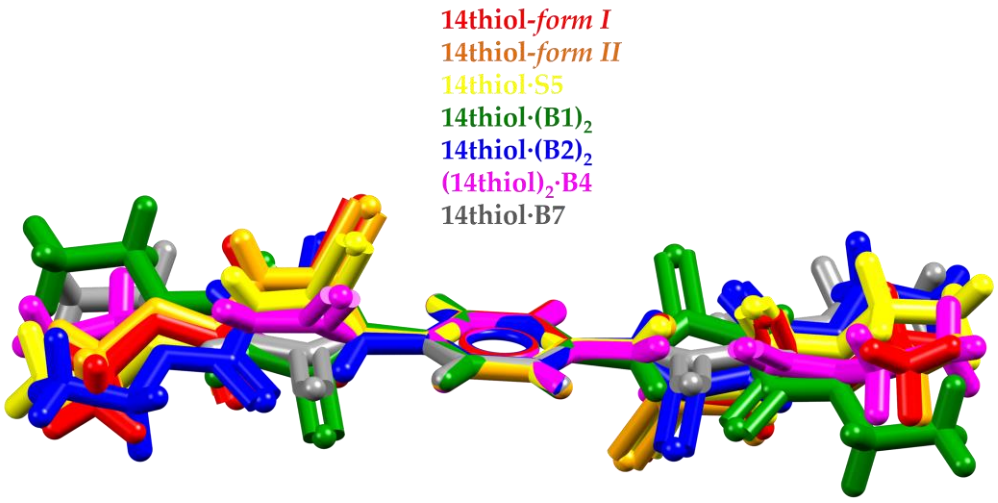

Figure 3-9 The superimposed molecules of **14thiol** from structures formed.

3.4.3. Hirshfeld Surface Analysis

The Hirshfeld surface analysis was utilized to investigate and visualize different types of intermolecular interactions in the crystals and 2D fingerprint plots provided quantitative

information about the interactions. Figure 3-10 illustrates the Hirshfeld surfaces of **14thiol** that have been mapped over d_{norm}, where the large circular depressions (deep red) stand for the hydrogen bonding contacts (i.e., N–H---S=C, N–H---O=C and N–H---N, N–H---O) whereas other visible spots represent the H---H contacts.

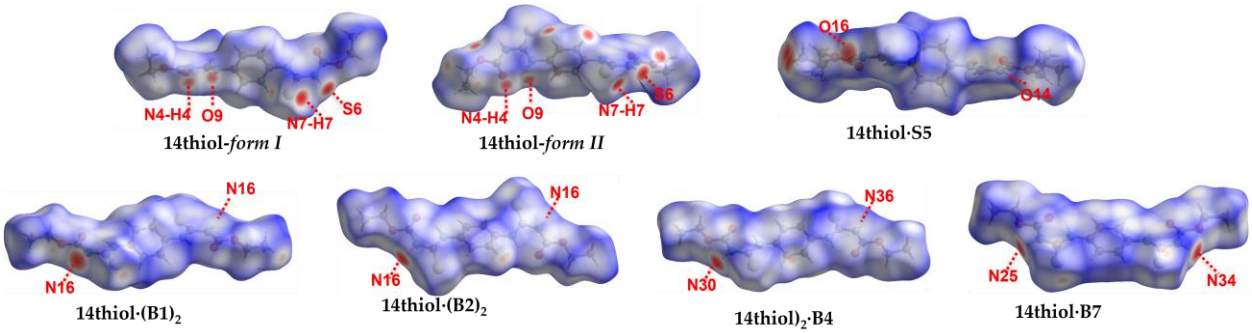

Figure 3-10 Hirshfeld surfaces in **14thiol** multicomponent crystals.

The corresponding 2D fingerprint plots are demonstrated in (Figure 3-11). Five contacts are the most significant contacts in all seven crystal structures. Notably, the hydrogen bonding contacts S---H, O---H and N---H appear as spikelike tips, while H---H contacts appear as asymmetric points spread over a large area, and the C---H contacts appear as a symmetric pair of wings. The H---H contacts make the largest contribution, which is to be expected since the limited hydrogen-bonding sites result in the increase of the contribution of the van der Waals force to stabilize the lattice. The S---H contacts are the second largest contributor, and this is due to the contacts being observed in the crystal packing and these contacts stabilize the lattice.

The structured **14thiol-*form I***, **14thiol-*form II***, and **14thiol·S5** had the highest O---H contacts due to the presence of N–H---O=C dimers in the polymorphs and N–H---O interactions in the dioxane solvate. The N---H contacts are least in these three structures since the former mentioned interactions hold the lattice together. Upon co-crystal formation with pyridine co-formers in **14thiol·(B1)$_2$, 14thiol·(B2)$_2$**, **(14thiol)$_2$·B4**, and **14thiol·B7** the N---H contacts increase significantly as expected since N-H---N is the primary interaction in the structures. On the contrary, the O---H contacts reduce by almost half in these structures due to the disruption of the N–H---O=C dimers. Significant O---H contacts are still observed and that is expected since all structures form intramolecular N-H---O=C hydrogen bonds.

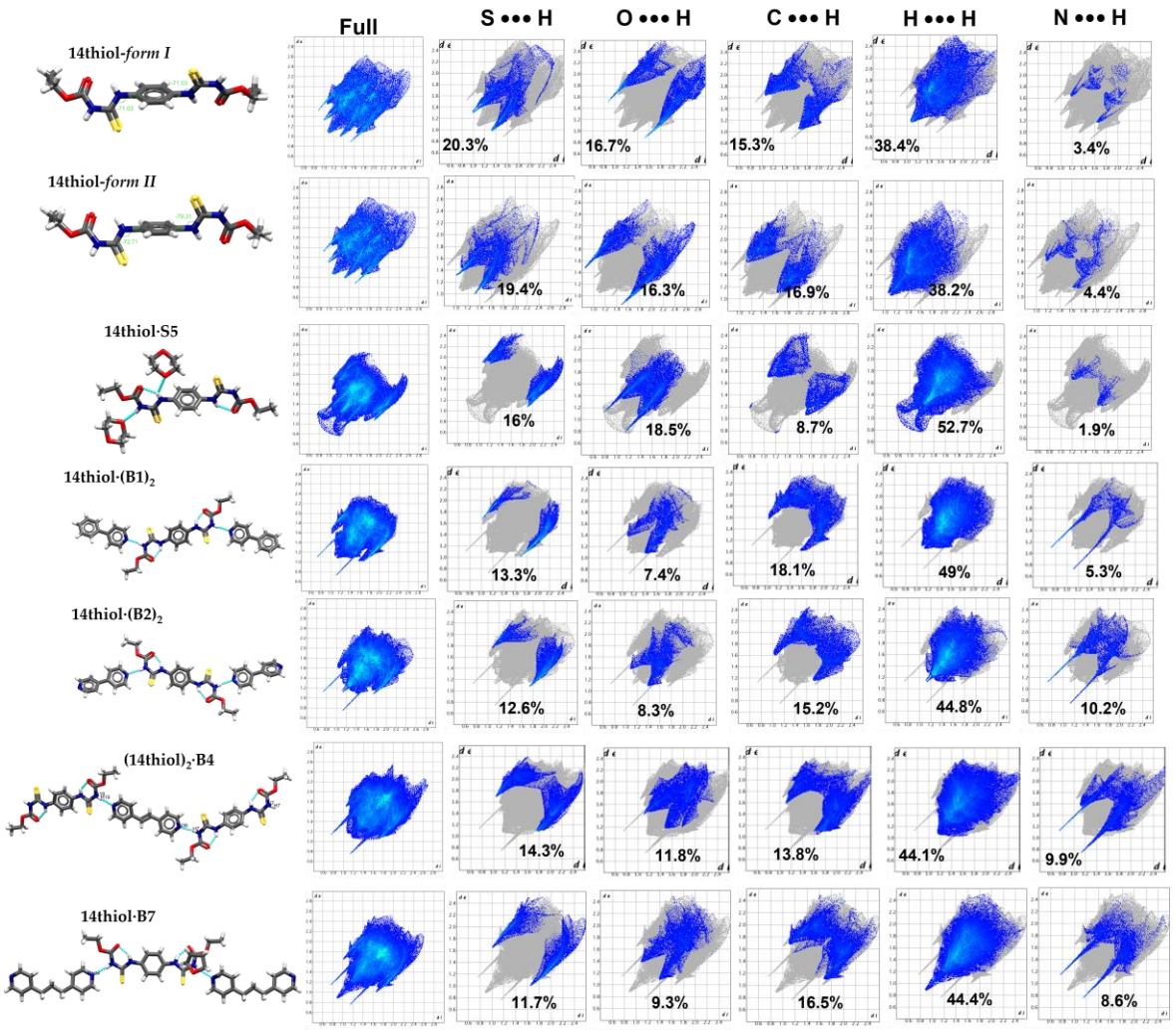

Figure 3-11 Summary of 2D fingerprint plots of the multicomponent crystals.

3.5. Conclusions

1. Introduction of pyridine-based co-formers disrupts the robust homomeric N–H---S=C and N–H---O=C hydrogen bonded dimers in **14thiol** with the formation of heteromeric N-H---N bonded crystals

2. The target **14thiol** is a versatile target for crystal engineering as it forms multicomponent crystals: two polymorphs of **14thiol**, one dioxane solvate, three co-crystal and one co-crystal solvate (THF).
3. Hirshfeld surface analysis revealed that the high acceptor ability in the coformers lead to the increase of hydrogen-bonding interactions (N-H---N) and a decrease of (O---H) contacts in **14thiol** cocrystals and vice versa.
4. Molecular geometry analysis shows that conformational flexibility is such a useful feature in driving co-crystallization because in this study **14thiol** adopted several conformations in different crystal structures to accommodate various co-formers thus yielding multicomponent solid forms.

3.6.References

1. Desiraju, G. R., Crystal Engineering: From Molecule to Crystal. *Journal of the American Chemical Society* **2013,** *135* (27), 9952-9967.
2. Aakeröy, C. B.; Salmon, D. J., Building co-crystals with molecular sense and supramolecular sensibility. *CrystEngComm* **2005,** *7* (72), 439-448.
3. Desiraju, G. R., Crystal Engineering: A Holistic View. *Angewandte Chemie International Edition* **2007,** *46* (44), 8342-8356.
4. Duggirala, N. K.; Perry, M. L.; Almarsson, Ö.; Zaworotko, M. J., Pharmaceutical cocrystals: along the path to improved medicines. *Chemical Communications* **2016,** *52* (4), 640-655.
5. Sinha, A. S.; Maguire, A. R.; Lawrence, S. E., Cocrystallization of Nutraceuticals. *Crystal Growth & Design* **2015,** *15* (2), 984-1009.
6. Bond, A. D., What is a co-crystal? *CrystEngComm* **2007,** *9* (9), 833-834.
7. Aakeröy, C. B.; Champness, N. R.; Janiak, C., Recent advances in crystal engineering. *CrystEngComm* **2010,** *12* (1), 22-43.
8. Desiraju, G. R., Supramolecular Synthons in Crystal Engineering—A New Organic Synthesis. *Angewandte Chemie International Edition in English* **1995,** *34* (21), 2311-2327.

9. Bernstein, J.; Davis, R. E.; Shimoni, L.; Chang, N.-L., Patterns in Hydrogen Bonding: Functionality and Graph Set Analysis in Crystals. *Angewandte Chemie International Edition in English* **1995,** *34* (15), 1555-1573.
10. Shunje, K. N.; Averkiev, B. B.; Aakeröy, C. B., Influence of Multiple Binding Sites on the Supramolecular Assembly of N-[(3-pyridinylamino) Thioxomethyl] Carbamates. *Molecules* **2022,** *27* (12), 3685.
11. Bruton, E. A.; Brammer, L.; Christopher Pigge, F.; Aakeröy, C. B.; Leinen, D. S., Hydrogen bond patterns in aromatic and aliphatic dioximes. *New Journal of Chemistry* **2003,** *27* (7), 1084-1094.
12. Etter, M. C., Encoding and decoding hydrogen-bond patterns of organic compounds. *Accounts of Chemical Research* **1990,** *23* (4), 120-126.
13. B. Aakeröy, C.; A. Evans, T.; R. Seddon, K.; Pálinkó, I., The C–H···Cl hydrogen bond: does it exist? *New Journal of Chemistry* **1999,** *23* (2), 145-152.
14. Alkorta, I.; Rozas, I.; Elguero, J., Non-conventional hydrogen bonds. *Chemical Society Reviews* **1998,** *27* (2), 163-170.
15. Musumeci, D.; Hunter, C. A.; Prohens, R.; Scuderi, S.; McCabe, J. F., Virtual cocrystal screening. *Chemical Science* **2011,** *2* (5), 883-890.
16. Spackman, P. R.; Turner, M. J.; McKinnon, J. J.; Wolff, S. K.; Grimwood, D. J.; Jayatilaka, D.; Spackman, M. A., CrystalExplorer: a program for Hirshfeld surface analysis, visualization and quantitative analysis of molecular crystals. *Journal of Applied Crystallography* **2021,** *54* (3), 1006-1011.
17. Bankiewicz, B.; Wojtulewski, S., Two New Cocrystals of the Dipicolinic Acid. Hirshfeld Atom Refinement of Crystal Structures and Quantum Theory of Atoms in Molecules Analysis of Molecular Complexes. *Crystal Growth & Design* **2019,** *19* (12), 6860-6872.
18. Yang, J.; Yin, L.; Gong, X.-D.; Sinditskii, V. P.; Zhang, J.-G., Origins of Salt Formation and Cocrystallization: A Combined Experimental and Theoretical Study. *Crystal Growth & Design* **2020,** *20* (9), 5834-5842.
19. Nauha, E.; Kolehmainen, E.; Nissinen, M., Packing incentives and a reliable N–H···N–pyridine synthon in co-crystallization of bipyridines with two agrochemical actives. *CrystEngComm* **2011,** *13* (21), 6531-6537.
20. Nauha, E.; Ojala, A.; Nissinen, M.; Saxell, H., Comparison of the polymorphs and solvates of two analogous fungicides—a case study of the applicability of a supramolecular synthon approach in crystal engineering. *CrystEngComm* **2011,** *13* (15), 4956-4964.
21. Nauha, E.; Saxell, H.; Nissinen, M.; Kolehmainen, E.; Schäfer, A.; Schlecker, R., Polymorphism and versatile solvate formation of thiophanate-methyl. *CrystEngComm* **2009,** *11* (11), 2536-2547.
22. Spackman, M. A.; Jayatilaka, D., Hirshfeld surface analysis. *CrystEngComm* **2009,** *11* (1), 19-32.

23. McKinnon, J. J.; Mitchell, A. S.; Spackman, M. A., Hirshfeld surfaces: a new tool for visualising and exploring molecular crystals. *Chemistry-A European Journal* **1998,** *4* (11), 2136-2141.
24. Hirshfeld, F. L., Bonded-atom fragments for describing molecular charge densities. *Theoretica chimica acta* **1977,** *44* (2), 129-138.
25. Spackman, M. A.; Byrom, P. G., A novel definition of a molecule in a crystal. *Chemical Physics Letters* **1997,** *267* (3–4), 215-220.
26. McKinnon, J. J.; Jayatilaka, D.; Spackman, M. A., Towards quantitative analysis of intermolecular interactions with Hirshfeld surfaces. *Chemical Communications* **2007,** (37), 3814-3816.
27. Luo, Y.-H.; Sun, B.-W., Pharmaceutical Co-Crystals of Pyrazinecarboxamide (PZA) with Various Carboxylic Acids: Crystallography, Hirshfeld Surfaces, and Dissolution Study. *Crystal Growth & Design* **2013,** *13* (5), 2098-2106.
28. Wood, P. A.; McKinnon, J. J.; Parsons, S.; Pidcock, E.; Spackman, M. A., Analysis of the compression of molecular crystal structures using Hirshfeld surfaces. *CrystEngComm* **2008,** *10* (4), 368-376.
29. J. McKinnon, J.; S. Mitchell, A.; A. Spackman, M., Visualising intermolecular interactions in crystals: naphthalene vs. terephthalic acid. *Chemical Communications* **1998,** (19), 2071-2072.
30. Batisai, E.; Ayamine, A.; Kilinkissa, O. E. Y.; Bathori, N. B., Melting point-solubility-structure correlations in multicomponent crystals containing fumaric or adipic acid. *CrystEngComm* **2014,** *16* (43), 9992-9998.
31. Bathori, N. B.; Nassimbeni, L. R.; Oliver, C. L., Quininium mandelates-a systematic study of chiral discrimination in crystals of diastereomeric salts. *Chemical Communications* **2011,** *47* (9), 2670-2672.
32. Bathori, N. B.; Kilinkissa, O. E. Y., Are gamma amino acids promising tools of crystal engineering? - Multicomponent crystals of baclofen. *CrystEngComm* **2015,** *17* (43), 8264-8272.

Chapter 4 - Influence of multiple binding sites on the supramolecular assembly of *N*-[(3-pyridinylamino) thioxomethyl] carbamates

4.1.Introduction

The ability to foresee and control the outcome of the organization and assembly of molecules is a highly coveted goal in the bottom-up synthesis of functional materials. Achieving this requires a better understanding of non-covalent intermolecular interactions between the building blocks and of the overall crystal packing arrangement of the molecules. From a practical perspective, manipulating intermolecular interactions has been used to establish structure-property-function correlation in applications such as molecular recognition,[1] design of mechanically flexible molecular crystals, [2-6] controlling thermal expansion behavior,[7] as well as design of molecular capsules.[8] In addition, an improved understanding of intermolecular interactions is essential if we want to control key crystallization events that lead to synthon polymorphism.[9-11]

Hydrogen bonding is the most extensively studied non-covalent interaction, followed by the halogen bond [12, 13]. They display similar strength and directionality, which can make it difficult to predict outcomes of how they will affect supramolecular assembly when functional groups that can accept hydrogen bonds and halogen bonds equally well are present in a system. Several strategies have been proposed to predict the outcome in cases

where multiple intermolecular interactions sites are present such as hydrogen-bond energy (HBE), and hydrogen-bond propensity (HBP) [14, 15]. Computing molecular electrostatic potential (MEP) maps is another method for analyzing the distribution of electron densities in molecular systems wherein the highest positive potential is classified as the best donor, and the highest negative potential as the best acceptor [16]. The ranking of these donor/acceptor sites can also shed light on which sites will preferentially bind to each other. To establish binding preference patterns in systems where both interactions can co-exist, Shimazu *et al*. carried out co-crystallization experiments of dipyridyloxalamide ligands with tetrafluorodiiodobenzenes [17].

The competing acceptors were pyridyl nitrogen and the carbonyl oxygen of the oxalamide groups as ranked by MEP and neither displayed specific binding preference to the tetrafluorodiiodobenzenes over the other. Resnati *et al.* also demonstrated that halogen and hydrogen bonding can exist orthogonally to construct porous organic frameworks.[18]

Of continued interest in our group is to establish binding preferences for systems with multiple acceptors that have significantly different electrostatic strengths. In previous studies, we carried out binding preference studies, including on heteroaryl-2-imidazoles with one hydrogen-bond (HB) donor and two or three different acceptor sites (ranked by

MEPs) using monotopic halogen-bond (XB) donor co-formers [19-22]. It was observed that XB donors outperformed the HB donor for the electrostatically most attractive acceptor site. In the current study, we explore a new target library decorated with the carbamate functional group.

Carbamate-bearing molecules and their derivatives[23-27] (Scheme 4-1) have wide-ranging applications in areas such as pesticides [28-31], active pharmaceutical ingredients[32, 33], and energetic materials [34-36]. Carbamates are also versatile compounds for crystal engineering because they contain multiple acceptor and donor sites such as carbonyl oxygen atom, pyridyl nitrogen atom, and C=S. However, this versatility also makes them challenging from an *a priori* design perspective.

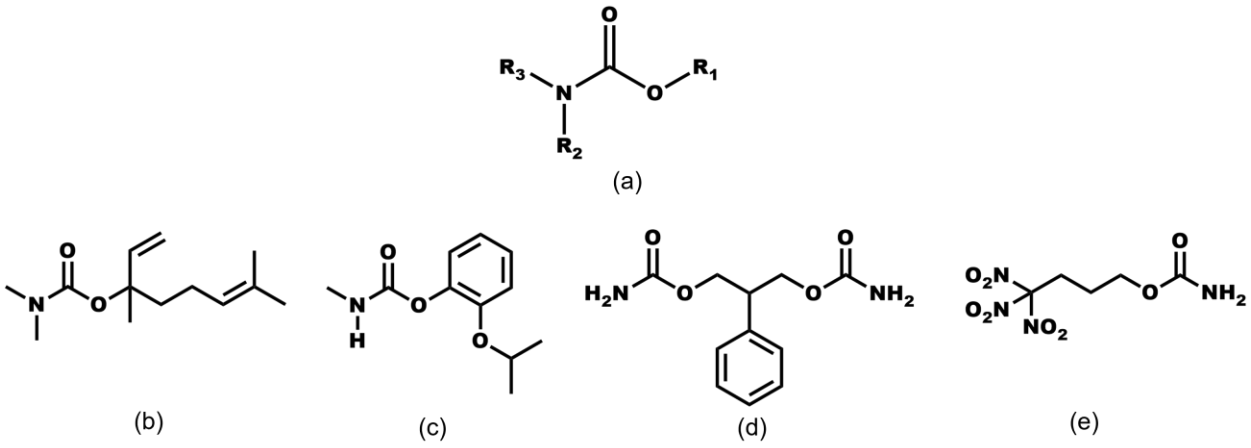

Scheme 4-1 (a) Carbamate moiety and carbamate bearing molecules (b) pepperwood (c) baygon (d) felbamate (e) trinitrobutyl nitrocarbamate.

In this study we address five specific questions.

- What is the impact of varying chain length (R= methyl, ethyl, and isobutyl) on the target molecule, **A1**-**A3**, crystal structures (Scheme 4-2)?
- Which structure directing synthons are formed when targets are co-crystallized [37-39] with halogen bond donor co-formers?
- What binding preference is observed in the solid state when hydrogen-bond and halogen-bond donors (**D1** and **D2**) compete for three acceptor sites (Scheme 2)?
- Does the supramolecular assembly change for different targets if we introduce the same XB donors as co-formers for co-crystallization?
- How reliable are MEP rankings/predictions when multiple acceptors are present on the target molecules?

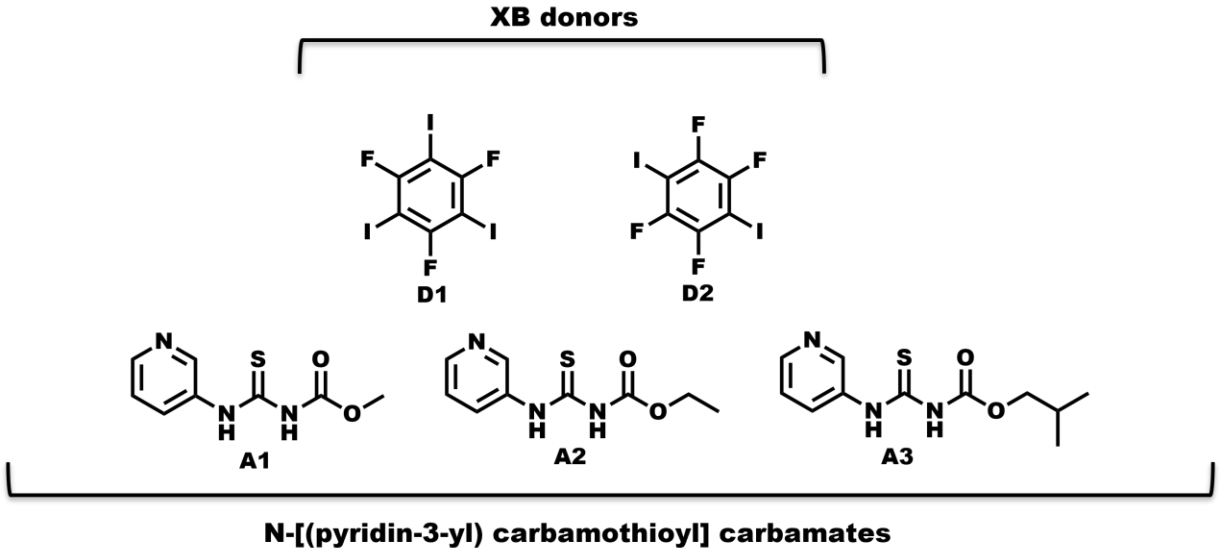

Scheme 4-2 Molecular structures of R-N-[(3-pyridinylamino) thioxomethyl] carbamate and two halogen bond donors used in this study.

An attempted co-crystallization of the target compounds with XB donors can result in the target and co-former precipitating separately in which case it would be a recrystallization. On the other hand, if halogen bonding is structure directing it can lead to formation of a co-crystal via various postulated synthons (Scheme 4-3).

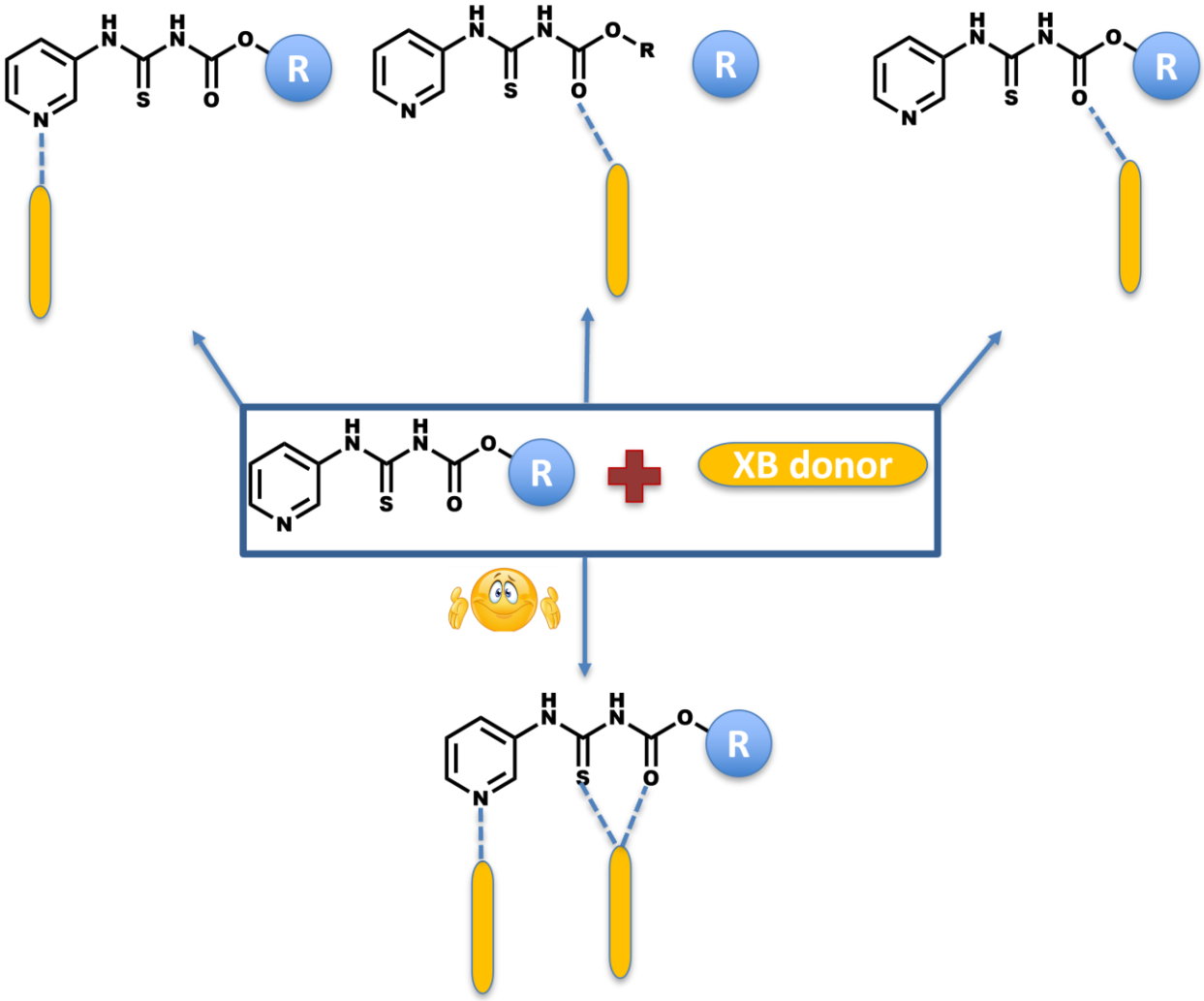

Scheme 4-3 Postulated primary intermolecular interactions in co-crystals of target molecules and halogen-bond donors.

4.2.Experimental

4.2.1. Reagents and General Methods

All reagents were used as received without any further purification. MEPs were calculated using density functional theory on molecules optimized in the gas phase using Spartan' 08 program with B3LYP/6-311++G** level of theory[40]. All the NMRs were recorded on a Bruker 400 MHz spectrophotometer. Single crystal X-ray diffraction (SCXRD) data were obtained using a Rigaku XtaLAB Synergy-S with a CuKα source. The melting points were collected using a TA instrument DSC Q20 differential scanning calorimeter. Targets were synthesized using modified versions of reported procedures[41, 42].

4.2.2. Synthesis of methyl-N-[(3-pyridinylamino) thioxomethyl carbamate[42] (A1)

Methyl chloroformate (0.78 mL, 10mmol) was added dropwise to a solution of ethyl acetate containing potassium thiocyanate (1.17 g, 12 mmol). The reaction mixture was heated at 75 °C for 3 hours. KCl was filtered off and 3-aminopyridine (0.94 g, 10 mmol) was added to filtrate. The reaction mixture was heated under reflux for a further 5 hours. The mixture was cooled to room temperature followed by vacuum filtration. After evaporating the solvent in vacuum, the product was obtained by washing the precipitate with 75% ethanol three times. The product was a white solid with a yield of 68 %, m.p: 172-175 °C. 1H NMR (400 MHz, Chloroform-d) δ 11.50 (s, 1H), 8.70 (d, J = 2.6 Hz, 1H),

8.51 (dd, J = 4.9, 1.5 Hz, 1H), 8.39 (s, 1H), 8.25 (ddd, J = 8.3, 2.8, 1.5 Hz, 1H), 7.36 (dd, J = 8.3, 4.8 Hz, 1H), 3.88 (s, 3H). 13C NMR (101 MHz, CDCl3) δ 178.57, 153.31, 147.68, 145.60, 134.52, 131.73, 123.29, 53.74.

4.2.3. Synthesis of ethyl-N-[(3-pyridinylamino) thioxomethyl] carbamate[41, 43] (A2)

Ethyl chloroformate (0.96 mL, 10mmol) and ethyl acetate were mixed in a round bottomed flask. To this solution, potassium thiocyanate (1.17 g, 12 mmol) and *N,N,N′,N′*-tetramethylethylenediamine (TMEDA) (0.02 mL, 0.1 mmol) were added and the reaction mixture was stirred at room temperature for 5 hours. 3-aminopyridine (0.94 g, 10 mmol) was then slowly added to the reaction mixture with constant stirring. The reaction mixture was stirred at room temperature for another 5 hours. The progress of the reaction was monitored using TLC. Upon completion, the solvent was evaporated under vacuum and the product was obtained by washing the precipitate with 10mL of 75% ethanol three times and 15 mL water three times. The product was a white solid with a yield of 75%, m.p: 164-165 °C. ^{1}H NMR (400 MHz, Chloroform-d) δ 11.56 (s, 1H), 8.71 (d, J = 2.6 Hz, 1H), 8.60 – 8.56 (m, 1H), 8.52 (dd, J = 4.8, 1.5 Hz, 1H), 8.26 (ddd, J = 8.4, 2.8, 1.6 Hz, 1H), 7.39 – 7.31 (m, 1H), 4.31 (q, J = 7.1 Hz, 2H), 1.37 (t, J = 7.1 Hz, 3H).^{13}C NMR (101 MHz, $CDCl_3$) δ 178.81, 152.98, 147.59, 145.60, 134.59, 131.72, 123.26, 63.31, 14.21.

4.2.4. Synthesis of isobutyl-*N*-[(3-pyridinylamino) thioxomethyl carbamate (A3)

Isobutyl chloroformate (1.30 mL, 10mmol) and ethyl acetate were mixed in a round bottomed flask. To this solution, potassium thiocyanate (1.17 g, 12 mmol) and TMEDA (0.02 mL, 0.1 mmol) were added, and the reaction mixture was stirred at room temperature for 5 hours. 3-aminopyridine (0.94 g, 10 mmol) was then slowly added to the reaction mixture with constant stirring. The reaction mixture was stirred at room temperature for another 5 hours. After evaporating the solvent in vacuum, the product was obtained by washing the precipitate with 75% ethanol and water. The product was a white solid with a yield of 71%. m.p: 123-125 °C. ^{1}H NMR (400 MHz, Chloroform-d) δ 11.56 (s, 1H), 8.71 (d, J = 2.6 Hz, 1H), 8.65 (s, 1H), 8.51 (d, J = 4.8 Hz, 1H), 8.26 (dt, J = 8.4, 2.0 Hz, 1H), 7.35 (dd, J = 8.3, 4.8 Hz, 1H), 4.03 (d, J = 6.5 Hz, 2H), 2.07 – 1.94 (m, J = 6.7 Hz, 1H), 0.98 (d, J = 6.6 Hz, 6H). ^{13}C NMR (101 MHz, Chloroform-d) δ 178.83, 153.09, 147.59, 145.59, 134.58, 131.71, 123.26, 73.06, 27.75, 18.85.5.

4.2.5. Crystallization Experiments

4.2.5.1. Synthesis of methyl-*N*-[(3-pyridinylamino) thioxomethyl] carbamate·1,3,5-trifluoro-2,4,6-triiodobenzene cocrystal (A1·D1)

Stoichiometric amounts of **A1** (2.5 mg) and **D1** (24 mg) were ground in a 1:4 molar ratio using solvent assisted grinding (SAG) and the resulting solids were analyzed using IR spectroscopy. The solid mixtures were dissolved in chloroform (3-4ml) and kept in small vials for slow evaporation at room temperature to get single crystals. Crystals suitable for

single-crystal X-ray diffraction were obtained after 5–6 days. The melting point of the co-crystal was 168-170 °C.

4.2.5.2. Synthesis of di-(ethyl-*N*-[(3-pyridinylamino) thioxomethyl] carbamate)·1,3,5-trifluoro-2,4,6-triiodobenzene cocrystal $(A2)_2$·D1

Stoichiometric amounts of **A2** (2.5 mg) and **D1** (23 mg) were ground in a 1:4 molar ratio using SAG and the resulting solids were analyzed using IR spectroscopy. The solid mixtures were dissolved in ethanol (3-4ml) and kept in small vials for slow evaporation at room temperature to get single crystals. Crystals suitable for single-crystal X-ray diffraction were obtained after 5–6 days. The melting point of the co-crystal was 152-154°C.

4.2.5.3. Synthesis of isobutyl-*N*-[(3-pyridinylamino) thioxomethyl] carbamate·1,3,5-trifluoro-2,4,6-triiodobenzene cocrystal (A3·D1)

Stoichiometric amounts of **A3** (2.5 mg) and **D1** (20 mg) were ground using SAG in a 1:4 molar ratio and the resulting solids were analyzed using IR spectroscopy. The solid mixtures were dissolved in ethanol (3-4ml) and kept in small vials for slow evaporation at room temperature to get single crystals. Crystals suitable for single-crystal X-ray diffraction were obtained after 3 weeks. The melting point of the co-crystal was 171-174°C.

4.2.5.4. Synthesis of di-(methyl-*N*-[(3-pyridinylamino) thioxomethyl] carbamate) 1,2,4,5-tetrafluoro-3,6-diiodobenzene chloroform solvate $(A1)_2$·D2

Stoichiometric amounts of **A1** (2.5 mg) and **D2** (8 mg) were ground in a 1:2 molar ratio using SAG and the resulting solids were analyzed using IR spectroscopy. The solid mixtures were dissolved in chloroform (3-4ml) and kept in small vials for slow evaporation at room temperature to get single crystals. Crystals suitable for single-crystal X-ray diffraction were obtained after 10 days. The melting point of the co-crystal was 158-160 °C.

4.2.5.5. Synthesis of ethyl-*N*-[(3-pyridinylamino) thioxomethyl] carbamate·1,2,4,5-tetrafluoro-3,6-diiodobenzene chloroform solvate (A2·D2)

Stoichiometric amounts of **A2** (2.5 mg) and **D2** (9 mg) were ground in a 1:2 molar ratio using SAG and the resulting solids were analyzed using IR spectroscopy. The solid mixtures were dissolved in chloroform (3-4ml) and kept in small vials for slow evaporation at room temperature to get single crystals. Crystals suitable for single-crystal X-ray diffraction were obtained after 1 week. The melting point of the co-crystal was 106-108 °C.

4.2.5.6. Synthesis of di-(isobutyl-*N*-[(3-pyridinylamino) thioxomethyl] carbamate) 1,2,4,5-tetrafluoro-3,6-diiodobenzene chloroform solvate $(A3)_2$·D2

Stoichiometric amounts of **A3** (2.5 mg) and **D2** (8 mg) were ground using SAG in a 1:2 molar ratio and the resulting solid was analyzed using IR spectroscopy. The solid mixture was dissolved in chloroform (3-4ml) and kept in small vials for slow evaporation at room

temperature to get single crystals. Crystals suitable for single-crystal X-ray diffraction were obtained after 1 week. The melting point of the co-crystal was 106-108 °C.

4.3.Results

Molecular electrostatic potentials were used for ranking the donor and acceptor ability of hydrogen-bond donors, halogen-bond donors, and acceptor sites by only considering the electrostatic component. The R-*N*-[(3-pyridinylamino) thioxo-methyl] carbamates targets contain acceptors such as carbonyl oxygen atom(C=O), pyridyl nitrogen atom (N_{pyr}), C=S, as well as a hydrogen-bond donor, N-H (Fig. 4-1a-c). The sulfur atom of the C=S group has two different regions of electron density as shown below. The two regions have significantly different potentials (≤23 kJ/mol) for **A1** and **A2**, while a difference of ≤10 kJ/mol is calculated for **A3**. The halogen-bond donors range from 159 to 169 kJ/mol (Fig. 4-1d-e). The target molecules have multiple donating (215 to 218 kJ/mol) and accepting sites (-92 to -198 kJ/mol) and acceptors can be ranked in the order N_{pyr} > C=S > C=O. The question then is where will binding occur if we introduce XB donors as co-formers for co-crystallization?

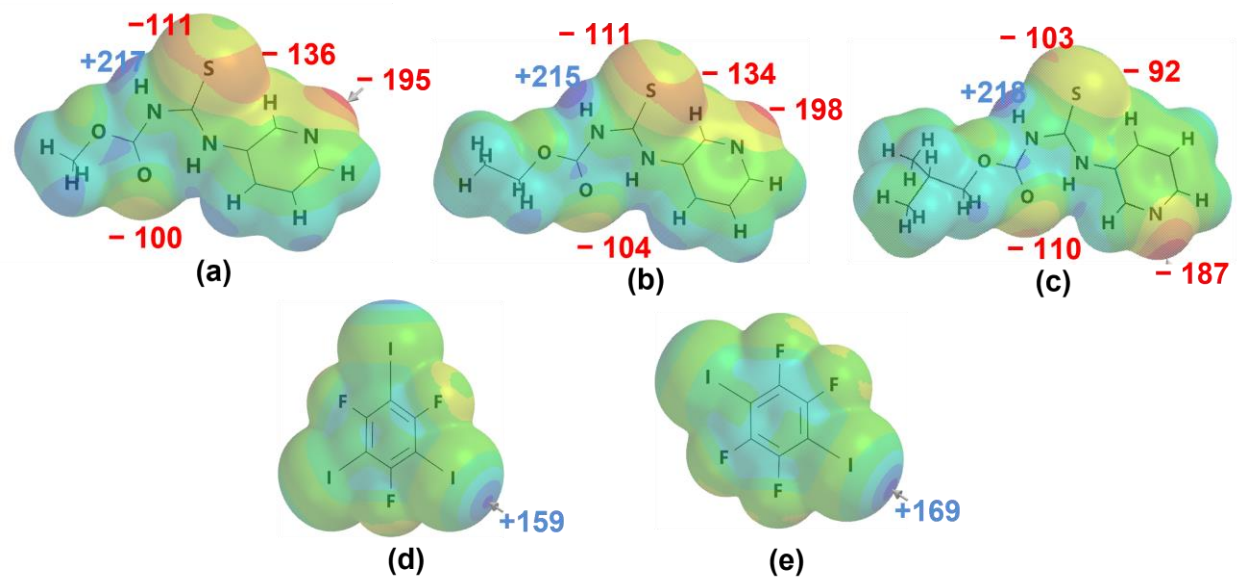

Figure 4-1 Molecular electrostatic potentials (kJ/mol) of the targets (a-c) **A1-A3** and (d-e) XB donors **D1-D2** respectively showing electron rich (red) and electron deficient (blue) regions.

We obtained crystals suitable for SCXRD analysis of **A1** and **A3**. The crystal structure of **A2** has previously been reported [43]. In the crystal structures of **A1**-**A3**, the primary intermolecular interactions were N–H···N_{pyr} complemented by an intramolecular N–H···O hydrogen bond. In addition, all three structures form C-H···S=C interactions (Fig. 4-2a-c). Overall, connectivity in the crystal structures of the parent molecules show the following preferred mode of interaction: (N-H···N_{pyr}) as primary interaction generating chain-like assembly and (C-H···S=C) dimer formation in all three targets. This matches with the expected MEP-based interaction hierarchy which assumes that the best donor preferentially binds to the best acceptor.

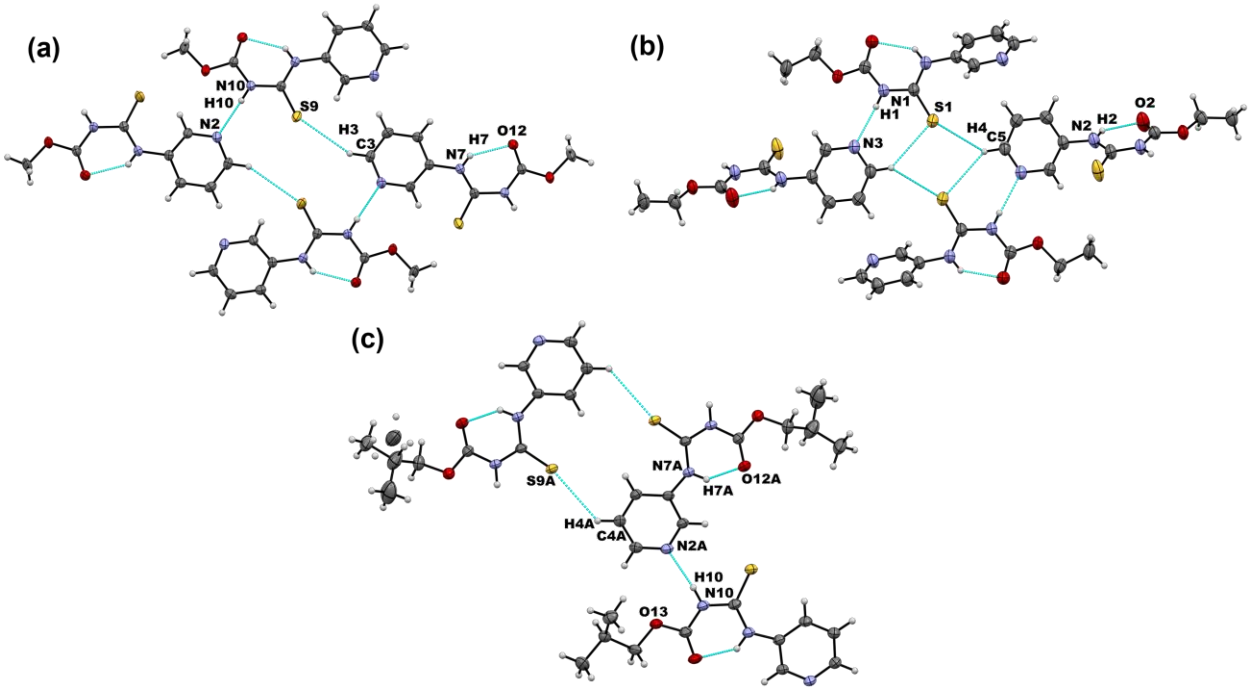

Figure 4-2 Primary non-covalent interactions (in blue) in the crystal structures of (a) **A1**·(b) **A2** and (c) **A3**.

Six co-crystals of each target compound with 1,3,5-trifluoro-2,4,6-triiodobenzene (**D1**) and 1,2,4,5-tetrafluoro-3,6-diiodobenzene (**D2**) were synthesized: **A1·D1**, $(\mathbf{A2})_2$**·D1**, **A3·D1**, $(\mathbf{A1})_2$**·D2**, **A2·D2** and $(\mathbf{A3})_2$**·D2**. In **A1·D1,** the hydrogen-bonded chains observed in parent molecules between the adjacent **A1** molecules via N–H···N_{pyr} interactions are retained. In addition, the **D1** donor acts as a crosslink between **A1** molecules through I···S=C and I···O=C halogen bonds (Fig. 4-3a). In $(\mathbf{A2})_2$**·D1**, the binding preference is through I···N_{pyr} halogen bonds, while the parent molecules form dimers through N-H···S=C and N-H···O=C interactions (Fig. 4-3b). It is worth noting that the N–H···N_{pyr} hydrogen-bond in **A2** is replaced by the new I···N_{pyr} halogen bond. Co-crystallization of **A3** and **D1** also yielded co-crystals via I···N_{pyr}, and unlike in $(\mathbf{A2})_2$**·D1** where I···N_{pyr} is the

only halogen-bond, a I···S=C halogen bond is also observed. In addition, parent molecules interact by forming (N-H···S=C) dimers. The remaining acceptor, (C=O) on **A3**, does not participate in any intermolecular bonds of note.

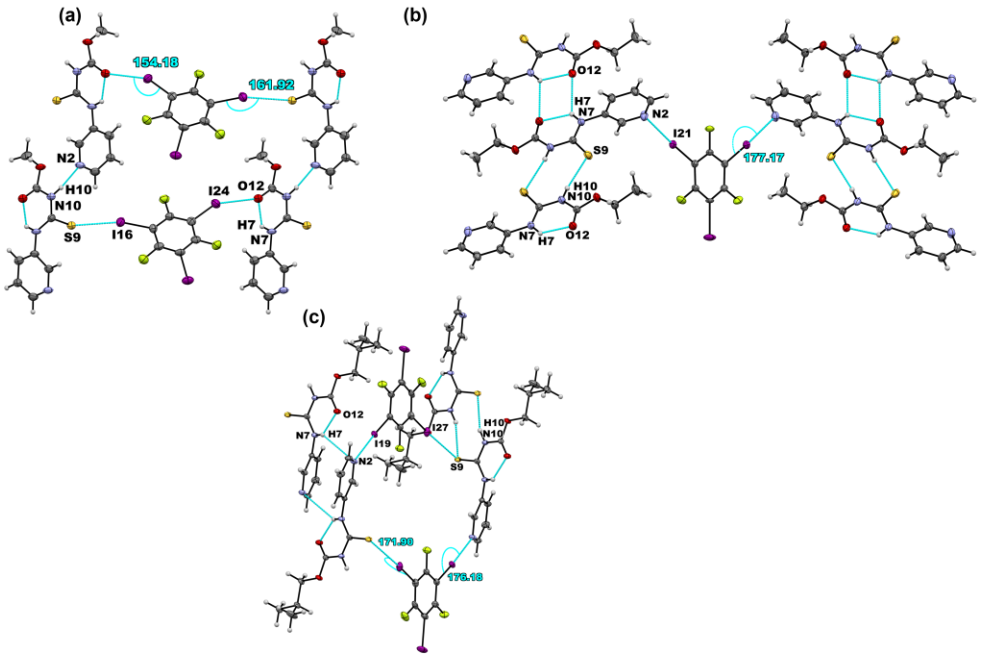

Figure 4-3 Primary non-covalent interactions in the crystal structures of (a) **A1·D1**, (b) **(A2)$_2$·D1** and (c) **A3·D1**.

The combination of **D2**, with the R-*N*-[(3-pyridinylamino) thioxomethyl] carbamates resulted in the formation of three co-crystals. Furthermore, **(A1)$_2$·D2** appeared as a solvate with a disordered chloroform in the asymmetric unit. Similar to **A1·D1**, a hydrogen-bonded chain is present between adjacent target molecules via N–H···N$_{pyr}$ interactions. In this co-crystal, the donor exclusively binds to the (C=S) acceptor providing a bridge between two target molecules through I···S=C (Fig. 4-4a). The same

primary synthons and assemblies are present in the structure of **A2·D2** as shown in (Fig. 4-4b). (**A3**)$_2$·**D2**, on the other hand, yielded halogen bonded co-crystals via I···N$_{pyr}$ while the parent molecules formed a dimer through N-H···S=C (Fig. 4-4c).

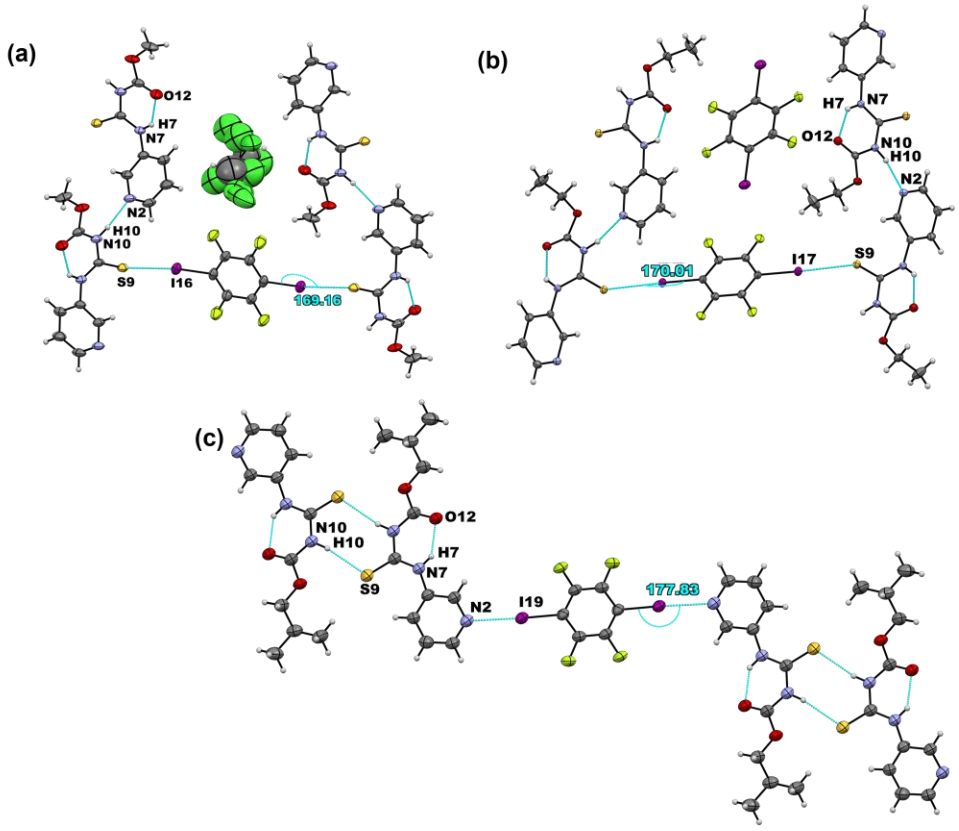

Figure 4-4 Primary non-covalent interactions (in blue) in the crystal structures of **(A1)**$_2$·**D2**, (b) **A2·D2** and (c) **(A3)**$_2$·**D2**.

4.4. Discussions

All three crystal structures of the target compounds showed identical hydrogen-bond motifs. A packing analysis was carried out to investigate the effect that aliphatic chains with varying lengths (R= methyl, ethyl, and isobutyl) may have on synthon robustness.

The crystal structures of **A1** and **A2** contain layers that stack on top of each other with no notable interlayer interactions. Furthermore, the alkyl groups (in green) point towards each other as seen in the packing units of **A1** and **A2** (Fig 4-5a. and b.). For **A3**, similar to the methyl and ethyl groups, the isobutyl groups point toward each other (Fig 4-5c). However, because there are two symmetry independent molecules present in the asymmetric unit, the tails can be differentiated (indicated by blue and green coloring in the figure). Also, because of the bulkier nature of the isobutyl group, the molecules aggregate into hydrophobic layers of the alkyl chain and pi-stacked layers of the aromatic rings. Packing index was calculated using PLATON [44] and was used to characterize total efficiency and compactness of the packing in the targets. The packing index was found to be 70.3 % for **A1**, and 66.4% for **A2** and **A3**. Overall, the packing was similar in all three target structures despite increasing the alkyl chain length, but it is noticeable that packing efficiency was slightly reduced in the structures of the compounds containing ethyl and isobutyl groups.

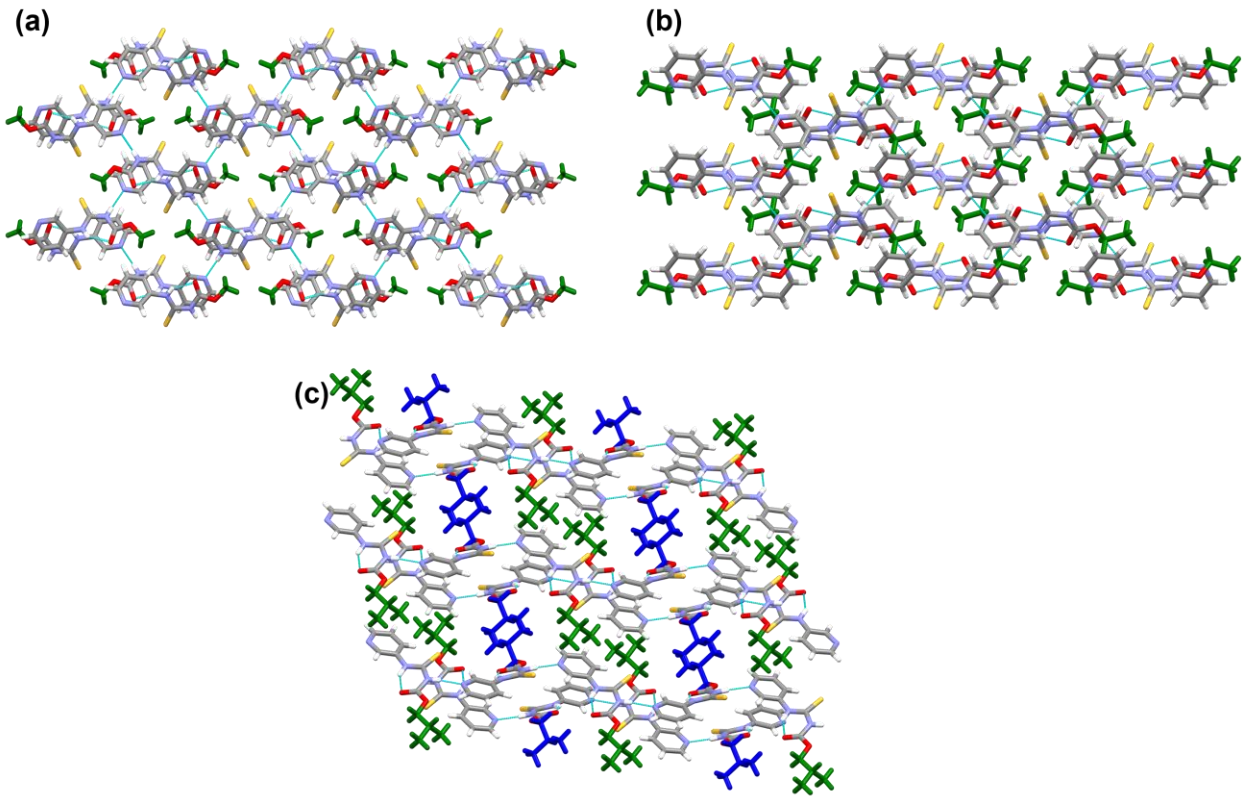

Figure 4-5 Crystal packing in target compounds (a-c) **A1-A3**

In **A1·D1** and **A3·D1**, the target molecules assemble into chains and **D1** provides a crosslink between adjacent chains (Fig. 4-6a, c). Unlike in **A1·D1** and **A3·D1**, in **(A2)$_2$·D1** the target molecules aggregate to form sheets connected by **D1** molecules (Fig.4-6b). Despite having different intermolecular interactions, the co-crystals adopt similar packing, (Fig. 4-6a-c).

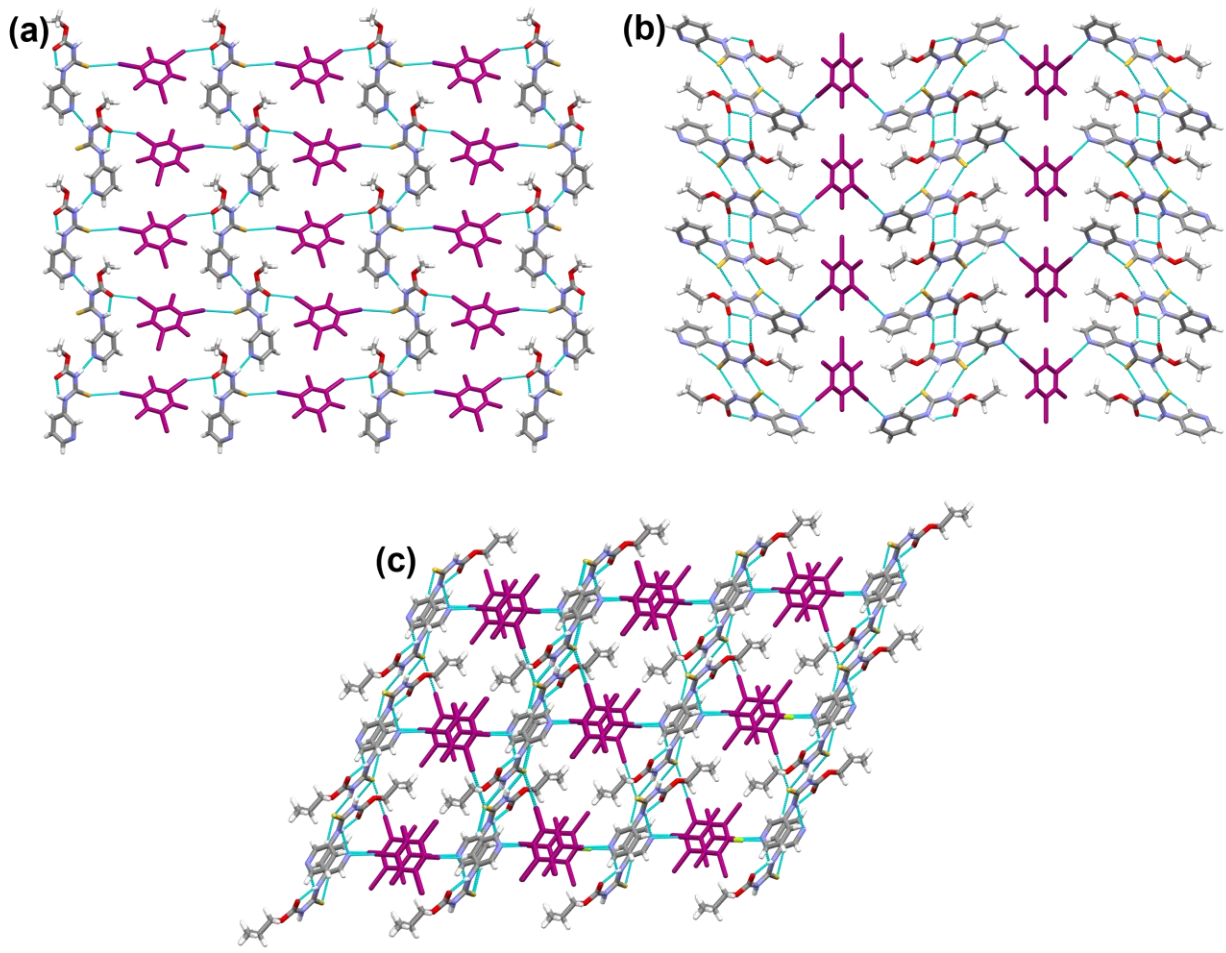

Figure 4-6 Crystal packing in (a) **A1·D1**, (b) **(A2)$_2$·D1** and (c) **A3·D1**.

The chloroform and **D2** molecules in the lattice of **(A1)$_2$·D2** and **A2·D2** respectively (Fig.4-7a, b), are primarily space filling, and do not seem to engage in any strong interactions with neighboring molecules. Despite **(A1)$_2$·D2** being a solvate and **A2·D2** being a pure co-crystal, both structures adopt the same packing. Furthermore, **(A1)$_2$·D2** and **A2·D2** exhibit similar packing behavior to **A1·D1** and **A3·D1**, where target molecules form chains interconnected by the co-formers through halogen bonds. **(A3)$_2$·D2** was different from

(A1)$_2$·D2 and **A2·D2** in that **(A3)$_2$·D2** formed I···Npyr halogen bonds with **D2**, while the latter both formed I···S=C halogen bonds. Although binding preference to S=C is observed in **(A1)$_2$·D2** and **A2·D2** it is still not obvious why the binding preference switches to I···Npyr in **(A3)$_2$·D2** (Fig. 4-7c)

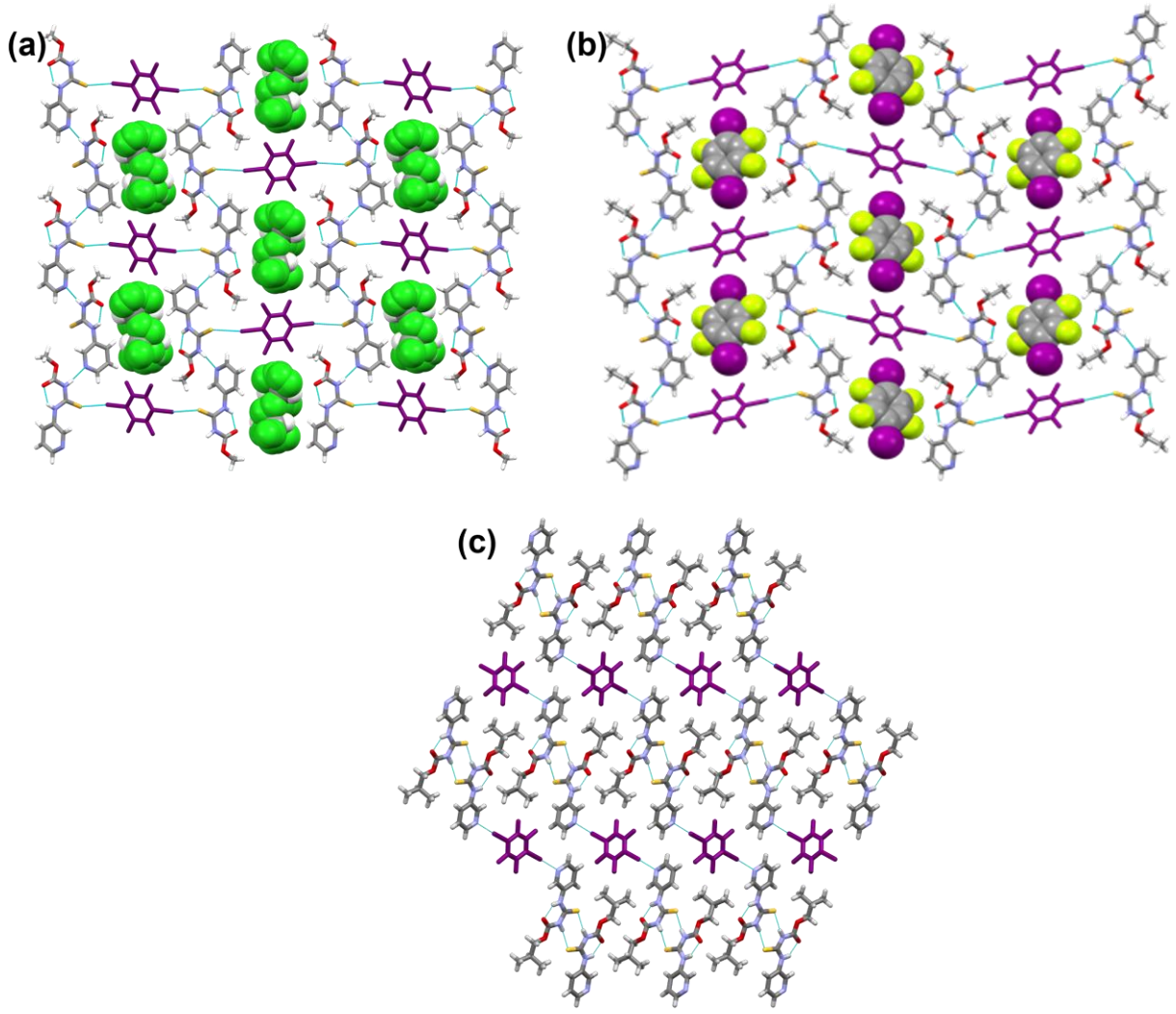

Figure 4-7 Crystal packing in (a) **(A1)$_2$·D2**, (b) **A2·D2** and (c) **(A3)$_2$·D2**.

All crystal structures obtained were compared to the outcome suggested by MEP calculations. In this study, the best donor and acceptor were predicted to be N-H and N_{pyr} of the target respectively. If the best donor binds to the best acceptor, N–H···N_{pyr} hydrogen bonds will be retained thus leaving the C=S and C=O acceptors to be free to form halogen bonds with the XB donors. However, if we assume that XB donors would preferentially bind to stronger acceptor sites, then acceptors can be ranked as N_{pyr} > C=S > C=O based purely on electrostatics.

Structural competition was not expected between acceptors N_{pyr} and C=S since their MEPs have about 60 kJ/mol difference. The I···N_{pyr} halogen bond was present in 3 of 6 structures, while the I···S=C halogen bond was found in 4 of 6 cases. In one of the structures, both interactions were present which suggests that MEPs underestimate the competing ability of the C=S moiety. Competition between C=S and C=O is expected to be moderate since the difference in MEP is ~30 kJ/mol. The I···S=C bond was observed in 4/6 structures while I···O=C is observed only once. The MEPs proved to be effective for predicting the outcome of the attempted co-crystallizations.

The % van der Waals reductions[45] were examined to get a semi-qualitative sense of the strengths of halogen-bond interactions observed. Analysis of the % vdW reductions in Table 1 reveals that the I···Npyr bond is stronger (16-20%; 176.2-177.8°) compared to

I···C=S bond (11-14%; 161.9-171.9°) and I···O=C bond (154°). The experimental % vdW reductions correlate with the MEP predictions. However, a careful analysis of the impact of molecular geometry could also be important for improved prediction accuracy given that the parent molecules are flexible.

Table 4-1 Halogen bond donor (X) to acceptor atom (A) XA distances and angles from crystal structures.

Co-crystal	**Halogen bond**	**Experimental XA distance**		**XA angle**
		(Å)	**% vdW reduction**	**(°)**
A1·D1	I···S=C	3.310(3)	12.2	161.9(3)
	I···O=C	3.168(9)	9.1	154.2(4)
$(A2)_2$·D1	I···Npyr	2.877(2)	18.2	177.2(8)
A3·D1	I···S=C	3.363(6)	10.9	171.9(7)
	I···Npyr	2.927(3)	16	176.2(1)
$(A1)_2$·D2	I···S=C	3.222(1)	14.6	169.2(1)
A2·D2	I···S=C	3.248(7)	13.8	170.0(6)
$(A3)_2$·D2	I···Npyr	2.802(6)	20.5	177.8(2)

The Cambridge Structural Database (CSD) ConQuest version 2021.1.0 [46] was used to provide a larger context through a search for the following intermolecular interactions: I···Npyr, I···S=C, and I···O=C. Appendix B shows a summary of the contact descriptors used for the CSD search. The search yielded 832 individual crystal structures containing I···Npyr halogen bond, 110 crystal structures containing I···S=C, and 30 structures containing I···O=C. Appendix B shows the histogram plots of frequency against bond length along with descriptive statistical data for each type of interaction. The histograms and descriptive statistical data were plotted using Mercury version

2021.1.0 [47]. Of the 832 CSD hits containing the I···Npyr halogen bond, the interaction had 1280 total bond lengths. According to the histogram for I···Npyr below, 50% of the bond lengths were in the mid-range (2.80-2.92 (Å)) with a mean of 2.92 Å, while 24.8% lie in the lower range (2.30-2.80 (Å)) and 25.2% in the upper range (3.00-3.52 (Å)). The CSD results show that I···Npyr bond is the most prevalent, and the bonds obtained in our crystal structures fit into the middle-range where majority of the reported structures appear.

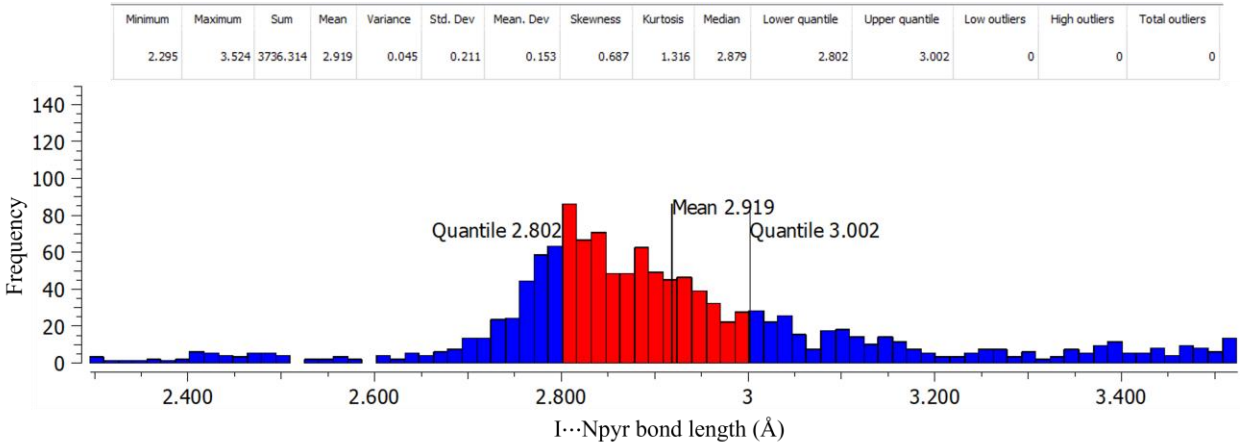

Figure 4-8 Histogram showing bond length against frequency for **I···N** halogen bond.

For the I···S=C bond, the 110 CSD hits gave a distribution of 184 various bond lengths. The histogram shows that 50% of those bond lengths were in the mid-range (3.18-3.65 (Å)) with a mean of 3.36 Å, while 25% lie in the lower range (2.49-3.18 (Å)) and 25% in the upper range (3.65-3.78 (Å)). Again, the I···S=C bond lengths obtained in our crystal structures are similar to reported data. For the I···O=C bond, we obtained only 30 hits (34 bond lengths) which is significantly lower hits than I···N_{pyr} and I···S=C. This suggests that

the interaction is not as prevalent as was the case in our crystal structures appearing only once. Overall, the histogram shows that the bond lengths are distributed with a mean of 3.18 Å and 50% of the bond lengths are in the range (3.07-3.28 (Å)). It is worth noting that despite fewer CSD hits for I···O=C bond, in our case it wasn't surprising that the interaction was less prevalent since O=C forms an intramolecular (N-H···O=C) hydrogen bond in all structures.

4.5. Conclusions

We have investigated a series of three parent molecules, as well as five pure co-crystals and one co-crystal solvate from R-N-[(3-pyridinylamino) thioxomethyl] carbamates with fluoroiodobenzene co-formers. Analysis of the parent molecules (**A1-A3**) shows that increasing the alkyl chain length does not significantly impact the overall supramolecular aggregating of the molecular building blocks. Overall, N–H···Npyr hydrogen bond is the dominant intermolecular interaction as it appears in all three structures, producing dimeric units in each case.

Co-crystallization experiments show that the N-H···Npyr interaction was present in 3/6 co-crystals with additional halogen-bond interactions. In cases where parent molecules did not form N–H···Npyr chains, hydrogen-bonded dimers through N-H···S=C and N-H···O=C stabilized the architectures. Co-crystals with **D1** displayed varying halogen

bonding patterns i.e. (I···S=C, I···O=C), (I···Npyr) and (I···Npyr, I···C=S) for **A1·D1**, **(A2)$_2$·D1**, and **A3·D1**, respectively. Co-crystallization with **D2** in **(A1)$_2$·D2** and **A2·D2** displayed binding preference to C=S which is the second-best acceptor forming I···C=S halogen bond while structure **(A3)$_2$·D2** shows binding preference to the best acceptor Npyr. I···Npyr was found in 3/6 structures, I···C=S in 4/6 structures and I···O=C only in one case. It is worth noting that I···C=S halogen bond coexisted twice with I···Npyr and I···O=C separately. CSD contact search revealed that the I···Npyr is most prevalent followed by I···S=C, then I···O=C and this trend is similar to what we observed for our structures.

Calculated molecular electrostatic potentials and % van der Waals radii suggest the formation of halogen bonding to the acceptors in the order Npyr > C=S > C=O. Overall, the co-crystals exhibited I···C=S halogen bond interactions even when MEP calculations favored the N_{pyr} acceptor by ~60 kJ/mol, suggesting that it is crucial to consider additional factors that affect co-crystallization outcomes such as geometry. Despite not establishing a consistent synthon prediction trend for our system, we have established that halogen bond donors are competitive for binding sites even in the presence of strong hydrogen-bond donors but synthon preference in the presence of multiple acceptors is not as straightforward as is the case for prediction in simpler systems.

4.6.References

1. Ardila-Fierro, K. J.; André, V.; Tan, D.; Duarte, M. T.; Lancaster, R. W.; Karamertzanis, P. G.; Friščić, T., Molecular Recognition of Steroid Hormones in the Solid State: Stark Differences in Cocrystallization of β-Estradiol and Estrone. *Crystal Growth & Design* **2015,** *15* (3), 1492-1501.
2. Pramanik, T.; Sarkar, S.; Guru Row, T. N., Halogen Bonded Network Modulating the Mechanical Property Elastic and Plastic Bending in Nonconventional Molecular Solid Solutions. *Crystal Growth & Design* **2022,** *22* (1), 48-53.
3. Reddy, C. M.; Padmanabhan, K. A.; Desiraju, G. R., Structure−Property Correlations in Bending and Brittle Organic Crystals. *Crystal Growth & Design* **2006,** *6* (12), 2720-2731.
4. Saha, S.; Desiraju, G. R., σ-Hole and π-Hole Synthon Mimicry in Third-Generation Crystal Engineering: Design of Elastic Crystals. *Chemistry – A European Journal* **2017,** *23* (20), 4936-4943.
5. Yadava, K.; Qin, X.; Liu, X.; Vittal, J. J., Straight, bendable and bent organic crystals. *Chemical Communications* **2019,** *55* (98), 14749-14752.
6. Ghosh, S.; Mishra, M. K.; Kadambi, S. B.; Ramamurty, U.; Desiraju, G. R., Designing Elastic Organic Crystals: Highly Flexible Polyhalogenated N-Benzylideneanilines. *Angewandte Chemie International Edition* **2015,** *54* (9), 2674-2678.
7. Juneja, N.; Shapiro, N. M.; Unruh, D. K.; Bosch, E.; Groeneman, R. H.; Hutchins, K. M., Controlling Thermal Expansion in Supramolecular Halogen-Bonded Mixed Cocrystals through Synthetic Feed and Dynamic Motion. *Angewandte Chemie International Edition* **2022,** *61* (26).
8. Liu, Y.; Ward, M. D., Molecular Capsules in Modular Frameworks. *Crystal Growth & Design* **2009,** *9* (9), 3859-3861.
9. Aakeröy, C. B.; Beatty, A. M.; Helfrich, B. A.; Nieuwenhuyzen, M., Do Polymorphic Compounds Make Good Cocrystallizing Agents? A Structural Case Study that Demonstrates the Importance of Synthon Flexibility. *Crystal Growth & Design* **2003,** *3* (2), 159-165.
10. Sreekanth, B. R.; Vishweshwar, P.; Vyas, K., Supramolecular synthon polymorphism in 2 : 1 co-crystal of 4-hydroxybenzoic acid and 2,3,5,6-tetramethylpyrazine. *Chemical Communications* **2007,** (23), 2375-2377.
11. Mukherjee, A.; Desiraju, G. R., Synthon polymorphism and pseudopolymorphism in co-crystals. The 4,4′-bipyridine–4-hydroxybenzoic acid structural landscape. *Chemical Communications* **2011,** *47* (14), 4090-4092.
12. Burrows, J. A., Pauling, Linus. The nature of the chemical bond and the structure of molecules aid crystals. Ithaca: The Cornell University Press, 1939. . *Science Education* **1941,** *25* (2), 120-120.

13. Aakeröy, C. B.; Spartz, C. L.; Dembowski, S.; Dwyre, S.; Desper, J., A systematic structural study of halogen bonding versus hydrogen bonding within competitive supramolecular systems. *IUCrJ* **2015,** *2* (Pt 5), 498-510.
14. Galek, P. T. A.; Allen, F. H.; Fábián, L.; Feeder, N., Knowledge-based H-bond prediction to aid experimental polymorph screening. *CrystEngComm* **2009,** *11* (12), 2634-2639.
15. Hunter, C. A., Quantifying Intermolecular Interactions: Guidelines for the Molecular Recognition Toolbox. *Angewandte Chemie International Edition* **2004,** *43* (40), 5310-5324.
16. Musumeci, D.; Hunter, C. A.; Prohens, R.; Scuderi, S.; McCabe, J. F., Virtual cocrystal screening. *Chemical Science* **2011,** *2* (5), 883-890.
17. DeHaven, B. A.; Chen, A. L.; Shimizu, E. A.; Salpage, S. R.; Smith, M. D.; Shimizu, L. S., Interplay between Hydrogen and Halogen Bonding in Cocrystals of Dipyridinylmethyl Oxalamides and Tetrafluorodiiodobenzenes. *Crystal Growth & Design* **2019,** *19* (10), 5776-5783.
18. Martí-Rujas, J.; Colombo, L.; Lü, J.; Dey, A.; Terraneo, G.; Metrangolo, P.; Pilati, T.; Resnati, G., Hydrogen and halogen bonding drive the orthogonal self-assembly of an organic framework possessing 2D channels. *Chemical Communications* **2012,** *48* (66), 8207-8209.
19. Aakeröy, C. B.; Wijethunga, T. K.; Haj, M. A.; Desper, J.; Moore, C., The structural landscape of heteroaryl-2-imidazoles: competing halogen- and hydrogen-bond interactions. *CrystEngComm* **2014,** *16* (31), 7218-7225.
20. Gunawardana, C. A.; Desper, J.; Sinha, A. S.; Đaković, M.; Aakeröy, C. B., Competition and selectivity in supramolecular synthesis: structural landscape around 1-(pyridylmethyl)-2,2′-biimidazoles. *Faraday Discussions* **2017,** *203* (0), 371-388.
21. Abeysekera, A. M.; Averkiev, B. B.; Sinha, A. S.; Le Magueres, P.; Aakeröy, C. B., Establishing Halogen-Bond Preferences in Molecules with Multiple Acceptor Sites. *ChemPlusChem* **2021,** *86* (8), 1049-1057.
22. De Silva, V.; Averkiev, B. B.; Sinha, A. S.; Aakeröy, C. B., The Balance between Hydrogen Bonds, Halogen Bonds, and Chalcogen Bonds in the Crystal Structures of a Series of 1,3,4-Chalcogenadiazoles. *Molecules* **2021,** *26* (14), 4125.
23. Stanley, C. W.; Thornton, J. S.; Katague, D. B., Gas-chromatographic method for residues of Baygon and metabolites in plant tissues. *Journal of Agricultural and Food Chemistry* **1972,** *20* (6), 1265-1269.
24. Teixeira, M. A.; Barrault, L.; Rodríguez, O.; Carvalho, C. C.; Rodrigues, A. E., Perfumery Radar 2.0: A Step toward Fragrance Design and Classification. *Industrial & Engineering Chemistry Research* **2014,** *53* (21), 8890-8912.
25. Axthammer, Q. J.; Krumm, B.; Klapötke, T. M., Synthesis of Energetic Nitrocarbamates from Polynitro Alcohols and Their Potential as High Energetic Oxidizers. *The Journal of Organic Chemistry* **2015,** *80* (12), 6329-6335.

26. Popović, M.; Nierkens, S.; Pieters, R.; Uetrecht, J., Investigating the Role of 2-Phenylpropenal in Felbamate-Induced Idiosyncratic Drug Reactions. *Chemical Research in Toxicology* **2004,** *17* (12), 1568-1576.
27. Parker, R. J.; Hartman, N. R.; Roecklein, B. A.; Mortko, H.; Kupferberg, H. J.; Stables, J.; Strong, J. M., Stability and Comparative Metabolism of Selected Felbamate Metabolites and Postulated Fluorofelbamate Metabolites by Postmitochondrial Suspensions. *Chemical Research in Toxicology* **2005,** *18* (12), 1842-1848.
28. Tegeler, T.; El Rassi, Z., On-Column Trace Enrichment by Sequential Frontal and Elution Electrochromatography. 1. Application to Carbamate Insecticides. *Analytical Chemistry* **2001,** *73* (14), 3365-3372.
29. Aly, O. M.; El-Dib, M. A., Studies of The Persistence of Some Carbamate Insecticides in The Aquatic Environment. In *Fate of Organic Pesticides in the Aquatic Environment*, AMERICAN CHEMICAL SOCIETY: 1972; Vol. 111, pp 210-243.
30. Shamim, M.; Meléndez, J.; Sappington, K.; Ruhman, M., Conducting Ecological Risk Assessments of Urban Pesticide Uses. In *Describing the Behavior and Effects of Pesticides in Urban and Agricultural Settings*, American Chemical Society: 2014; Vol. 1168, pp 207-274.
31. Zhang, J. J.; Yang, H., Advance in Methodology and Strategies To Unveil Metabolic Mechanisms of Pesticide Residues in Food Crops. *Journal of Agricultural and Food Chemistry* **2021,** *69* (9), 2658-2667.
32. Ghosh, A. K.; Brindisi, M., Organic Carbamates in Drug Design and Medicinal Chemistry. *Journal of Medicinal Chemistry* **2015,** *58* (7), 2895-2940.
33. Matošević, A.; Bosak, A., Carbamate group as structural motif in drugs: a review of carbamate derivatives used as therapeutic agents. *Archives of Industrial Hygiene and Toxicology* **2020,** *71* (4), 285-299.
34. Bennion, J. C.; Matzger, A. J., Development and Evolution of Energetic Cocrystals. *Accounts of Chemical Research* **2021,** *54* (7), 1699-1710.
35. Axthammer, Q. J.; Klapötke, T. M.; Krumm, B.; Reith, T., Energetic Sila-Nitrocarbamates: Silicon Analogues of Neo-Pentane Derivatives. *Inorganic Chemistry* **2016,** *55* (9), 4683-4692.
36. Klapötke, T. M.; Krumm, B.; Unger, C. C., Energetic Metal and Nitrogen-Rich Salts of the Pentaerythritol Tetranitrate Analogue Pentaerythritol Tetranitrocarbamate. *Inorganic Chemistry* **2019,** *58* (4), 2881-2887.
37. Aitipamula, S.; Banerjee, R.; Bansal, A. K.; Biradha, K.; Cheney, M. L.; Choudhury, A. R.; Desiraju, G. R.; Dikundwar, A. G.; Dubey, R.; Duggirala, N.; Ghogale, P. P.; Ghosh, S.; Goswami, P. K.; Goud, N. R.; Jetti, R. R. K. R.; Karpinski, P.; Kaushik, P.; Kumar, D.; Kumar, V.; Moulton, B.; Mukherjee, A.; Mukherjee, G.; Myerson, A. S.; Puri, V.; Ramanan, A.; Rajamannar, T.; Reddy, C. M.; Rodriguez-Hornedo, N.; Rogers, R. D.; Row, T. N. G.; Sanphui, P.; Shan, N.; Shete, G.; Singh, A.; Sun, C. C.; Swift, J. A.; Thaimattam, R.; Thakur, T. S.; Kumar Thaper, R.; Thomas, S. P.;

Tothadi, S.; Vangala, V. R.; Variankaval, N.; Vishweshwar, P.; Weyna, D. R.; Zaworotko, M. J., Polymorphs, Salts, and Cocrystals: What's in a Name? *Crystal Growth & Design* **2012,** *12* (5), 2147-2152.
38. Aakeröy, C. B.; Fasulo, M. E.; Desper, J., Cocrystal or Salt: Does It Really Matter? *Molecular Pharmaceutics* **2007,** *4* (3), 317-322.
39. Desiraju, G. R., Crystal Engineering: From Molecule to Crystal. *Journal of the American Chemical Society* **2013,** *135* (27), 9952-9967.
40. Wavefunction, I., Irvine, CA 92612, USA, https://www.wavefun.com/products/spartan.html, accessed March, 2022.
41. Wei, T. B.; Lin, Q.; Zhang, Y. M.; Wang, H., Efficient and Novel Synthesis of N-Aryl-N′-ethoxycarbonylthiourea and Arene-bis-ethoxycarbonylthiourea Derivatives Catalyzed by TMEDA. *Synthetic Communications* **2004,** *34* (12), 2205-2213.
42. Ren, Y.-H.; Song, J.-R.; Xu, K.-Z.; Ma, H.-X.; Huang, J.; Fu, D.-W.; Hu, H.-M., Preparation, Crystal Structure and Theoretical Calculation of N-(Pyrimidin-2-yl)-N′-methoxycarbonyl-thiourea. *Chinese Journal of Chemistry* **2007,** *25* (4), 510-514.
43. Zhang, Y.-M. Y., Li-Zi; Lin, Qi; Wei, Tai-Bao; Wang, Da-Qi, Synthesis and the crystal structure of N-ethoxycarbonyl-N'-(3-pyridyl)thiourea. *Youji Huaxue* **2006,** *26* (1), 134-138.
44. Spek, A., Structure validation in chemical crystallography. *Acta Crystallographica Section D* **2009,** *65* (2), 148-155.
45. Bondi, A., van der Waals Volumes and Radii. *The Journal of Physical Chemistry* **1964,** *68* (3), 441-451.
46. Groom, C. R.; Bruno, I. J.; Lightfoot, M. P.; Ward, S. C., The Cambridge Structural Database. *Acta Crystallographica Section B* **2016,** *72* (2), 171-179.
47. Macrae, C. F.; Sovago, I.; Cottrell, S. J.; Galek, P. T. A.; McCabe, P.; Pidcock, E.; Platings, M.; Shields, G. P.; Stevens, J. S.; Towler, M.; Wood, P. A., Mercury 4.0: from visualization to analysis, design and prediction. *Journal of Applied Crystallography* **2020,** *53* (1), 226-235.

Chapter 5 - Modulating thermal expansion by fine-tuning the molecular dimensions and number of functional groups in alkyl carbamate molecules

5.1.Introduction

Facilitating the design of functional solid-state materials with predictable and desirable structure-property relationships is essential for the development of new technologies and this also lies at the very heart of crystal engineering. Manipulating intermolecular interactions has been used to establish effective structure-property-function correlations, and a deeper understanding of noncovalent interactions is useful in the interpretation of the structure directing role of such forces.[1] For example, the control of noncovalent interactions has facilitated the design of materials with self-healing capacity[2-4] and stimuli-responsiveness.[5-7]

Temperature (T) is one of the most common physical external stimuli, employed as a trigger to initiate responses of thermosensitive materials. It is well-known that most materials expand as temperature increases, showing positive thermal expansion (PTE). However, some materials show lattice *contraction* during heating *i.e.*, negative thermal expansion[8-10] (NTE) or zero thermal expansion[11-13] (ZTE), in which materials neither expand nor contract over a specific temperature range. Thermal expansion ca also be classified as colossal TE which describes positive TE of materials with TE coefficient

greater than 100 MK^{-1}.[14] Scientists have come up with several reasons for TE[15-17], and one of the many reasons for thermal expansion is believed to be attributed to the types of interactions present in the materials. In general, it has been found that stronger interactions are less affected by temperature change, while weaker interactions cause larger thermal expansion with increasing temperature.[18] Several inorganic compounds have been reported to exhibit such anomalous expansion behavior.[14, 19-23] However, the organic counterparts have not been studied as much in this regard, and it is important to understand their TE properties since organic molecules can be used in materials design as well.

Crystal engineering has been utilized to fine tune the thermal expansion properties of materials; for instance, Saha et al.[24-27] have studied the interaction dependent thermal expansion in hydrogen-bonded solid forms. Hutchins and co-workers[28-30] have also explored fine-tuning co-crystals to control thermal expansion by changing the molecular motion in the crystals. Although crystal engineering has been employed in several systems to control thermal expansion behavior of solid-state materials, the systematic designing of materials exhibiting such properties is still a challenge.

The systems studied here for thermal expansion consist of five single component systems **DC4-DC8** (Scheme 5-1). Our target molecules contain H-bond donor and acceptor

functional groups and so we anticipate that H-bonding will bind the lattice together. Additionally, fine-tuning the number of functional groups allows for multiple molecular dimensions in our targets. It has been previously reported that a one-dimensional hydrogen bonded dimorphic pair demonstrates an interaction strength–thermal expansion relationship.[31] Altogether, it was observed that smaller expansions occurred in directions along which molecules were bound via stronger interactions. Owing to this we will examine a system with different hydrogen bond dimensionality for thermal expansion capability. A series of detailed structural determinations at 20-K intervals will enable us to visualize the process at the molecular level.

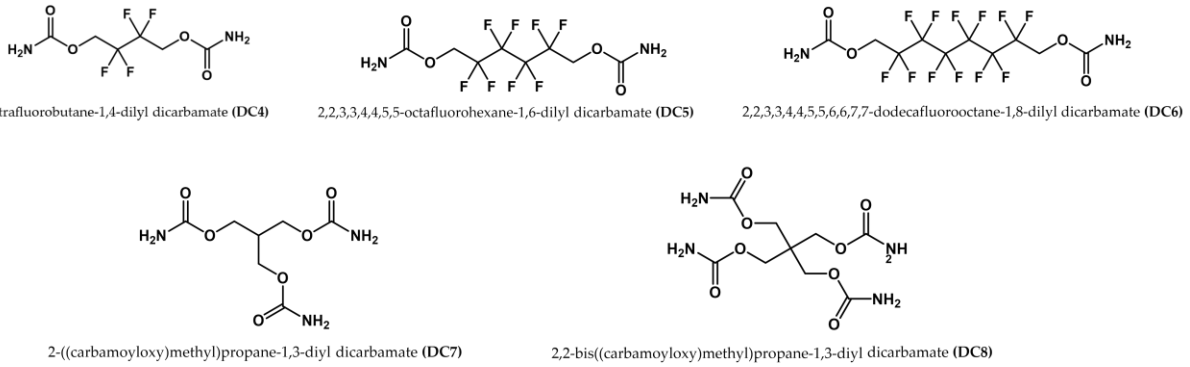

Scheme 5-1 Molecular structures of the carbamate targets used in this study (DC4-DC8)

The study is performed in order to answer the following questions,

1. What is the hydrogen bonding pattern in these five carbamate-based targets?
2. What is the relationship between intermolecular interactions and molecular packing with thermal expansion (TE)?

3. Can we systematically establish the influence of varying molecular dimensions on thermal expansion behavior of solid-state materials?

5.2.Experimental

5.2.1. Reagents and Methodology

All the precursors, reagents, solvents were purchased from commercial sources and used without further purification. ^{1}H NMR spectra was recorded on a Bruker 400 MHz spectrophotometer. The melting points were collected using a TA instrument DSC Q20 differential scanning calorimeter.

5.2.1.1. Variable temperature X-ray diffraction experiments

To investigate the effects of changing the chain length, number of functional groups, and crystal packing on the TE properties of our targets variable temperature X-ray diffraction experiments were conducted on a Rigaku XtaLAB Synergy-S with a CuKα source. Full data sets for each target molecule were collected over the temperature range of 250 to 150 K at 20 K increments to give six data points (250, 230, 210, 190, 170, 150 K). Changes in the unit cell parameters were observed for each target over the temperature range.

5.2.1.2. Energy framework calculations

CrystalExplorer 21[32] was employed to calculate and visualize intermolecular interaction energies based on the B3LYP/6-311G(d,p) level of theory and using crystal geometries

from experimental structures of the targets. The interaction energies of each molecule with all molecules having any atom within 3.8 Å were calculated. The tube size in the energy frameworks of all targets was set to 50, and the tube thickness corresponds to the strength of the interaction. The cut-off energy value was set to 5 kJ/mol. The energy components calculated within this method are electrostatic, polarization, dispersion, and exchange-repulsion: $E_{tot} = k_{ele}E_{ele} + k_{pol}E_{pol} + k_{dis}E_{dis} + k_{rep}E_{rep}$, in which k is scale factors obtained from benchmarked sets of compounds.

5.2.2. Synthesis of 2,2,3,3-tetrafluorobutane-1,4-dilyl dicarbamate (DC4)

In 20mL of acetonitrile, 2,2,3,3-tetrafluorobutane-1,4-diol (0.50 g, 3.09 mmol) was suspended, and cooled in an ice bath. Chlorosulfonyl isocyanate (CSI) (0.88 g, 6.17 mmol) was added very slowly at 0 °C to the suspension. The alcohol was dissolved during the addition of CSI, and a precipitate was formed. The ice bath was removed, and the mixture was stirred for 1 hour at room temperature. After 1 hour, the reaction mixture was cooled again in an ice bath, and 10 mL of water was added slowly. Acetonitrile was removed by rotavap and the precipitate formed was filtered and washed thoroughly with cold water and dried to obtain pure product as white solid. The solid was recrystallized in chloroform to give crystals suitable for SCXRD. Yield 0.73g (95 %). Mp 173-176 °C. ^{1}H NMR (600 MHz, DMSO-d6) δ 7.08 (s, 3H), 6.85 (s, 3H), 4.55 (t, J = 15.2 Hz, 6H), 3.17 (d, J = 3.5 Hz, 1H), 2.09 (d, J = 5.6 Hz, 5H), 0.99 (s, 1H).

5.2.3. Synthesis of 2,2,3,3,4,4,5,5-octafluorohexane-1,6-dilyl dicarbamate (DC5)

In 20mL of acetonitrile, 2,2,3,3,4,4,5,5-octafluorohexane-1,6-diol (0.50 g, 1.91 mmol) was suspended, and it cooled in an ice bath. Chlorosulfonyl isocyanate (CSI) (0.60 g, 4.2 mmol) was added very slowly at 0 °C to the suspension. The alcohol was dissolved during the addition of CSI, and a precipitate was formed. The ice bath was removed, and the mixture was stirred for 1 hour at room temperature. After 1 hour, the reaction mixture was cooled again in an ice bath and 10 mL of water was added slowly. Acetonitrile was removed by rotavap and the precipitate formed was filtered and washed thoroughly with cold water and dried to obtain pure product as white solid. The solid was recrystallized in acetonitrile to give crystals suitable for SCXRD. Yield 0.40 g (59 %). Mp 146-149 °C. ^{1}H NMR (600 MHz, DMSO-d6) δ 7.13 (s, 1H), 6.91 (s, 1H), 4.67 (t, J = 14.7 Hz, 3H), 2.09 (s, 18H).

5.2.4. Synthesis of 2,2,3,3,4,4,5,5,6,6,7,7-dodecafluorooctane-1,8-dilyl dicarbamate (DC6)

In 20mL of acetonitrile, 2,2,3,3,4,4,5,5,6,6,6,7,7-dodecafluorooctane-1,8-diol (0.50 g, 1.38 mmol) was suspended, and it cooled in an ice bath. Chlorosulfonyl isocyanate (CSI) (0.43 g, 3.04 mmol) was added very slowly at 0 °C to the suspension. The alcohol was dissolved during the addition of CSI, and a precipitate was formed. The ice bath was removed, and the mixture was stirred for 1 hour at room temperature. After 1 hour, the reaction mixture was cooled again in an ice bath and 10 mL of water was added slowly. Acetonitrile was

removed by rotavap and the precipitate formed was filtered and washed thoroughly with cold water and dried to obtain pure product as white solid. The solid was recrystallized in methanol to give crystals suitable for SCXRD. Yield 0.21 g (34 %). Mp 144-146 °C. ^{1}H NMR (600 MHz, DMSO-d6) δ 2.71 (s, 1H), 2.36 (s, 1H), 0.57 (s, 1H), -0.14 (t, J = 13.6 Hz, 6H).

5.2.5. Synthesis of 2-((carbamoyloxy)methyl)propane-1,3-diyl dicarbamate (DC7)

In 20mL of acetonitrile, 2-(hydroxymethyl)-1,3-propanediol (0.50 g, 4.7 mmol) was suspended and it cooled in an ice bath. Chlorosulfonyl isocyanate (CSI) (2.20 g, 15.5 mmol) was added very slowly at 0 °C to the suspension. During the addition, the alcohol was dissolved and at the end of the addition of CSI, a precipitate was observed. Then the ice bath was removed, and the mixture was stirred for 1.5 hours at room temperature. After 1.5 hours, the reaction mixture was cooled by placing an ice bath and 10 mL of water was added with caution. Acetonitrile was removed by rotavap and the precipitate filtered and washed thoroughly with cold water and dried to obtain pure product as white color solid. The solid was recrystallized in methanol to give crystals suitable for SCXRD. Yield 0.98 g (89 %). Mp 164-168 °C. ^{1}H NMR (600 MHz, DMSO-d6) δ 6.71 (s, 1H), 6.52 (s, 1H), 4.88 (tt, J = 6.1, 4.0 Hz, 1H), 4.07 (dd, J = 11.8, 3.9 Hz, 2H), 4.00 (dd, J = 11.8, 6.1 Hz, 2H), 2.09 (d, J = 5.4 Hz, 2H).

5.2.6. Synthesis of 2,2-bis((carbamoyloxy)methyl)propane-1,3-diyl dicarbamate (DC8)

In 20mL of acetonitrile, pentaerythritol (0.50 g, 3.7 mmol) was suspended and it cooled in an ice bath. Chlorosulfonyl isocyanate (CSI) (2.55 g, 18 mmol) was added very slowly at 0 °C to the suspension. The alcohol was dissolved during the addition of CSI, and a precipitate was formed. The ice bath was removed, and mixture was stirred for 1 hour at room temperature. After 1 hour, the reaction mixture was cooled by placing an ice bath and 10 mL of water was added slowly. Acetonitrile was removed by rotavap and the precipitate formed was filtered and washed thoroughly with cold water and dried to obtain pure product as white color solid. The solid was recrystallized in a solvent mixture of acetonitrile and water to give crystals suitable for SCXRD. Yield 1.03 g (90 %). Mp 256-261°C. ^{1}H NMR (600 MHz, DMSO-d6) δ 6.85 (s, 2H), 6.68 (s, 2H), 4.41 (s, 4H), 2.09 (d, J = 5.4 Hz, 1H).

5.3. Theory: Thermal expansion

Most materials are known to expand upon heating due to anharmonic thermal vibration of atoms.[33] Organic crystalline materials contain three crystallographic axes (a, b, c) and so the response of such materials to temperature occurs in all three directions.[34] For example, if the length of a crystal along a particular direction is L_i (initial length) at T_i (initial temperature in K) and L_f (final length) at T_f (final temperature in K), then the linear thermal expansion coefficient can be calculated as shown in equation 5.3.1[35],

$$\alpha_L = \frac{1}{L}\left(\frac{\delta L}{\delta T}\right) \qquad (5.3.1)$$

Similarly, if the volume is V_i (initial volume) at T_i (initial temperature in K) and V_f (final volume) at T_f (final temperature in K), then the volumetric thermal expansion coefficient can be calculated as shown in equation 5.3.2,

$$\alpha_v = \frac{1}{v}\left(\frac{\delta V}{\delta T}\right) \qquad (5.3.2)$$

The crystals of small organic molecules are reported to have coefficients of TE ranging from 100–300 × 10^{-6} K^{-1}.[36] The units of linear coefficient of TE are given in reciprocal temperature (K^{-1}) but they are typically expressed in MK^{-1} which is a more convenient unit rather than 10^{-6} K^{-1}.

5.4.Results

5.4.1. Hydrogen bonding in crystal structures

The hydrogen bond motifs in the five targets are compared in (Figure 5.1). All the single crystal structures are sustained by N-H---O=C intermolecular interactions. Graph-set notation was used to describe the observed H-bond networks in detail. Graph Set Notation is a tool used to explain H-bonding patterns in crystals and it was designed by Etter and co-workers.[37] They performed a comprehensive Cambridge Structural Database (CSD) analysis on the preference for singular functional groups and their arrangements in solids.[37-39] Subsequently they developed a general formula to describe the observed patterns, given as $G_d^a(r)$, where G is the graphical descriptor of the motif (S-

intramolecular, C-chain, R-ring, D-discrete bonds), 'a' is the number of acceptor atoms, 'd' is the number of donor atoms and 'r' is the number of atoms involved in the motif. Compounds **DC4-DC6** are structurally similar, they differ in that the chain length increases from **DC4**, **DC5**, to **DC6** respectively. In **DC4** the compound crystallizes in the C2/c monoclinic space group, and hydrogen-bonding pattern can be described by the $R_2^2(8)$ graph set constructed by N-H···O=C (Figure 5-1a). The extended hydrogen-bonding motif assembles into a 2D network via two types of chains which are crossed in the form $C_1^1(4)$ formed via N7-H7···O=C.

In **DC5** and **DC6** both compounds crystallize in the *P-1* triclinic space group. Similar to **DC4**, **DC5** and **DC6** are primarily held together by $R_2^2(8)$graph set formed via N-H···O=C (Figure 5-1b, 5-1c). In addition, $C_1^1(13)$and $C_1^1(15)$ chains are present in **DC5** and **DC6** respectively. Unlike in **DC4** where perpendicular chains are formed, the extended hydrogen bonding motifs of **DC5** and **DC6** form $R_4^2(8)$rings which bridge between the 2D chains.

In **DC7**, the structural backbone changes altogether from the fluorinated dicarbamates in **DC4-DC6** to a non-fluorinated tri-carbamate (Figure 5-1d). **DC7** crystallizes in the P21/n space group. The hydrogen bonding pattern is dictated by $R_2^2(8)$ and $R_4^2(8)$ graph sets which is the same as in **DC5** and **DC6**. Compound **DC8** is a tetra-carbamate and

crystallizes in the *I4* tetragonal space group. In **DC8**, a unique hydrogen bonding pattern was observed whereby only one type of graph set $R_4^4(16)$ holds the molecules throughout the assembly (Figure 5-1e).

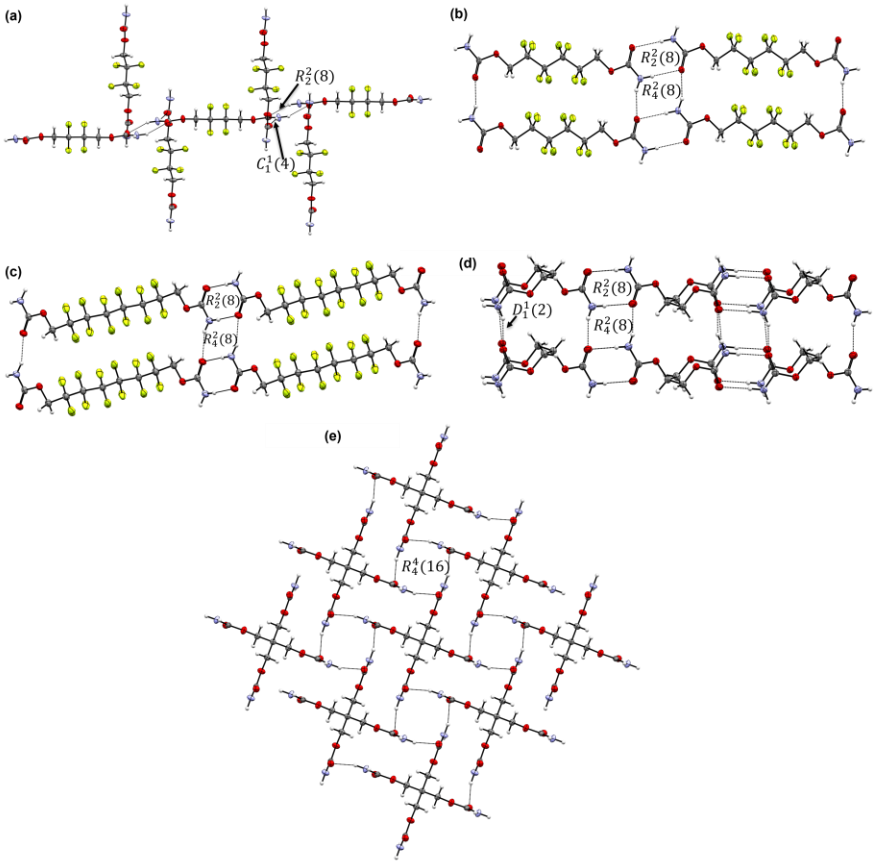

Figure 5-1 Hydrogen bonding motifs in target crystal structures described using the graph set notation (a) DC4 (b) DC5 (c) DC6 (d) DC7 (e) DC8

Tables 5-1 to 5-4 show the summarized crystallographic information of each target at different temperatures (250, 230, 210, 190, 170, 150 K). It is noteworthy that the unit cell parameters (**a, b, c**) are changing at different temperatures which shows that the compounds are thermally responsive.

Table 5-1 Crystallographic data of **DC4** showing how unit cell parameters change with temperature.

DC4						
Identification code	exp_381_1_250	exp_381_2_230	exp_381_3_210	exp_381_4_190	exp_381_5_170	exp_381_6_150
Empirical formula	$C_6H_8F_4N_2O_4$	$C_6H_8F_4N_2O_4$	$C_6H_8F_4N_2O_4$	$C_6H_8F_4N_2O_4$	$C_6H_8F_4N_2O_4$	$C_6H_8F_4N_2O_4$
Formula weight	248.14	248.14	248.14	248.14	248.14	248.14
Temperature/K	**250(2)**	**230(2)**	**210(2)**	**190(2)**	**170(2)**	**150(2)**
Crystal system	monoclinic	monoclinic	monoclinic	monoclinic	monoclinic	monoclinic
Space group	C2/c	C2/c	C2/c	C2/c	C2/c	C2/c
a/Å	16.5323(5)	16.5102(4)	16.4846(4)	16.4590(4)	16.4339(4)	16.4044(6)
b/Å	6.0556(2)	6.0608(2)	6.06630(10)	6.07270(10)	6.0772(2)	6.0866(2)
c/Å	9.9470(3)	9.9358(3)	9.9247(3)	9.9150(3)	9.9036(3)	9.8937(4)
α/°	90	90	90	90	90	90
β/°	104.508(3)	104.560(3)	104.605(3)	104.655(3)	104.704(3)	104.776(4)
γ/°	90	90	90	90	90	90
Volume/Å^3	964.07(5)	962.30(5)	960.41(4)	958.77(4)	956.70(5)	955.19(6)
Z	4	4	4	4	4	4
ρ_{calc}g/cm^3	1.710	1.713	1.716	1.719	1.723	1.726
μ/mm^{-1}	1.701	1.704	1.707	1.710	1.714	1.716
F(000)	504.0	504.0	504.0	504.0	504.0	504.0
Radiation	CuKα(λ = 1.54184)	CuKα (λ = 1.54184)	CuKα (λ = 1.54184)	CuKα (λ = 1.54184)	CuKα (λ = 1.54184)	CuKα (λ = 1.54184)
2Θ range for data collection/°	11.056 to 154.324	11.074 to 153.138	11.094 to 152.976	11.114 to 152.85	11.132 to 153.376	11.156 to 152.888
Index ranges	-20 ≤ h ≤ 20, -5 ≤ k ≤ 7, -12 ≤ l ≤ 12	-20 ≤ h ≤ 20, -5 ≤ k ≤ 7, -12 ≤ l ≤ 12	-20 ≤ h ≤ 20, -5 ≤ k ≤ 7, -12 ≤ l ≤ 12	-19 ≤ h ≤ 20, -5 ≤ k ≤ 7, -12 ≤ l ≤ 12	-19 ≤ h ≤ 20, -5 ≤ k ≤ 7, -12 ≤ l ≤ 12	-19 ≤ h ≤ 20, -5 ≤ k ≤ 7, -12 ≤ l ≤ 12
Reflections collected	3259	3249	3242	3222	3158	3065
Independent reflections	977 [R_{int} = 0.0150, R_{sigma} = 0.0132]	975 [R_{int} = 0.0164, R_{sigma} = 0.0139]	972 [R_{int} = 0.0153, R_{sigma} = 0.0131]	972 [R_{int} = 0.0140, R_{sigma} = 0.0116]	968 [R_{int} = 0.0190, R_{sigma} = 0.0144]	966 [R_{int} = 0.0280, R_{sigma} = 0.0201]
Data/restraints/ parameters	977/0/82	975/0/90	972/0/90	972/0/82	968/0/90	966/0/82
Goodness-of-fit on F^2	1.136	1.090	1.077	1.077	1.083	1.130
Final R indexes [I>=2σ (I)]	R_1 = 0.0297, wR_2 = 0.0783	R_1 = 0.0286, wR_2 = 0.0749	R_1 = 0.0283, wR_2 = 0.0743	R_1 = 0.0273, wR_2 = 0.0677	R_1 = 0.0286, wR_2 = 0.0755	R_1 = 0.0349, wR_2 = 0.1018
Final R indexes [all data]	R_1 = 0.0305, wR_2 = 0.0790	R_1 = 0.0293, wR_2 = 0.0761	R_1 = 0.0289, wR_2 = 0.0747	R_1 = 0.0280, wR_2 = 0.0682	R_1 = 0.0294, wR_2 = 0.0761	R_1 = 0.0360, wR_2 = 0.1027
Largest diff. peak/hole / e Å^{-3}	0.30/-0.16	0.30/-0.19	0.29/-0.20	0.34/-0.18	0.32/-0.19	0.47/-0.24

Table 5-2 Crystallographic data of **DC5** showing how unit cell parameters change with temperature.

DC5						
Identification code	exp_382_1_250	exp_382_2_230	exp_382_3_210	exp_382_4_190	exp_382_5_170	exp_382_6_150
Empirical formula	$C_8H_8F_8N_2O_4$	$C_8H_8F_8N_2O_4$	$C_8H_8F_8N_2O_4$	$C_8H_8F_8N_2O_4$	$C_8H_8F_8N_2O_4$	$C_8H_8F_8N_2O_4$
Formula weight	348.16	348.16	348.16	348.16	348.16	348.16
Temperature/K	250(2)	230(2)	210(2)	190(2)	170(2)	150(2)
Crystal system	triclinic	triclinic	triclinic	triclinic	triclinic	triclinic
Space group	P-1	P-1	P-1	P-1	P-1	P-1
a/Å	5.13895(17)	5.13551(13)	5.13197(13)	5.1278(2)	5.1250(2)	5.1210(3)
b/Å	6.2821(2)	6.2724(2)	6.2647(2)	6.2585(3)	6.2509(3)	6.2443(3)
c/Å	9.9177(4)	9.8945(3)	9.8728(3)	9.8548(5)	9.8340(5)	9.8161(5)
α/°	91.140(3)	90.825(3)	90.565(3)	90.374(4)	90.069(4)	89.829(4)
β/°	104.394(3)	104.428(2)	104.470(2)	104.528(4)	104.508(4)	104.536(5)
γ/°	102.228(3)	102.399(2)	102.535(3)	102.644(4)	102.798(4)	102.911(4)
Volume/Å^3	302.20(2)	300.691(15)	299.328(15)	298.09(2)	296.88(2)	295.69(3)
Z	1	1	1	1	1	1
ρ_{calc}g/cm^3	1.913	1.923	1.931	1.939	1.947	1.955
μ/mm^{-1}	2.075	2.085	2.095	2.104	2.112	2.121
F(000)	174.0	174.0	174.0	174.0	174.0	174.0
Radiation	CuKα (λ = 1.54184)	CuKα (λ = 1.54184)	CuKα (λ = 1.54184)	CuKα (λ = 1.54184)	CuKα (λ = 1.54184)	CuKα (λ = 1.54184)
2Θ range for data collection/°	9.234 to 153.578	9.252 to 153.16	9.272 to 154.212	9.29 to 153.008	9.306 to 154.274	9.322 to 154.516
Index ranges	$-6 \le h \le 3$, $-7 \le k \le 7$, $-12 \le l \le 12$	$-6 \le h \le 3$, $-7 \le k \le 7$, $-12 \le l \le 12$	$-6 \le h \le 3$, $-7 \le k \le 7$, $-12 \le l \le 12$	$-6 \le h \le 3$, $-7 \le k \le 7$, $-12 \le l \le 12$	$-6 \le h \le 3$, $-7 \le k \le 7$, $-12 \le l \le 12$	$-6 \le h \le 3$, $-7 \le k \le 7$, $-12 \le l \le 12$
Reflections collected	3665	3635	3611	3596	3547	3523
Independent reflections	1224 [R_{int} = 0.0174, R_{sigma} = 0.0139]	1228 [R_{int} = 0.0179, R_{sigma} = 0.0141]	1230 [R_{int} = 0.0179, R_{sigma} = 0.0136]	1231 [R_{int} = 0.0180, R_{sigma} = 0.0129]	1231 [R_{int} = 0.0206, R_{sigma} = 0.0145]	1213 [R_{int} = 0.0206, R_{sigma} = 0.0140]
Data/restraints/ parameters	1224/0/109	1228/0/109	1230/0/109	1231/0/109	1231/0/109	1213/0/109
Goodness-of-fit on F^2	1.025	1.038	1.034	1.063	1.131	1.132
Final R indexes [I>=2σ (I)]	R_1 = 0.0371, wR_2 = 0.1032	R_1 = 0.0359, wR_2 = 0.0995	R_1 = 0.0350, wR_2 = 0.0986	R_1 = 0.0353, wR_2 = 0.1001	R_1 = 0.0356, wR_2 = 0.0991	R_1 = 0.0390, wR_2 = 0.1181
Final R indexes [all data]	R_1 = 0.0381, wR_2 = 0.1043	R_1 = 0.0368, wR_2 = 0.1007	R_1 = 0.0360, wR_2 = 0.0996	R_1 = 0.0362, wR_2 = 0.1009	R_1 = 0.0368, wR_2 = 0.1002	R_1 = 0.0400, wR_2 = 0.1191
Largest diff. peak/hole / e Å^{-3}	0.33/-0.24	0.30/-0.23	0.30/-0.23	0.31/-0.28	0.23/-0.29	0.26/-0.28

Table 5-3 Crystallographic data of **DC7** showing how unit cell parameters change with temperature.

DC7						
Identification code	exp_384_1_250	exp_384_2_230	exp_384_3_210	exp_384_4_190	exp_384_5_170	exp_384_6_150
Empirical formula	$C_6H_{11}N_3O_6$	$C_6H_{11}N_3O_6$	$C_6H_{11}N_3O_6$	$C_6H_{11}N_3O_6$	$C_6H_{11}N_3O_6$	$C_6H_{11}N_3O_6$
Formula weight	221.18	221.18	221.18	221.18	221.18	221.18
Temperature/K	250(2)	230(2)	210(2)	190(2)	170(2)	150(2)
Crystal system	monoclinic	monoclinic	monoclinic	monoclinic	monoclinic	monoclinic
Space group	$P2_1/n$	$P2_1/n$	$P2_1/n$	$P2_1/n$	$P2_1/n$	$P2_1/n$
a/Å	5.0904(3)	5.0894(3)	5.0900(3)	5.0887(3)	5.0908(3)	5.0923(3)
b/Å	17.3230(9)	17.3145(8)	17.3024(8)	17.3007(8)	17.2968(10)	17.2839(9)
c/Å	10.7598(7)	10.7458(7)	10.7378(7)	10.7217(7)	10.7098(8)	10.6979(8)
α/°	90	90	90	90	90	90
β/°	101.019(6)	101.054(6)	101.112(6)	101.132(6)	101.129(7)	101.151(6)
γ/°	90	90	90	90	90	90
Volume/Å^3	931.32(10)	929.36(9)	927.94(9)	926.16(9)	925.31(11)	923.80(10)
Z	4	4	4	4	4	4
ρ_{calc}g/cm^3	1.577	1.581	1.583	1.586	1.588	1.590
μ/mm^{-1}	1.241	1.244	1.246	1.248	1.249	1.251
F(000)	464.0	464.0	464.0	464.0	464.0	464.0
Radiation	CuKα (λ = 1.54184)	CuKα (λ = 1.54184)	CuKα (λ = 1.54184)	CuKα (λ = 1.54184)	CuKα (λ = 1.54184)	CuKα (λ = 1.54184)
2Θ range for data collection/°	9.808 to 152.536	9.82 to 152.552	9.828 to 152.454	9.84 to 152.602	9.848 to 152.88	9.86 to 152.564
Index ranges	$-6 \le h \le 5$, $-21 \le k \le 21$, $-13 \le l \le 13$	$-5 \le h \le 6$, $-21 \le k \le 21$, $-13 \le l \le 13$	$-6 \le h \le 5$, $-21 \le k \le 21$, $-13 \le l \le 13$	$-6 \le h \le 5$, $-21 \le k \le 21$, $-13 \le l \le 13$	$-5 \le h \le 6$, $-21 \le k \le 21$, $-13 \le l \le 13$	$-6 \le h \le 5$, $-21 \le k \le 21$, $-13 \le l \le 13$
Reflections collected	5836	5798	5797	5746	5713	5702
Independent reflections	1823 [R_{int} = 0.0465, R_{sigma} = 0.0438]	1817 [R_{int} = 0.0448, R_{sigma} = 0.0427]	1814 [R_{int} = 0.0451, R_{sigma} = 0.0410]	1814 [R_{int} = 0.0470, R_{sigma} = 0.0429]	1805 [R_{int} = 0.0421, R_{sigma} = 0.0371]	1797 [R_{int} = 0.0443, R_{sigma} = 0.0418]
Data/restraints/ parameters	1823/0/160	1817/0/160	1814/0/160	1814/0/160	1805/0/160	1797/0/160
Goodness-of-fit on F^2	1.084	1.117	1.110	1.092	1.180	1.105
Final R indexes [I>=2σ (I)]	R_1 = 0.0541, wR_2 = 0.1379	R_1 = 0.0568, wR_2 = 0.1481	R_1 = 0.0526, wR_2 = 0.1386	R_1 = 0.0560, wR_2 = 0.1432	R_1 = 0.0586, wR_2 = 0.1577	R_1 = 0.0588, wR_2 = 0.1425
Final R indexes [all data]	R_1 = 0.0703, wR_2 = 0.1451	R_1 = 0.0715, wR_2 = 0.1543	R_1 = 0.0678, wR_2 = 0.1445	R_1 = 0.0748, wR_2 = 0.1539	R_1 = 0.0714, wR_2 = 0.1639	R_1 = 0.0711, wR_2 = 0.1480
Largest diff. peak/hole / e Å^{-3}	0.25/-0.19	0.25/-0.22	0.26/-0.20	0.26/-0.24	0.25/-0.24	0.27/-0.24

Table 5-4 Crystallographic data of **DC8** showing how unit cell parameters change with temperature.

DC8						
Identification code	exp_391_1_250	exp_391_2_230	exp_391_3_210	exp_391_4_190	exp_391_5_170	exp_391_6_150
Empirical formula	$C_9H_{16}N_4O_8$	$C_9H_{16}N_4O_8$	$C_9H_{16}N_4O_8$	$C_9H_{16}N_4O_8$	$C_9H_{16}N_4O_8$	$C_9H_{16}N_4O_8$
Formula weight	308.26	308.26	308.26	308.26	308.26	308.26
Temperature/K	250(2)	230.00(10)	210(2)	190(2)	170(2)	150.00(10)
Crystal system	tetragonal	tetragonal	tetragonal	tetragonal	tetragonal	tetragonal
Space group	I-4	I-4	I-4	I-4	I-4	I-4
a/Å	11.3305(2)	11.3142(2)	11.29999(17)	11.2854(2)	11.2712(2)	11.2568(2)
b/Å	11.3305(2)	11.3142(2)	11.29999(17)	11.2854(2)	11.2712(2)	11.2568(2)
c/Å	5.06860(10)	5.06580(10)	5.06298(12)	5.06060(10)	5.05810(10)	5.05560(10)
α/°	90	90	90	90	90	90
β/°	90	90	90	90	90	90
γ/°	90	90	90	90	90	90
Volume/Å^3	650.71(3)	648.48(3)	646.49(2)	644.52(3)	642.58(3)	640.62(3)
Z	2	2	2	2	2	2
ρ_{calc}g/cm^3	1.573	1.579	1.584	1.588	1.593	1.598
μ/mm^{-1}	1.212	1.216	1.220	1.224	1.227	1.231
F(000)	324.0	324.0	324.0	324.0	324.0	324.0
Crystal size/mm^3	0.3 × 0.1 × 0.07	0.3 × 0.1 × 0.07	0.3 × 0.1 × 0.07	0.3 × 0.1 × 0.07	0.3 × 0.1 × 0.07	0.3 × 0.1 × 0.07
Radiation	CuKα (λ = 1.54184)	Cu Kα (λ = 1.54184)	CuKα (λ = 1.54184)	CuKα (λ = 1.54184)	CuKα (λ = 1.54184)	Cu Kα (λ = 1.54184)
2Θ range for data collection/°	11.044 to 155.006	11.06 to 151.122	11.074 to 151.688	11.088 to 152.28	11.102 to 152.872	11.116 to 153.486
Index ranges	-13 ≤ h ≤ 13, -14 ≤ k ≤ 11, -6 ≤ l ≤ 6	-13 ≤ h ≤ 13, -14 ≤ k ≤ 11, -6 ≤ l ≤ 6	-13 ≤ h ≤ 13, -14 ≤ k ≤ 11, -6 ≤ l ≤ 6	-13 ≤ h ≤ 13, -14 ≤ k ≤ 11, -6 ≤ l ≤ 6	-13 ≤ h ≤ 13, -14 ≤ k ≤ 11, -6 ≤ l ≤ 6	-13 ≤ h ≤ 13, -14 ≤ k ≤ 11, -6 ≤ l ≤ 6
Reflections collected	3094	3078	3071	3070	2916	3041
Independent reflections	664 [R_{int} = 0.0270, R_{sigma} = 0.0182]	661 [R_{int} = 0.0282, R_{sigma} = 0.0185]	659 [R_{int} = 0.0273, R_{sigma} = 0.0179]	655 [R_{int} = 0.0279, R_{sigma} = 0.0184]	654 [R_{int} = 0.0950, R_{sigma} = 0.0556]	652 [R_{int} = 0.0310, R_{sigma} = 0.0197]
Data/restraints/ parameters	664/0/57	661/0/57	659/0/57	655/0/57	654/0/57	652/0/57
Goodness-of-fit on F^2	1.098	1.108	1.117	1.124	1.060	1.106
Final R indexes [I>=2σ (I)]	R_1 = 0.0225, wR_2 = 0.0627	R_1 = 0.0223, wR_2 = 0.0606	R_1 = 0.0214, wR_2 = 0.0599	R_1 = 0.0223, wR_2 = 0.0590	R_1 = 0.0424, wR_2 = 0.1114	R_1 = 0.0235, wR_2 = 0.0634
Final R indexes [all data]	R_1 = 0.0226, wR_2 = 0.0628	R_1 = 0.0224, wR_2 = 0.0607	R_1 = 0.0216, wR_2 = 0.0601	R_1 = 0.0225, wR_2 = 0.0591	R_1 = 0.0426, wR_2 = 0.1118	R_1 = 0.0236, wR_2 = 0.0635
Largest diff. peak/hole / e Å^{-3}	0.14/-0.10	0.13/-0.11	0.12/-0.10	0.12/-0.12	0.22/-0.22	0.13/-0.13

5.5. Discussion

5.5.1. Thermal expansion (TE) properties and crystal packing of targets

Thermal expansion coefficients (α) were calculated using PASCal[40]. In general, the linear thermal expansion coefficients (α_{X1}, α_{X2}, and α_{X3}), are measured along the three principal axes of thermal expansion (X_1, X_2, and X_3), which determined by the expansion/contraction behavior of molecules in the crystal lattice at different temperatures.[41] Figure 5-2 illustrates the crystallographic unit cell (a,b,c) and the principal axes (X_1, X_2, and X_3) for the thermal expansion in the DC4 crystal structure. This demonstration helps to visualize the planes associated with TE and direction of thermal expansion (X_1, X_2, and X_3) which is perpendicular to the planes as they appear in the crystal lattice (Figure 5-2a-5-2c).

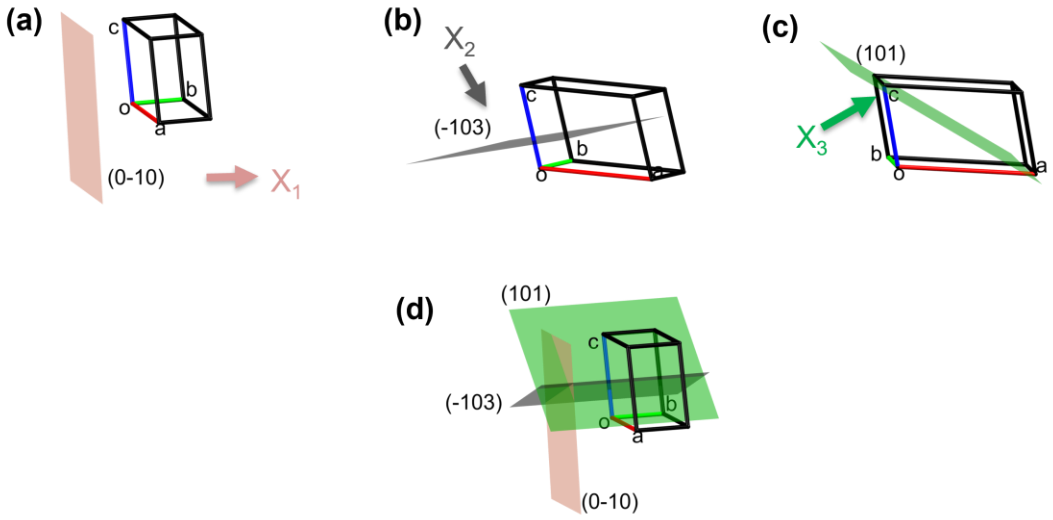

Figure 5-2 Representation of DC4 crystal structure showing the crystallographic axis. The planes were TE occurs and principal axes (a) X_1, (b) X_2, (c) X_3 showing the direction thermal expansion, and (d) all the planes shown on the same axis.

TE analysis of DC4 **along X_1 and X_2 axes: DC4** exhibits negative thermal expansion (NTE) along X_1 (α_{X1}= −49 MK^{-1}) (Table 5-5). Packing in **DC4** consists of 2D chains (Figure 5-3a). that are sustained by the robust $R_2^2(8)$ rings, while neighboring chains are held together by N-H···O=C interaction denoted by $C_1^1(4)$ graph set. The NTE along X_1 is due to the strongest hydrogen bonds in the structure (N-H···O=C dimers) which lie along the X_1 direction as well as contraction of the a-axis upon heating. The solid shows limited positive thermal expansion (PTE) along the X_2 axis (α_{X2}=45 MK^{-1}). The X_2 axis involves the N-H···O=C interactions denoted by $C_1^1(4)$ graph set that bridges horizontal and vertical chains. The coefficients along X_1 and X_2 are −49 MK^{-1} and 45 MK^{-1} respectively, therefore the coefficients nearly cancel each other out, resulting in two-dimensional zero TE behavior. The linear TE coefficients (α_{X1}, α_{X2}, and α_{X3}) along the principal axes (X_1, X_2, and X_3) and their directions with respect to the crystallographic axes for each target are shown in (Table 5-5).

Table 5-5 TE Coefficients (250-150K) for targets with errors in parentheses and approximate crystallographic axes in brackets

Target	α_{X1} (MK^{-1}) [axis]	α_{X2} (MK^{-1}) [axis]	α_{X3} (MK^{-1}) [axis]
DC4	-49 (3) [0 -1 0]	45 (1) [-1 0 3]	99 (2) [1 0 1]
DC5	-41 (1) [-3 8 4]	58 (2) [4 1 1]	200 (4) [-1 -3 2]
DC6	-1 (4) [2 3 2]	85 (3) [1 0 0]	211 (3) [0 1 0]
DC7	-3 (2) [-1 0 0]	21 (2) [0 1 0]	59 (5) [1 0 3]
DC8	26 (0) [0 0 1]	65 (1) [-1 -1 0]	65 (1) [1 -1 0]

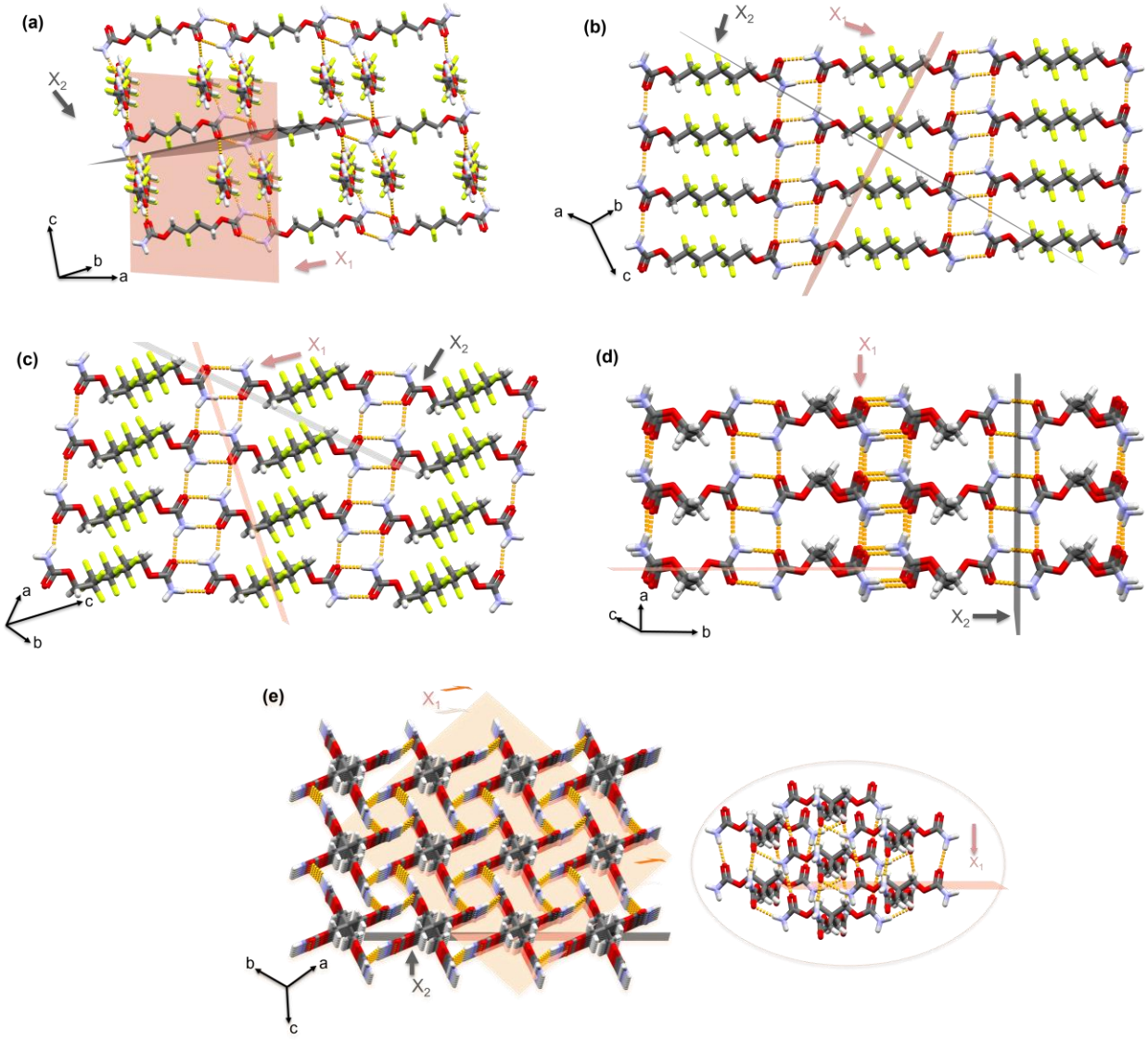

Figure 5-3 Single-crystal structures showing 2D hydrogen-bonded sheet and direction of TE along X1 and X2 axes for (a) DC4 (b) DC5 (c) DC6 (d) DC7 (e) DC8

TE analysis of DC5 **and** DC6 **along X_1 and X_2 axes: DC5** displays negative TE along X_1 (α_{X1}= −41 MK^{-1}), while for **DC6.** TE coefficients along X_1 are nearly zero (α_{X1}= −1 MK^{-1}) as a result **DC6** exhibits uniaxial ZTE along X_1. For both **DC5** and **DC6**, the hydrogen-bonded dimers are the strongest interactions along X_1, and consequently are least affected

by changes in temperature. The extended motifs of both solids generate similar 2D sheets held together by N-H···O=C hydrogen bonds (Figure 5-3b and 5-3c). **DC5** exhibits limited PTE while **DC6** exhibits significant PTE with TE coefficients of 58 MK^{-1} and 85 MK^{-1} respectively. The X_2 axis encompasses the N-H···O=C interactions that form $R_2^2(8)$ and $R_4^2(8)$ rings which eventually construct 2D sheets.

It is worth noting that the TE behavior of **DC5** and **DC6** along X_1 and X_2 are significantly different despite forming similar 2D sheets that are held together by the same type of rings and interactions. In fact, **DC5** TE coefficients (α_{X1}= −41 MK^{-1}, α_{X2}= 58 MK^{-1}) are similar to TE coefficients of **DC4** (α_{X1}= −49 MK^{-1}, α_{X2}= 45 MK^{-1}) which indicates that increasing the chain length from **DC4** to **DC5** does not significantly impact TE behavior along X_1 and X_2 direction. On the contrary, a substantial shift in TE trend was observed in **DC6** as given by the TE coefficients (α_{X1}= −1 MK^{-1}, α_{X2}= 85 MK^{-1}).

TE Behavior of DC7 **and** DC8 **along X_1 and X2:** In **DC7**, the N-H···O=C intermolecular interactions along X_1 are moderately strong and form $R_2^2(8)$ and $R_4^2(8)$ rings. When these interactions work together, they eventually construct 2D sheets in the assembly. The structural backbone of **DC7** is a tri-carbamate with two carbamate functional groups laying parallel in a stacked manner in one direction and the third group facing in an opposite direction which fortifies a dense hydrogen-bonded network along the X_1 and X_2

axes of the solid (Figure 5-3d). Owing to the intermolecular interactions along X_1, TE coefficient is nearly zero (α_{X1}= -3 MK^{-1}) thus **DC7** exhibits uniaxial ZTE along X_1. **DC7** shows mild positive thermal expansion (PTE) along the X_2 axis (α_{X2}=21 MK^{-1}). Along the X_2 axis, molecules are joined by dimers and the effect of the stacked dimers which minimize the TE is evident by the limited TE coefficient of 21 MK^{-1}. **DC8** is a symmetrical tetra-carbamate which aggregates to form a 3D network via N-H···O=C intermolecular interactions which create by $R_4^4(16)$ graph rings that hold the network together. Notably, amongst all targets in this study **DC8** is the only one that exhibits mild PTE along X_1 (α_{X1}=26 MK^{-1}) whereas **DC4-DC7** displayed NTE and ZTE. This is possibly due to the 3D molecular packing arrangement which allows the molecules room for vibrations along the axes when heated. The intermolecular interactions along X_1 are shown in magnified (Figure 5-3e). In **DC8**, along the X_2 axis, molecules are joined connected via $R_4^4(16)$ rings and moderate TE coefficient of 65 MK^{-1} is shown.

Overall, for our system increasing the functional groups from di>tri>tetra led to a downward trend in TE along X_2 axis. Analysis for TE behavior along X_1 shows an upward trend where TE coefficients change from NTE>ZTE>PTE.

TE analysis of targets along X_3 axis: The highest TE occurs along the X_3 axis for all five target compounds (Figure 5-4). In **DC4**, the crossed chains stack without interlocking and

there are no robust interactions in-between the chains hence a higher PTE of 99 MK^{-1} is exhibited by the solid (Figure 5-4a). **DC5** and **DC6** had substantially higher coefficients of TE, and both solids exhibit unique behavior known as colossal TE (α_{X3}= 200 MK^{-1}, α_{X3}= 211 MK^{-1}) respectively. In **DC5**, molecules pack to form almost flat 2D sheets and adjacent sheets stack and no intermolecular interactions could be identified between the sheets. The packing behavior in **DC6** is similar to **DC5** except the 2D sheets form a wave like pattern and not the flat sheets as in **DC5**. The lack of interlayer interactions allows for maximum TE along X_3 axis, and this justifies the magnitude of the coefficients of TE.

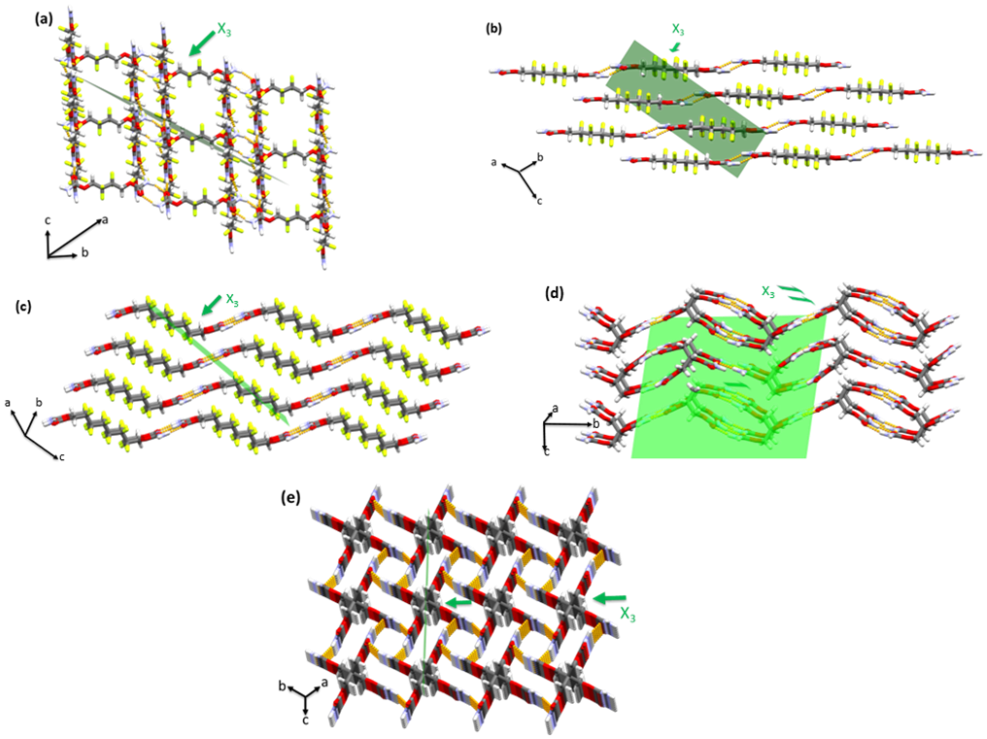

Figure 5-4 Single-crystal X-ray structures showing packing and TE along X3 axis for (a) DC4 (b) DC5 (c) DC6 (d) DC7 (e) DC8

For **DC7** and **DC8**, coefficients of TE are (α_{X3}= 59 MK^{-1}, α_{X3}= 65 MK^{-1}), respectively. Despite having the highest TE coefficients along X_3 for the individual solids, these values are significantly lower than **DC4-DC6**. Going from **DC4** to **DC6** an increase in TE coefficients is seen. However, going from **DC6** to **DC7** and **DC8** it is apparent that altering the molecular design and dimensions affects the extend of TE of solid-state materials. Careful analysis shows that functionality, molecular dimensionality and packing collectively can be used to rationalize the observed TE in these solids.

5.5.2. Energy Framework Calculations

To further rationalize the TE properties of the solids, the intermolecular interactions were assessed using energy framework calculation. Such analysis can be used to better comprehend crystal packing by combining rapid computation of intermolecular interaction energy with a unique graphical depiction of their magnitude.[42] The estimation of energy frameworks is based on the interaction energies calculated by CrystalExplorer. The crystallographic information file (cif) obtained by solving the single crystal X-ray diffraction data was used as the input file for CrystalExplorer software for performing energy frameworks calculations. The interaction energies between molecules are calculated by first defining a sphere with a 3.80 Å radius around a center molecule and the fragments of all the molecules within that sphere were then completed and the energy frameworks calculation was performed.

Energy interactions between molecular pairs are depicted as cylinders connecting the centroids of two molecules, with the radius of the cylinder corresponding to the magnitude of the interaction energy. Frameworks can be built for a variety of purposes. Studies have been conducted where energy framework analysis is used to rationalize materials properties with intermolecular interactions.[43-46] For example, Reddy and co-workers[47] used the energy framework tool to understand mechanical properties of three polymorphs and they found that, for their system, bending behavior could be attributed to the anisotropy of packing and intermolecular interactions.

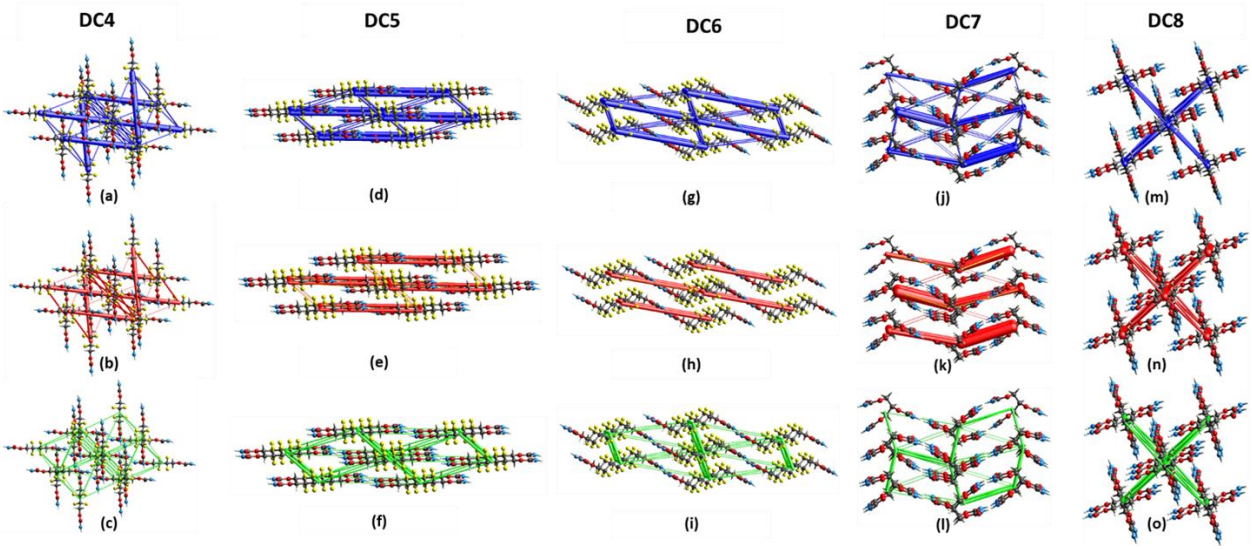

Figure 5-5 Energy frameworks (a, d, g, j, m) total interaction energy (blue), (b, e, h, k, n) dispersion (green), and (c, f, i, l, o) electrostatic components (red) for DC4, DC5, DC6, DC7, and DC8

Table 5-6 Calculated Interaction Energies for DC4, DC5, DC6, DC7, and DC8

	E_{ele}	E_{pol}	E_{dis}	E_{rep}	E_{tot} **(kJ/mol)**
DC4	-97.9	-21.1	-19.1	20.7	-122.9
DC5	-112.5	-24.7	-48	44.6	-151.4
DC6	-128.3	-24.7	-60.1	50.9	-174.8
DC7	-311.9	-69.2	-72.1	258.0	-284.2
DC8	-141.0	-36.1	-79.1	140.5	-157.8

The frameworks corresponding to the total, dispersion term, and electrostatic term interaction energies (IE) are depicted in (Figure 5-4). The energy components calculated within this method are electrostatic, polarization, dispersion, and exchange-repulsion (Table 5-6): In the case of **DC4**, the aggregate of total interaction energies of molecules forming chains was found to be −122.9 kJ/mol. For **DC4**, the energy framework (Figure 5-4b) shows the highest IE is due to electrostatic components and this includes the N−H···O=C intermolecular interaction depicted by $C_1^1(4)$ graph set and the N−H···O=C hydrogen bonds within $R_2^2(8)$ dimers.

For **DC5** and **DC6** the total interaction energies of molecules forming layers of 2D sheets was found to be −151.4 kJ/mol and -174.8 kJ/mol respectively, which includes N−H···O=C hydrogen bonds between $R_2^2(8)$ and $R_4^2(8)$ rings. The electrostatic interaction contributions are highest which suggests why the TE was minimal along the axes encompassing those interactions (Figure 5-4e, 5-4h). Furthermore, dispersion interactions

are present but weak between the chains and sheets which explains why TE was particularly higher along the direction (Figure 5-4c, 5-4f, 5-4i).

DC7 had the highest total interaction energy (-284.2kJ/mol) in the series due to the molecular design which has three robust $R_2^2(8)$ dimers (Figure 5-4j). The presence of concentrated electrostatic interactions (Figure 5-4k) in the solid suggests why the least TE (ZTE and mild PTE) was exhibited by the **DC7** in the series. In **DC8** the total interaction energy was -157.8kJ/mol which included N−H···O=C hydrogen bonds via $R_4^4(16)$rings (Figure 5-4m).

5.6.Conclusions

1. Graph set notation was a versatile tool in comparing the hydrogen bonding patterns observed in the five targets.

2. Our results show that that the different thermal expansion behavior is minimal along the direction of the strong N-H---O=C hydrogen bonded interactions in all targets. Intermolecular interactions and packing arrangements in our targets facilitate thermal expansion with changes in temperature.

3. We also have demonstrated that thermal expansion in the lower dimensional dicarbamates is more than that in the higher dimensional tri-carbamate and tetra-carbamate crystals due to large density of the robust hydrogen bonded dimers and

limited expansion as the structure is confined with increase in dimensionality. This was further justified by the energy framework analysis of intermolecular interactions which confirmed that IEs were highest along the direction of the robust N-H---O=C interactions hence the least TE behavior along that direction.

Although there are various factors that regulate the thermal expansion in materials, this work suggests that intermolecular interactions and molecular dimensionality are important parameters which could be used to control the thermal expansion in materials.

5.7. References

1. Kolesnik, I. A.; Potkin, V. I.; Grigoriev, M. S.; Novikov, A. P.; Gomila, R. M.; Podrezova, A. G.; Brazhkin, V. V.; Zubkov, F. I.; Frontera, A., Synthesis, X-ray characterization and DFT calculations of a series of 3-substituted 4,5-dichloroisothiazoles. *CrystEngComm* **2023**.
2. Reinecke, A.; Bertinetti, L.; Fratzl, P.; Harrington, M. J., Cooperative behavior of a sacrificial bond network and elastic framework in providing self-healing capacity in mussel byssal threads. *Journal of Structural Biology* **2016,** *196* (3), 329-339.
3. Shchukin, D. G.; Zheludkevich, M.; Yasakau, K.; Lamaka, S.; Ferreira, M. G. S.; Möhwald, H., Layer-by-Layer Assembled Nanocontainers for Self-Healing Corrosion Protection. *Advanced Materials* **2006,** *18* (13), 1672-1678.
4. Brunsveld, L.; Folmer, B. J. B.; Meijer, E. W.; Sijbesma, R. P., Supramolecular Polymers. *Chemical Reviews* **2001,** *101* (12), 4071-4098.
5. Best, J. P.; Neubauer, M. P.; Javed, S.; Dam, H. H.; Fery, A.; Caruso, F., Mechanics of pH-Responsive Hydrogel Capsules. *Langmuir* **2013,** *29* (31), 9814-9823.
6. Chen, J.; Peng, Q.; Peng, X.; Han, L.; Wang, X.; Wang, J.; Zeng, H., Recent Advances in Mechano-Responsive Hydrogels for Biomedical Applications. *ACS Applied Polymer Materials* **2020,** *2* (3), 1092-1107.
7. Xiao, H.; Lu, W.; Le, X.; Ma, C.; Li, Z.; Zheng, J.; Zhang, J.; Huang, Y.; Chen, T., A multi-responsive hydrogel with a triple shape memory effect based on reversible switches. *Chemical Communications* **2016,** *52* (90), 13292-13295.

8. Liu, H.; Zhang, C.; Sun, W.; Zhang, Z.; Zhou, M.; Wang, W.; Chen, X.; Zeng, X., Scandium Molybdate Nanofibers with Negative Thermal Expansion for Fabricating Composites with Controllable Coefficients of Thermal Expansion. *ACS Applied Nano Materials* **2020,** *3* (7), 7130-7135.
9. Pachoud, E.; Cumby, J.; Lithgow, C. T.; Attfield, J. P., Charge Order and Negative Thermal Expansion in V_2OPO_4. *Journal of the American Chemical Society* **2018,** *140* (2), 636-641.
10. Li, Q.; Lin, K.; Liu, Z.; Hu, L.; Cao, Y.; Chen, J.; Xing, X., Chemical Diversity for Tailoring Negative Thermal Expansion. *Chemical Reviews* **2022,** *122* (9), 8438-8486.
11. Liu, Y.; Mei, D.; Wang, N.; Molokeev, M. S.; Jiang, X.; Lin, Z., Intrinsic Isotropic Near-Zero Thermal Expansion in $Zn_4B_6O_{12}X$ (X = O, S, Se). *ACS Applied Materials & Interfaces* **2020,** *12* (34), 38435-38440.
12. Chen, J.; Xing, X.; Sun, C.; Hu, P.; Yu, R.; Wang, X.; Li, L., Zero Thermal Expansion in PbTiO3-Based Perovskites. *Journal of the American Chemical Society* **2008,** *130* (4), 1144-1145.
13. Ohtani, R.; Grosjean, A.; Ishikawa, R.; Yamamoto, R.; Nakamura, M.; Clegg, J. K.; Hayami, S., Zero in-Plane Thermal Expansion in Guest-Tunable 2D Coordination Polymers. *Inorganic Chemistry* **2017,** *56* (11), 6225-6233.
14. Goodwin, A. L.; Calleja, M.; Conterio, M. J.; Dove, M. T.; Evans, J. S. O.; Keen, D. A.; Peters, L.; Tucker, M. G., Colossal Positive and Negative Thermal Expansion in the Framework Material *Science* **2008,** *319* (5864), 794-797.
15. S. O. Evans, J., Negative thermal expansion materials *Journal of the Chemical Society, Dalton Transactions* **1999,** (19), 3317-3326.
16. Yamamura, Y.; Horikoshi, A.; Yasuzuka, S.; Saitoh, H.; Saito, K., Negative thermal expansion emerging upon structural phase transition in ZrV_2O_7 and HfV_2O_7. *Dalton Transactions* **2011,** *40* (10), 2242-2248.
17. Cahn, R. W., The how and why of thermal contraction. *Nature* **1997,** *386* (6620), 22-23.
18. Salud, J.; Barrio, M.; Lopez, D. O.; Tamarit, J. L.; Alcobe, X., Anisotropy of Intermolecular Interactions from the Study of the Thermal-Expansion Tensor. *Journal of Applied Crystallography* **1998,** *31* (5), 748-757.
19. Ogborn, J. M.; Collings, I. E.; Moggach, S. A.; Thompson, A. L.; Goodwin, A. L., Supramolecular mechanics in a metal–organic framework. *Chemical Science* **2012,** *3* (10), 3011-3017.
20. Grobler, I.; Smith, V. J.; Bhatt, P. M.; Herbert, S. A.; Barbour, L. J., Tunable Anisotropic Thermal Expansion of a Porous Zinc(II) Metal–Organic Framework. *Journal of the American Chemical Society* **2013,** *135* (17), 6411-6414.
21. Wu, Y.; Kobayashi, A.; Halder, G. J.; Peterson, V. K.; Chapman, K. W.; Lock, N.; Southon, P. D.; Kepert, C. J., Negative Thermal Expansion in the Metal–Organic

Framework Material Cu_3(1,3,5-benzenetricarboxylate)$_2$. *Angewandte Chemie International Edition* **2008,** *47* (46), 8929-8932.
22. Lightfoot, P.; Woodcock, D. A.; Maple, M. J.; Villaescusa, L. A.; Wright, P. A., The widespread occurrence of negative thermal expansion in zeolites. *Journal of Materials Chemistry* **2001,** *11* (1), 212-216.
23. Khosrovani, N.; Sleight, A. W.; Vogt, T., Structure of ZrV_2O_7 from −263 to 470°C. *Journal of Solid State Chemistry* **1997,** *132* (2), 355-360.
24. Saraswatula, V. G.; Bhattacharya, S.; Saha, B. K., Can the thermal expansion be controlled by varying the hydrogen bond dimensionality in polymorphs? *New Journal of Chemistry* **2015,** *39* (5), 3345-3348.
25. Saraswatula, V. G.; Saha, B. K., Modulation of Thermal Expansion by Guests and Polymorphism in a Hydrogen Bonded Host. *Crystal Growth & Design* **2015,** *15* (2), 593-601.
26. Bhattacharya, S.; Saha, B. K., Uniaxial Negative Thermal Expansion in an Organic Complex Caused by Sliding of Layers. *Crystal Growth & Design* **2012,** *12* (10), 4716-4719.
27. Bhattacharya, S.; Ganesh, S.; Saha, B., Does Higher-Dimensional Hydrogen Bonding Guarantee a Smaller Thermal Expansion? A Thermal Expansion Study of an Interdigitated 1D and Interpenetrated 3D Hydrogen-Bonded Colored Dimorphic System. *Crystal Growth & Design* **2015,** *16*.
28. Ding, X.; Unruh, D. K.; Groeneman, R. H.; Hutchins, K. M., Controlling thermal expansion within mixed cocrystals by tuning molecular motion capability. *Chemical Science* **2020,** *11* (29), 7701-7707.
29. Hutchins, K. M.; Unruh, D. K.; Verdu, F. A.; Groeneman, R. H., Molecular Pedal Motion Influences Thermal Expansion Properties within Isostructural Hydrogen-Bonded Co-crystals. *Crystal Growth & Design* **2018,** *18* (2), 566-570.
30. Juneja, N.; Unruh, D. K.; George, G. C., III; Hutchins, K. M., Impact of Torsional and Conformational Flexibility on Pedal Motion and Thermal Expansion in Pyridyl Bisimine Cocrystals. *Crystal Growth & Design* **2023,** *23* (1), 524-531.
31. Bhattacharya, S.; Saha, B. K., Interaction Dependence and Similarity in Thermal Expansion of a Dimorphic 1D Hydrogen-Bonded Organic Complex. *Crystal Growth & Design* **2013,** *13* (8), 3299-3302.
32. Turner, M. J.; Grabowsky, S.; Jayatilaka, D.; Spackman, M. A., Accurate and Efficient Model Energies for Exploring Intermolecular Interactions in Molecular Crystals. *The Journal of Physical Chemistry Letters* **2014,** *5* (24), 4249-4255.
33. Chen, J.; Hu, L.; Deng, J.; Xing, X., Negative thermal expansion in functional materials: controllable thermal expansion by chemical modifications. *Chemical Society Reviews* **2015,** *44* (11), 3522-3567.
34. van der Lee, A.; Dumitrescu, D. G., Thermal expansion properties of organic crystals: a CSD study. *Chemical Science* **2021,** *12* (24), 8537-8547.

35. Miller, W.; Smith, C. W.; Mackenzie, D. S.; Evans, K. E., Negative thermal expansion: a review. *Journal of Materials Science* **2009,** *44* (20), 5441-5451.
36. Krishnan, R. S.; Srinivasan, R.; Devanarayanan, S., Chapter 3 - Theory of Thermal Expansion of Crystals. In *Thermal Expansion of Crystals*, Krishnan, R. S.; Srinivasan, R.; Devanarayanan, S., Eds. Pergamon: 1979; Vol. 12, pp 54-104.
37. Etter, M. C.; MacDonald, J. C.; Bernstein, J., Graph-set analysis of hydrogen-bond patterns in organic crystals. *Acta Crystallographica Section B* **1990,** *46* (2), 256-262.
38. Bernstein, J.; Davis, R. E., Graph Set Analysis of Hydrogen Bond Motifs. In *Implications of Molecular and Materials Structure for New Technologies*, Howard, J. A. K.; Allen, F. H.; Shields, G. P., Eds. Springer Netherlands: Dordrecht, 1999; pp 275-290.
39. Groom, C. R.; Bruno, I. J.; Lightfoot, M. P.; Ward, S. C., The Cambridge Structural Database. *Acta Crystallographica Section B* **2016,** *72* (2), 171-179.
40. Cliffe, M. J.; Goodwin, A. L., PASCal: a principal axis strain calculator for thermal expansion and compressibility determination. *Journal of Applied Crystallography* **2012,** *45* (6), 1321-1329.
41. Newnham, R. E., Properties of Materials: Anisotropy, Symmetry, Structure. Oxford University Press: 2004.
42. Spackman, P. R.; Turner, M. J.; McKinnon, J. J.; Wolff, S. K.; Grimwood, D. J.; Jayatilaka, D.; Spackman, M. A., CrystalExplorer: a program for Hirshfeld surface analysis, visualization and quantitative analysis of molecular crystals. *Journal of Applied Crystallography* **2021,** *54* (3), 1006-1011.
43. Torubaev, Y. V.; Rai, D. K.; Skabitsky, I. V.; Pakhira, S.; Dmitrienko, A., Energy framework approach to the supramolecular reactions: interplay of the secondary bonding interaction in Ph2E2 (E = Se, Te)/p-I-C6F4-I co-crystals. *New Journal of Chemistry* **2019,** *43* (21), 7941-7949.
44. Malecka, M.; Checinska, L.; Kusz, J.; Biernacka, M.; Kupcewicz, B., Interactions in flavanone and chalcone derivatives: Hirshfeld surface analysis, energy frameworks and global reactivity descriptors. *Acta Crystallographica Section C* **2020,** *76* (3), 212-224.
45. Zhang, K.; Sun, C. C.; Liu, Y.; Wang, C.; Shi, P.; Xu, J.; Wu, S.; Gong, J., Structural Origins of Elastic and 2D Plastic Flexibility of Molecular Crystals Investigated with Two Polymorphs of Conformationally Rigid Coumarin. *Chemistry of Materials* **2021,** *33* (3), 1053-1060.
46. Reddy, C. M.; Kirchner, M. T.; Gundakaram, R. C.; Padmanabhan, K. A.; Desiraju, G. R., Isostructurality, Polymorphism and Mechanical Properties of Some Hexahalogenated Benzenes: The Nature of Halogen···Halogen Interactions. *Chemistry – A European Journal* **2006,** *12* (8), 2222-2234.
47. Raju, K. B.; Ranjan, S.; Vishnu, V. S.; Bhattacharya, M.; Bhattacharya, B.; Mukhopadhyay, A. K.; Reddy, C. M., Rationalizing Distinct Mechanical Properties of Three Polymorphs of a Drug Adduct by Nanoindentation and Energy Frameworks

Analysis: Role of Slip Layer Topology and Weak Interactions. *Crystal Growth & Design* **2018,** *18* (7), 3927-3937.

Chapter 6 - Capture of Fragrances using Hydrogen-Bonded Organic Frameworks

6.1. Background

6.1.1. Fragrance molecules

Fragrances are essential ingredients, and they are utilized in a variety of products such as food, detergents, personal care products, cosmetics, and perfumes. Fragrant molecules exhibit high volatility, an essential property which enables them to deliver a pleasant olfactory response. On the other hand, this property also can be a disadvantage as it reduces the long-lasting perception of fragrant molecules. The capability to maintain the scent of fragrances for a long period of time is crucial for improving customers' experience and enhancing beneficial effects thus it has attracted tremendous attention in the fragrance industry.[1] Owing to this, there is need to develop delivery systems that can efficiently deposit fragrances in a controlled manner and concurrently provide a long-lasting perception of the volatiles. Currently, the nanotechnology field has made significant progress in developing techniques to control the release of fragrant molecules using nano/microcapsules.[2] These capsules can further be divided into different classes based on the wall material used, for example polymeric capsules, inorganic and polymeric–inorganic capsules.[3, 4] To date, microencapsulation is the leading technology that has been utilized for scent physical encapsulation and storage.[5] This physical encapsulation is stabilized by weak interactions like electrostatic attraction and in some

cases hydrophobic-hydrophobic interactions.[6] Another widely used approach to capture the fragrance into the capsule is the profragrance approach. This is a type of covalent binding where ketone/aldehyde containing fragrances can form a labile covalent bond with hydroxyl functional group which can easily be broken upon exposure to external stimuli such as moisture, pH and temperature.[3, 7, 8]

Although extensive research has been conducted on encapsulation of fragrances with polymeric capsules, the technology still suffers from difficulty to control morphology, pore size and their poor colloidal stability in liquid.[9]

6.1.2. Porous materials as encapsulants

Porous materials such as zeolites, metal–organic frameworks (MOFs), and covalent organic frameworks (COFs) can be good candidates for encapsulation and controlled release of volatiles molecules due to their large surface area, and large pore size, which can overcome some limitations of polymeric capsules. Zeolites and metal–organic frameworks (MOFs) have been widely studied for encapsulation of volatiles.[10, 11]

6.1.2.1. Metal–organic frameworks (MOFs)

MOFs are crystalline and porous solid materials constructed from metal ions and organic ligands. Due to their porous nature and excellent designability they have been studied extensively for applications such as gas storage and catalysis.[12, 13] However, the use of

MOFs for controlled release of fragrant molecules has been explored too, although it is not as prevalent as former applications.

For example, Vaughn and coworkers[14] investigated the use of a zinc-based Rutgers Recyclable Porous Material (RPM) for capture and moisture-controlled release of hydrophilic (ethyl butyrate, EB) and hydrophobic (d-limonene, DL) fragrance compounds. Their findings show that the release profile of EB in RPM3-Zn-ethyl butyrate was achieved after 1 hour. The shorter retention time of EB was attributed to the weaker interaction between hydrophilic EB and hydrophobic porosity of RPM3-Zn MOF. On the other hand, release studies of DL showed that the RPM3-Zn-limonene had a comparatively longer release time of up to 1.5 hours which was attributed to slow dissociation of the framework in solution, whereby water molecules competitively take over ligand sites. Furthermore, a polymeric starch material was used as an encapsulant for comparison and more than 80% of limonene was released instantly. Although, the release of ethyl butyrate and limonene was reduced only for up to ninety minutes, this is significant compared to the pure fragrant molecules which volatilized almost instantly. In the absence of moisture, the release was found to be inactive in both cases.

6.1.2.2. Covalent organic frameworks (COFs)

Another class of porous materials is COFs and these are porous polymers that integrate organic units into extended molecular frameworks with periodically ordered skeletons and well-defined pores. COFs are popular for features like excellent stability and

accessible pores which make them competitive with porous materials such as MOFs.[15] Their key advantage is that due to the nature of covalent bonds they can assemble to form a strong backbone. Unlike MOFs, covalent organic frameworks have not been used for the controlled release of fragrant molecules. However, Liu et. al.[16] reported a COF (3D-COF) based on a hexamethylbiphenyl skeleton which can accurately distinguish between more than twenty kinds of volatile organic frameworks (VOCs), including aromatic, alcohol-based VOCs.

While fundamentally COFs can potentially have these advantages, the challenge that remains is how to incorporate all these features simultaneously. In addition, the covalent bonding is robust and is difficult to manipulate for applications like triggered release of adsorbed material since the trigger will likely rupture the COF backbone.[17] Despite the advantages, the combination of covalent connectivity with crystallinity is difficult to achieve. Additionally, COFs require special functional groups and reaction conditions, which typically are designed for reversible covalent bonds. While the possibility to precisely position functional groups within the pore is a significant advancement of COFs to MOFs, this feature is lost due to the large prevalence of amorphous domains and disordered structures.

6.1.2.3. Hydrogen-bonded organic frameworks (HOFs)

Metal-organic and covalent organic frameworks (MOFs and COFs) have dominated the field of porous materials because of the aforementioned properties.[18, 19] In the same way, hydrogen-bonded organic frameworks (HOFs) have been used for sensing, gas storage and small molecule separation. However, unlike MOFs and COFs which are constructed via coordination and covalent bonds respectively, HOFs have weak hydrogen bonding (H-bonding) connections between discrete building blocks which makes them more versatile because of the reversible nature of the hydrogen-bond formation.[20] As a result, HOFs have some promising advantages. These include highly crystalline structures from a simple solution process that employs H-bonding In addition, this implies that the synthesis is susceptible to the design principles of crystal engineering.[21] Unlike MOFs, the metal component is unnecessary which enables HOFs to be lightweight and potentially environmentally friendly porous structures.

6.1.3. Modes of encapsulation

HOFs present an attractive mode of encapsulating and subsequently releasing fragrance molecules due to the relative easiness of pore design as compared to MOFs and COFs. The HOFs can be designed to retain guest molecules via different strategies, such as physical capture (Scheme 6-1 left), using dynamic covalent bonds and H-bonding. (Scheme 6-1 right). Physical capture is similar to gas adsorption applications, whereby the gas molecules are incorporated into the crystal structure to fill the voids. Dynamic

covalent bonds can be used to create profragrances of HOFs. A profragrance forms a weak covalent bond which can be cleaved when exposed to a stimulus.[22] Finally, the framework interior can be decorated with H-bonding donor and acceptor groups which can enable bonding with the fragrance molecules with appropriate functional groups.

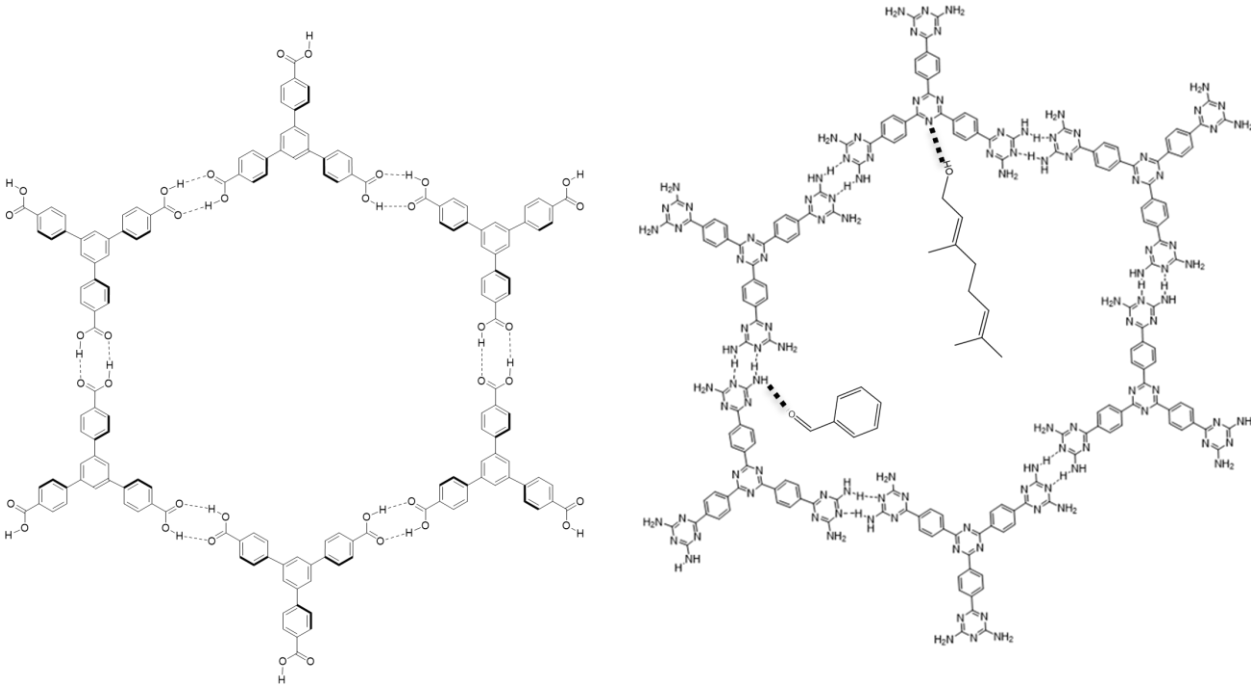

Scheme 6-1 Formation of HOF frameworks with carboxylic acid dimer (left) and N-H---N dimer linkages which can potentially undergo physical and H-bonding encapsulation respectively.

6.1.4. Choice of host and guest molecules

6.1.4.1. Choice of fragrance molecules

For physical capture one of the strategies to capture the fragrance molecules can be using HOFs that have channels that are able to uptake the molecules and occupy the void. Therefore, the size and functionality of fragrance molecules is important. For example, for the fragrance molecules to be incorporated into the framework via hydrogen bonding,

the molecules must contain hydrogen bond donors or acceptors and the interior of the HOF must have functional groups that can also accept or donate hydrogen bonds. As such, fragrance molecules with groups such as hydroxyl groups (alcohols) as H-bond donors and pyridine groups that can accept hydrogen bonding are suitable options.

6.1.4.2. Supramolecular Synthons and Tectons

A tecton is an entity that comprises of the backbone as well as bonding synthons that will hold the molecules together.[23] Having chosen the modes by which the fragrances can be captured, the HOF structure has to be designed by selecting the appropriate framework molecules and the interactions between these molecules.

6.1.4.2.1. Choice of backbone unit

Construction of stable frameworks requires careful selection of tectons. Features such as size, rigidity, planarity, symmetry, functionality, and geometry are crucial as they influence the robustness of the framework.[24] While robustness is a critical requirement for HOF, permanent porosity too is of great importance and so the goal is to build a framework that satisfies both characteristics. Planarity of the frameworks is another key feature. For example, frameworks composed of planar building blocks exhibit large volumes of channels whereas non-planar building blocks tend to cause interpenetration. Interpenetration is a common occurrence that is known to reduce pore size in porous networks. However, although interpenetration reduces pore size in HOFs, such

frameworks tend to be more rigid and thermally stable than nonpenetrated frameworks.[25-27] Thus, all these possible obstacles should be considered when constructing HOFs. The design of physical encapsulation backbone units shown below (Scheme 6.2) lacks additional functional groups and this will enable study of the adsorption capacity of the HOF framework.

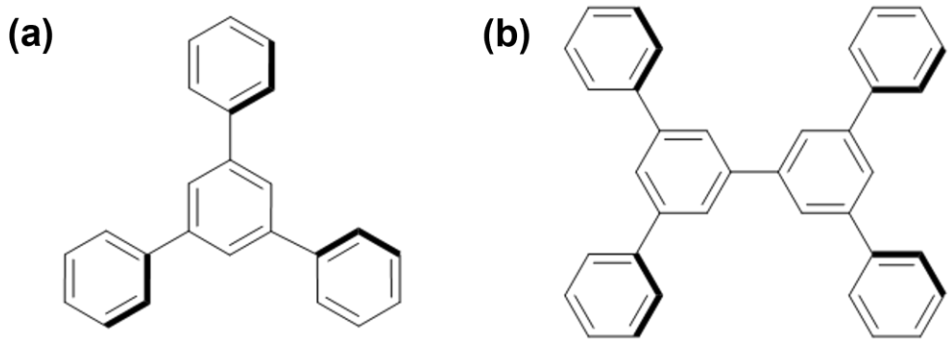

Scheme 6-2 Examples of (a) trigonal and (b) tetrahedron backbone for HOF construction.

6.1.4.2.2. Choice of synthon for holding the frameworks

Complementary to the molecular geometry, the interactions holding these molecules together are very important in the formation of well-defined structures. HOFs can be constructed from small organic molecules held together by H-bonding. As such, compared to covalent bonds in COFs and coordination bonds in MOFs, hydrogen bonds in HOFs are weaker. This enables the fabrication of highly crystalline structures. The choice of the hydrogen bond to hold together the frameworks becomes important. In addition, other non-covalent interactions play significant roles in influencing the HOF

structure. Contributions of weaker interactions such as π–π interactions enables the assembly of low density and robust frameworks.

Hydrogen bonds can be divided into three classes: weak (N≡CH---O, F3C-H---O, alkyl-C-H---O, MeO-H---O, imine≡N---H-O/N), moderate (COOH---O=C-OH, N–H---N/O, COOH---N) and strong hydrogen bonds (charge assisted H-bonds). Hydrogen bonds such as N–H---N and O–H---O have been predominantly used for HOF assembly.[25, 26] Despite showing limited stability, other types of hydrogen bonds (O–H---N and C–H---O) observed in nitrogen- and aldehyde-based structural units such as pyridones, ketones and amino acids have been used for HOF construction.[26] Previous work has shown that H-bonding units like carboxylic acids and 2,4-diaminotriazine form dimers which are stronger hydrogen bonding interactions compared to single donor/acceptor units (Scheme 6-3(a), (b)) and thus can aggregate into a predictable and stable fashion.[28-30]

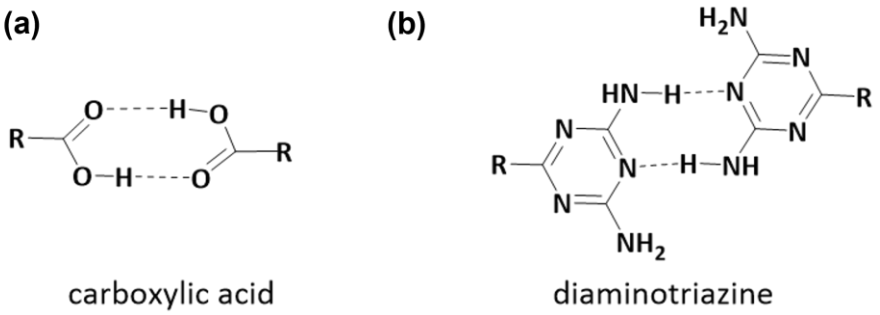

Scheme 6-3 Examples of robust synthons for constructing HOFs

6.2. Goals

Most fragrances are mixtures of volatile organic compounds and provide a pleasant olfactory response. However, high volatility tends to be a drawback because it reduces their effective use as additives in several products. To address the volatility of fragrances, the host trimesic acid (TMA) was selected because it offers robust synthons carboxylic acid dimers and a strong backbone. Additionally, TMA is inexpensive and non-toxic which makes it a good candidate for environmental and large scale applications. TMA is a typical ligand for MOF synthesis and has been widely studied by crystal engineers.[31, 32] The carboxylic acid dimer is easy to synthesize and is a highly directional H-bond and was therefore our choice in the formation of HOFs. Seven fragrance molecules linalool, geraniol, menthol, camphor, isoborneol, α-terpineol and cinnamyl alcohol were selected to investigate for the encapsulation of the volatile materials (Scheme 6-4). These fragrances were selected because they possess functional groups such as hydroxyl groups (alcohols) and ketone (C=O) which can potentially provide H-bond donor and acceptor ability between the host and guest molecules.

In this work we attempt to address the following questions,

1. Can we design a porous and robust HOF?
2. Can HOFs successfully encapsulate fragrance molecules inside their pores via physical encapsulation mode?

3. Can HOFs successfully encapsulate fragrance molecules inside their pores via H-bonding encapsulation mode?
4. Can we quantify the guest molecules encapsulated in the framework pores using TGA analysis?
5. How thermally stable are the frameworks?

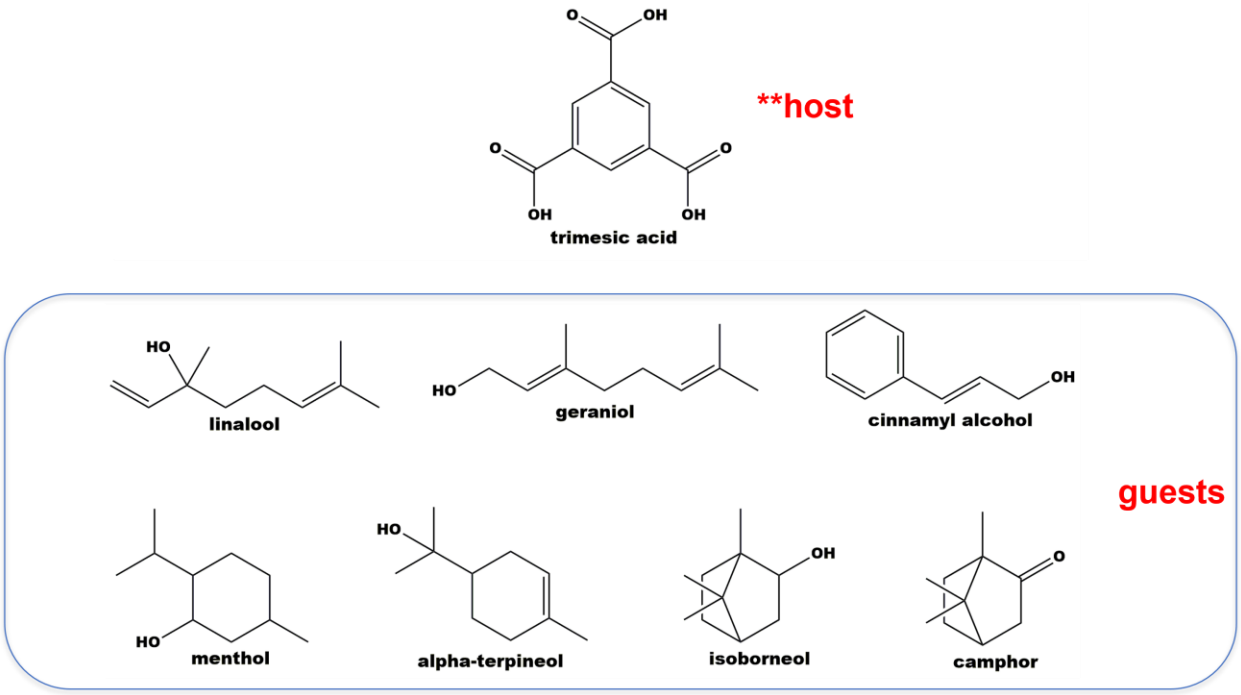

Scheme 6-4 Molecular structures of host and guest fragrances used in this study.

6.3.Experimental

6.3.1. Reagents and General Methods

All reagents were used as received without any further purification. The obtained crystal products were characterized by TGA, ^{1}HNMR, powder X-ray diffraction (PXRD), and

SCXRD. All the NMR spectra were recorded on a Bruker 400 MHz spectrophotometer. Single crystal X-ray diffraction (SCXRD) data were obtained using a Rigaku XtaLAB Synergy-S with a CuKα source. The weight loss profiles were collected using a TA instrument thermogravimetric analysis (TGA) Q20 using TA Universal Analysis software. Samples were heated at a rate of 10 ºC/min under a nitrogen atmosphere. Powder patterns were recorded on a Bruker AXS D8 Advance Phaser diffractometer with Cu Kα radiation (λ = 1.5418 Å).

6.3.2. Crystallization experiments

Co-crystallization experiments were performed by dissolving stoichiometric amounts of the host and fragrance in a known amount of solvent or a mixture of solvents followed by stirring at room temperature for 48hrs. Methanol and tetrahydrofuran (THF) solvents were used in this study and seven fragrance molecules linalool, geraniol, menthol, camphor, isoborneol, α-terpineol and cinnamyl alcohol were used in the attempted co-crystallizations. 14 co-crystallization experiments were set up and the solvents were left to evaporate slowly at room temperature until a crystalline product was formed. Successful uptake of the fragrance guest was confirmed by thermogravimetric analysis (TGA). Out of the 14 co-crystallization attempts, we obtained two co-crystal structures of trimesic acid with α-terpineol and cinnamyl alcohol, respectively.

.

6.3.2.1. Synthesis of TMA·α-terpineol (1)

The fragrance, α-terpineol, (1.76g, 11.4 mmol) was added to a methanol solution (5 mL), of trimesic acid (0.3 g, 1.4 mmol). The mixture was stirred at room temperature for 48 hrs in a sealed scintillation vial. The resulting solution was left for slow evaporation at room temperature. After about 3 weeks, suitable single crystals were obtained.

6.3.2.2. Synthesis of TMA·cinnamyl alcohol (2)

Similar to synthesis of **1**, cinnamyl alcohol (1.53g, 11.4 mmol) was added to a methanol solution (5 mL), of trimesic acid (0.3 g, 1.4 mmol). The mixture was stirred at room temperature for 48 hrs in a sealed scintillation vial. The resulting solution was left for slow evaporation at room temperature. After about 3 weeks, suitable single crystals were obtained.

6.4.Results and Discussions

6.4.1. Single crystal structure analysis

Our approach involved crystallization of trimesic acid in the presence of a guest molecule that might pack within the 14 Å channels. **TMA·α-terpineol** crystallized in space group *C*2/*c* to yield a porous framework. The primary intermolecular interactions were the robust C=O···H-O carboxylic acid dimers between molecules of TMA. As shown in (Figure 6-1a) α-terpineol as well as water and disordered methanol molecules occupy the pore. Additionally, H-bonding is observed between α-terpineol and water molecule via (α-terpineol) O···H-O(water) interaction. The molecules of TMA assemble into hexagonal

honeycomb layers with a 14.7 Å diameter pore channel (Figure 6-1b). The framework is stabilized by substantial face-to-face π-π interactions between the stacked layers of the framework (Figure 6-1c).

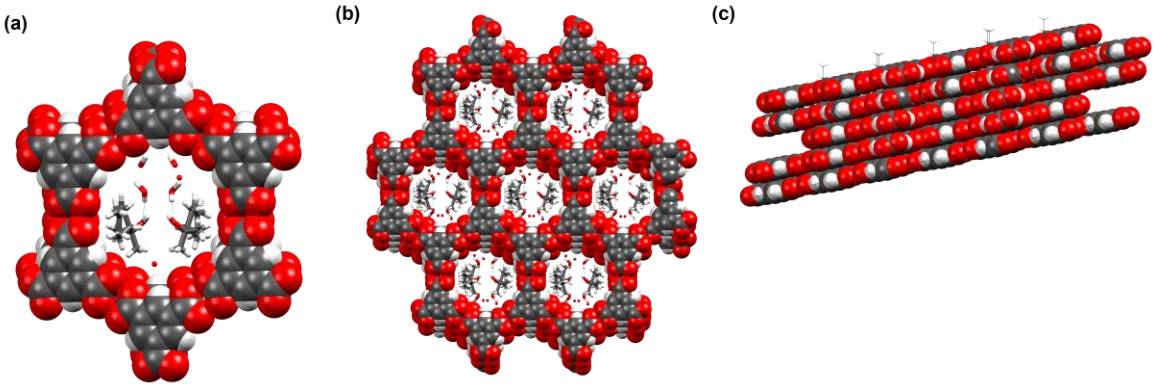

Figure 6-1 Single crystal structure of **TMA·*α*-terpineol** showing (a) HOF construction and physical encapsulation of guest moecules with no interaction to host (b) packing of the HOF into honeycomb network (c) π-πstacked layers of the framework.

TMA·cinnamyl alcohol crystallized in space group *Ia* to yield a porous framework. Interestingly, for **TMA·cinnamyl alcohol,** in addition to engaging in normal carboxylic acid dimers between only TMA molecules, the cinnamyl alcohol also hydrogen bonds to the carboxylic acid groups of TMA. In the crystal structure the C=O···H-O carboxylic acid dimers are present as well as (TMA)C=O···H-O (fragrance) and (fragrance) H-O···H-O(TMA) (Figure 6-2a). It is intriguing that the hexagonal backbone (Figure 6-2b) was sustained despite the incorporation of additional primary interactions where the fragrance molecule cinnamyl alcohol is involved in the H-bonding of the core framework.

Similar to the structure of **TMA·*α*-terpineol,** the framework is also stabilized by substantial face-to-face π-π interactions between the stacked layers of the framework (Figure 6-2c).

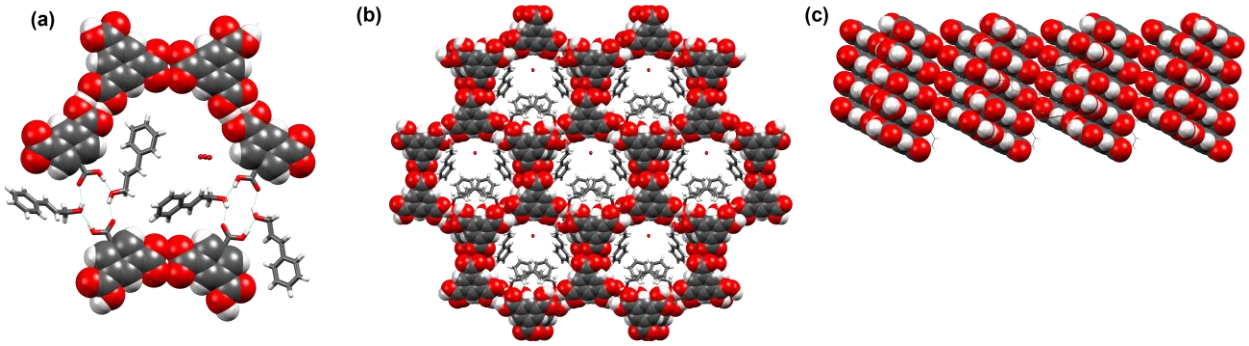

Figure 6-2 Single crystal structure of **TMA·cinnamyl alcohol** showing (a) H-bonding encapsulation with guest molecules H-bonding with the host molecules (b) packing of the HOF into a hexagonal framework (c) π-π stacking of the framework layers.

PLATON[33] software was used to compare void space of non-catenated hexagonally arranged porous polymorph of trimesic acid, δ-TMA with the **TMA·*α*-terpineol** and **TMA·cinnamyl alcohol**.[34] The assumption here was that availability of void space may be indicative of the probability of solvent/guest inclusion as shown by previous attempts at the prediction of solvent/guest inclusion.[35, 36] The % void space present in trimesic acid structure was calculated to be 50%. For **TMA·*α*-terpineol** the void space was 9.4% after fragrance and solvent uptake, while no void space was present after uptake for **TMA·cinnamyl alcohol**.

6.4.2. Thermogravimetric analysis

The TG curve of **TMA·α-terpineol** first shows three consecutive weight losses of 8.1% from 53 to 75 °C corresponding to the release of two methanol molecules (calculated, 9.5%). Another weight loss of 6.4% occurs in the 75-125 °C region corresponding to the release of two water molecules (calculated, 5.3%), and finally one more weight loss of 19.8% occurs in the 135–155 °C region, corresponding to the release of one α-terpineol molecule (calculated, 22.2%). The remaining host hydrogen bonding framework began to decompose upon further heating in the 295–330 °C region with a 65.7% weight loss, corresponding to two TMA molecules (calculated, 61%). (Figure 6-3).

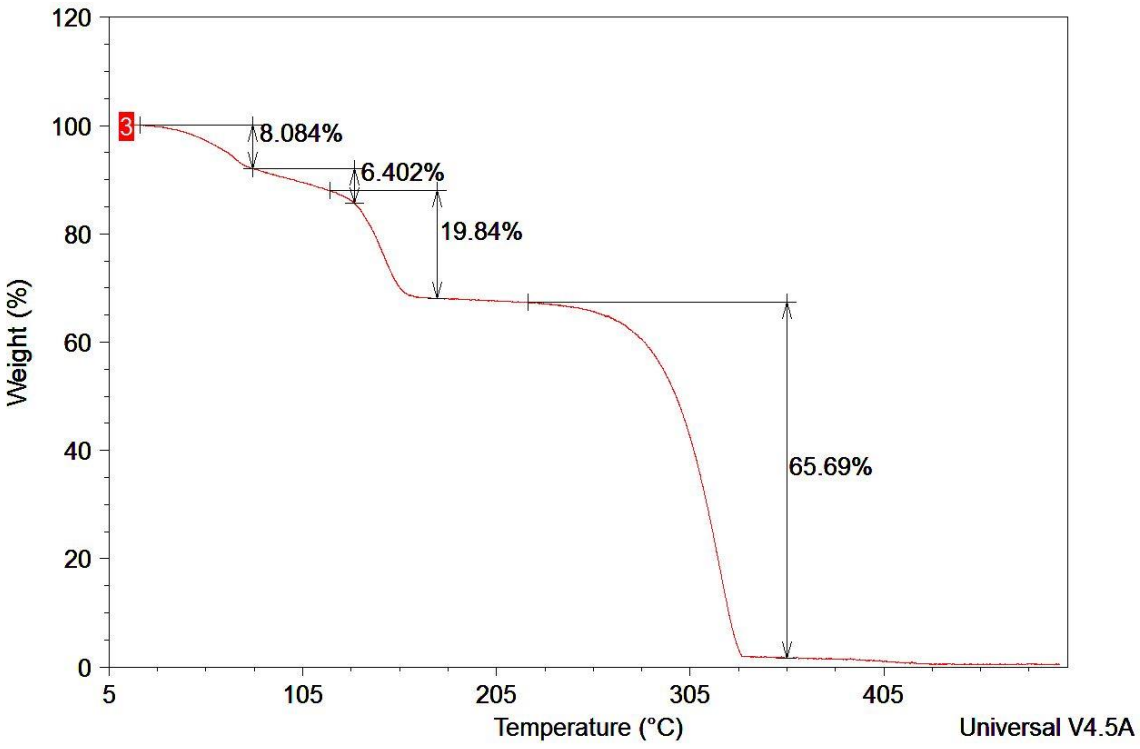

Figure 6-3 TGA analysis of **TMA·α-terpineol** showing successive weight loss of the methanol, water, and fragrance molecules.

The compound **TMA·cinnamyl alcohol** first shows two consecutive weight losses of 12.2% from 68 to 96 °C and 14.1% from 127 to 159 °C corresponding to the release of one water molecule and one cinnamyl alcohol molecule respectively. The temperature at which the weight loss starts is above the boiling point of methanol (65°C) which suggests the absence of methanol in the structure moiety. The remaining host hydrogen bonding framework began to decompose upon further heating in the 310–355 °C region with a 70.1% weight loss, corresponding to two TMA molecules (calculated, 69.5%) (Fig 6-4).

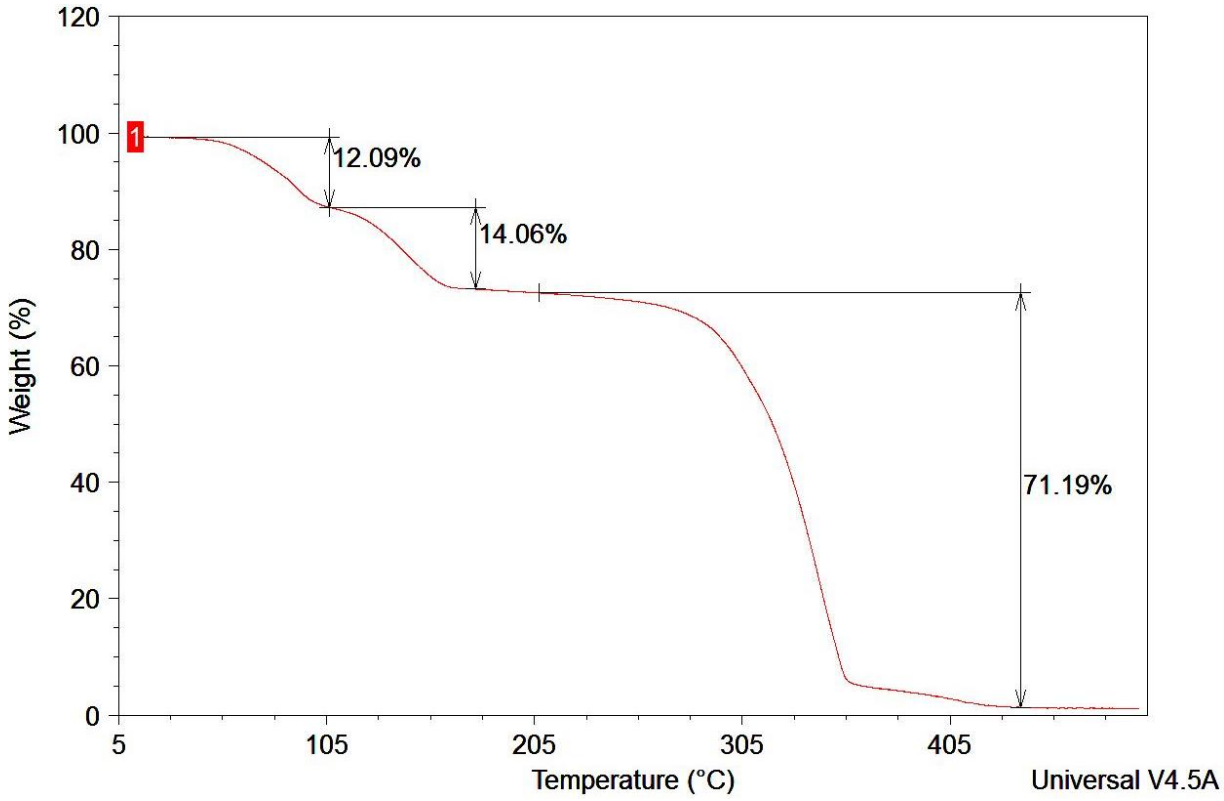

Figure 6-4 TGA analysis of **TMA·cinnamyl alcohol** showing consecutive weight loss of water and fragrance molecules.

6.4.3. Thermal stability analysis of the frameworks

Another crucial characteristic feature for good porous materials is thermal stability. To evaluate the thermal stability of our two-fragrance encapsulated HOFs, the materials were heated to temperatures just above the boiling point of the fragrances according to our TGA data. Since high crystallinity is one of the most important merit of HOFs we reasoned that if our frameworks are thermally stable then crystallinity of the frameworks should be retained upon heating the materials hence releasing the fragrance and solvents which all have boiling points substantially below the TMA melting point of >290°C. Figure 6-5 shows a comparison of the PXRD patterns: **TMA·α-terpineol** (grey), TMA (red) and heated **TMA·α-terpineol** (green). Upon heating the *as-synthesized* **TMA·α-terpineol** sample to 240°C, the α-terpineol and solvents are released from the pore. Most importantly, while the PXRD pattern of the heated **TMA·α-terpineol** is not the same as that of pure TMA, but the pattern shows that the heated materials retains crystallinity. This suggests that upon heating, the guest molecules inside the pore are released and our framework does not disintegrate which indicates that our HOF material is thermally stable.

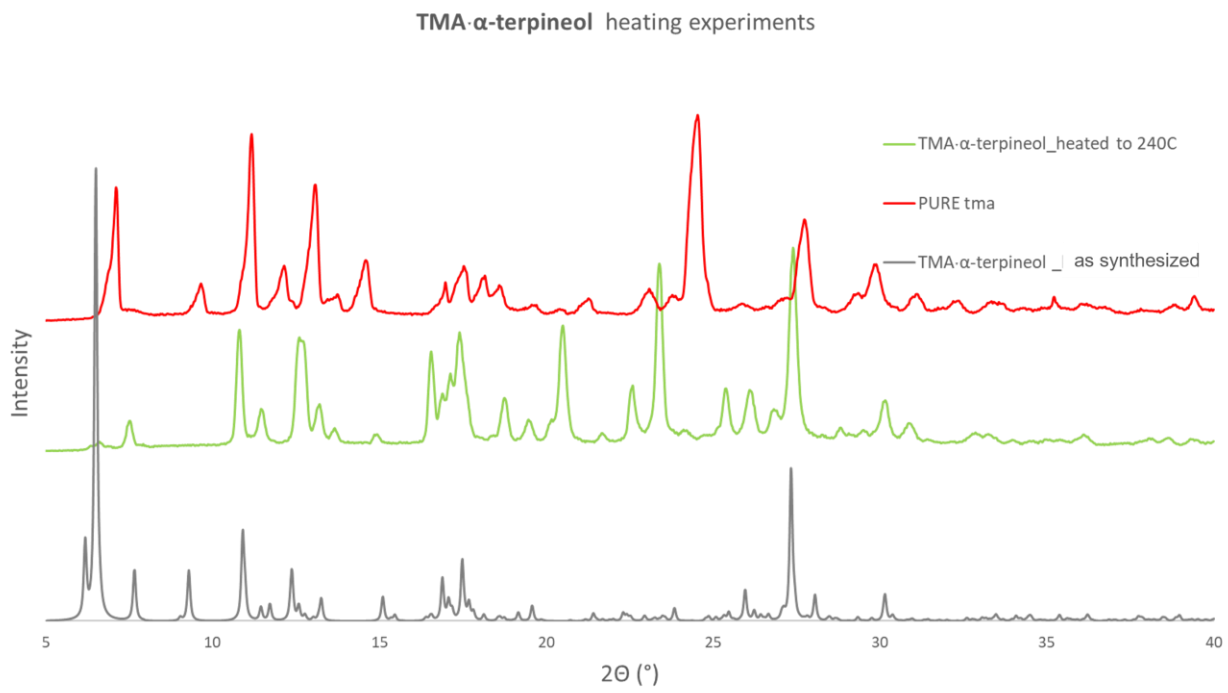

Figure 6-5 PXRD analysis showing the patterns of (red) TMA, (green) heated **TMA·*α*-terpineol** sample and (grey) the as-synthesized **TMA·*α*-terpineol** sample.

Figure 6-6 shows a comparison of the PXRD patterns: **TMA·cinnamyl alcohol** (grey), TMA (red) and heated **TMA·cinnamyl alcohol** (green). Upon heating the *as-synthesized* **TMA·cinnamyl** sample to 200°C, the cinnamyl alcohol and solvent molecule are released from the pore. Since the cinnamyl alcohol was involved in the primary interactions that held the framework together, It was fascinating to observe that the framework did not crumble with the release of the cinnamyl alcohol molecules. Instead, the PXRD pattern of the heated **TMA·cinnamyl alcohol** is similar to that of TMA. We postulate that upon heating, as the cinnamyl alcohol molecules are released, the neighboring TMA molecules recognize each other and aggregate to reform the hexagonal framework. The PXRD

patterns support that the heated material is still crystalline and that the pattern matches with that of TMA. The ability of the molecules to rearrange and maintain the framework after loss of the guest in the core is a clear advantage of the versatility of frameworks held together by non-covalent interactions especially compared to COFs which could have collapsed in such a case.

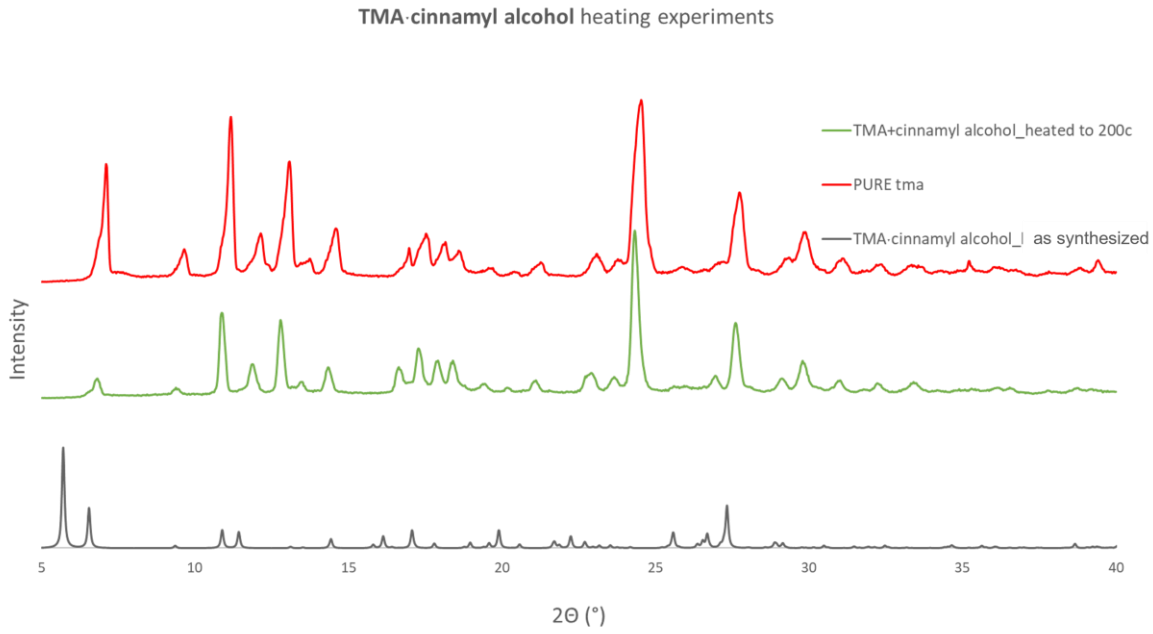

Figure 6-6 PXRD analysis showing the patterns of (red) TMA, (green) heated **TMA·cinnamyl alcohol**, and (grey) as-synthesized **TMA·cinnamyl alcohol** samples.

6.5. Conclusions

This chapter introduced hydrogen-bonded organic frameworks (HOFs) for the capture of high volatile-fragrances using crystallization techniques. The framework assembles *via*

predictable hydrogen bonding motifs, helping to further our ability to rationally design robust, porous networks. We have demonstrated that:

1. Trimesic acid as a backbone can successfully construct robust and porous framework.
2. The host trimesic acid and guest fragrances formed crystalline frameworks that were stabilized by carboxylic acid dimers, multiple π-π stacking and O-H···O hydrogen bonding interactions.
3. Physical encapsulation is an effective mode of encapsulating fragrance molecules as shown in the **TMA·α-terpineol** structure.
4. H-bonding is a plausible mode of encapsulation as proven by our **TMA·cinnamyl alcohol** framework.
5. TGA analysis is a reliable method for quantifying the guest molecules present in pore channels.
6. Our TMA-HOFs retain crystallinity after heating and release of the guest molecules.

The compounds presented here provide an opportunity to further design and construct host-guest supramolecular frameworks with desired structures. This study is proof of concept that HOFs are suitable systems and are complementary systems to MOFs and COFs.

6.6.References

1. Hu, J.; Liu, L.; Xie, Y.; Wu, L., Facile synthesis of thermal-responsive P(NIPAM-S)/SiO_2 hybrid hollow spheres and their controllable release properties for fragrance. *Polymer Chemistry* **2013,** *4* (11), 3293-3299.
2. Zhu, G. Y., Xiao, Z.B., Zhou, R.J., Yi, F.P, Fragrance and Flavor Microencapsulation Technology. *Advanced Materials* **2012,** *535-537*, 440-445.
3. Herrmann, A., Controlled Release of Volatiles under Mild Reaction Conditions: From Nature to Everyday Products. *Angewandte Chemie International Edition* **2007,** *46* (31), 5836-5863.
4. Wang, P.; Zhu, Y.; Yang, X.; Chen, A., Prolonged-release performance of perfume encapsulated by tailoring mesoporous silica spheres. *Flavour and Fragrance Journal* **2008,** *23* (1), 29-34.
5. Zhu, G. Y.; Xiao, Z. B.; Zhou, R. J.; Yi, F. P., Fragrance and Flavor Microencapsulation Technology. *Advanced Materials Research* **2012,** *535-537*, 440-445.
6. Tree-udom, T.; Wanichwecharungruang, S. P.; Seemork, J.; Arayachukeat, S., Fragrant chitosan nanospheres: Controlled release systems with physical and chemical barriers. *Carbohydrate Polymers* **2011,** *86* (4), 1602-1609.
7. Theisinger, S.; Schoeller, K.; Osborn, B.; Sarkar, M.; Landfester, K., Encapsulation of a Fragrance via Miniemulsion Polymerization for Temperature-Controlled Release. *Macromolecular Chemistry and Physics* **2009,** *210* (6), 411-420.
8. Hofmeister, I.; Landfester, K.; Taden, A., pH-Sensitive Nanocapsules with Barrier Properties: Fragrance Encapsulation and Controlled Release. *Macromolecules* **2014,** *47* (16), 5768-5773.
9. Bollhorst, T.; Rezwan, K.; Maas, M., Colloidal capsules: nano- and microcapsules with colloidal particle shells. *Chemical Society Reviews* **2017,** *46* (8), 2091-2126.
10. Dedecker, K.; Dumas, E.; Lavédrine, B.; Steunou, N.; Serre, C., 5 - Metal-organic frameworks for the capture of volatile organic compounds and toxic chemicals. In *Metal-Organic Frameworks (MOFs) for Environmental Applications*, Ghosh, S. K., Ed. Elsevier: 2019; pp 141-178.
11. Yang, Y.; Burke, N.; Ali, S.; Huang, S.; Lim, S.; Zhu, Y., Experimental studies of hydrocarbon separation on zeolites, activated carbons and MOFs for applications in natural gas processing. *RSC Advances* **2017,** *7* (21), 12629-12638.
12. Samarakoon, K. P.; Satterfield, C. S.; McCoy, M. C.; Pivaral-Urbina, D. A.; Islamoglu, T.; Day, V. W.; Gadzikwa, T., Uniform, Binary Functionalization of a Metal–Organic Framework Material. *Inorganic Chemistry* **2019,** *58* (14), 8906-8909.
13. Wang, H.; Lashkari, E.; Lim, H.; Zheng, C.; Emge, T. J.; Gong, Q.; Yam, K.; Li, J., The moisture-triggered controlled release of a natural food preservative from a microporous metal–organic framework. *Chemical Communications* **2016,** *52* (10), 2129-2132.

14. Vaughn, J.; Wu, H.; Efremovska, B.; Olson, D. H.; Mattai, J.; Ortiz, C.; Puchalski, A.; Li, J.; Pan, L., Encapsulated recyclable porous materials: an effective moisture-triggered fragrance release system. *Chemical Communications* **2013,** *49* (51), 5724-5726.
15. Diercks, C. S.; Yaghi, O. M., The atom, the molecule, and the covalent organic framework. *Science* **2017,** *355* (6328), eaal1585.
16. Kamionka, M.; Breuil, P.; Pijolat, C., Calibration of a multivariate gas sensing device for atmospheric pollution measurement. *Sensors and Actuators B: Chemical* **2006,** *118* (1), 323-327.
17. Haase, F.; Lotsch, B. V., Solving the COF trilemma: towards crystalline, stable and functional covalent organic frameworks. *Chemical Society Reviews* **2020,** *49* (23), 8469-8500.
18. Furukawa, H.; Cordova, K. E.; O'Keeffe, M.; Yaghi, O. M., The Chemistry and Applications of Metal-Organic Frameworks. *Science* **2013,** *341* (6149), 1230444.
19. Colson, J. W.; Dichtel, W. R., Rationally synthesized two-dimensional polymers. *Nature Chemistry* **2013,** *5* (6), 453-465.
20. Hisaki, I.; Xin, C.; Takahashi, K.; Nakamura, T., Designing Hydrogen-Bonded Organic Frameworks (HOFs) with Permanent Porosity. *Angewandte Chemie International Edition* **2019,** *58* (33), 11160-11170.
21. Desiraju, G. R., C–H···O and other weak hydrogen bonds. From crystal engineering to virtual screening. *Chemical Communications* **2005,** (24), 2995-3001.
22. Gunaratne, H. Q. N.; Nockemann, P.; Seddon, K. R., Pro-fragrant ionic liquids with stable hemiacetal motifs: water-triggered release of fragrances. *Chemical Communications* **2015,** *51* (21), 4455-4457.
23. Simard, M.; Su, D.; Wuest, J. D., Use of hydrogen bonds to control molecular aggregation. Self-assembly of three-dimensional networks with large chambers. *Journal of the American Chemical Society* **1991,** *113* (12), 4696-4698.
24. Li, P.; He, Y.; Zhao, Y.; Weng, L.; Wang, H.; Krishna, R.; Wu, H.; Zhou, W.; O'Keeffe, M.; Han, Y.; Chen, B., A Rod-Packing Microporous Hydrogen-Bonded Organic Framework for Highly Selective Separation of C_2H_2/CO_2 at Room Temperature. *Angewandte Chemie International Edition* **2015,** *54* (2), 574-577.
25. Wang, H.; Li, B.; Wu, H.; Hu, T.-L.; Yao, Z.; Zhou, W.; Xiang, S.; Chen, B., A Flexible Microporous Hydrogen-Bonded Organic Framework for Gas Sorption and Separation. *Journal of the American Chemical Society* **2015,** *137* (31), 9963-9970.
26. Huang, Y.-G.; Shiota, Y.; Wu, M.-Y.; Su, S.-Q.; Yao, Z.-S.; Kang, S.; Kanegawa, S.; Li, G.-L.; Wu, S.-Q.; Kamachi, T.; Yoshizawa, K.; Ariga, K.; Hong, M.-C.; Sato, O., Superior thermoelasticity and shape-memory nanopores in a porous supramolecular organic framework. *Nature Communications* **2016,** *7* (1), 11564.
27. Lü, J.; Perez-Krap, C.; Suyetin, M.; Alsmail, N. H.; Yan, Y.; Yang, S.; Lewis, W.; Bichoutskaia, E.; Tang, C. C.; Blake, A. J.; Cao, R.; Schröder, M., A Robust Binary Supramolecular Organic Framework (SOF) with High CO2 Adsorption and Selectivity. *Journal of the American Chemical Society* **2014,** *136* (37), 12828-12831.

28. Kobayashi, K.; Shirasaka, T.; Horn, E.; Furukawa, N., Two-dimensional hexagonal hydrogen-bonded network with triangle-like large cavities: hexakis(4-carboxyphenyl)benzene. *Tetrahedron Letters* **2000,** *41* (1), 89-93.
29. Yin, Q.; Zhao, P.; Sa, R.-J.; Chen, G.-C.; Lü, J.; Liu, T.-F.; Cao, R., An Ultra-Robust and Crystalline Redeemable Hydrogen-Bonded Organic Framework for Synergistic Chemo-Photodynamic Therapy. *Angewandte Chemie International Edition* **2018,** *57* (26), 7691-7696.
30. Hisaki, I.; Suzuki, Y.; Gomez, E.; Ji, Q.; Tohnai, N.; Nakamura, T.; Douhal, A., Acid Responsive Hydrogen-Bonded Organic Frameworks. *Journal of the American Chemical Society* **2019,** *141* (5), 2111-2121.
31. Dmitriev, A.; Lin, N.; Weckesser, J.; Barth, J. V.; Kern, K., Supramolecular Assemblies of Trimesic Acid on a Cu(100) Surface. *The Journal of Physical Chemistry B* **2002,** *106* (27), 6907-6912.
32. Chui, S. S.-Y.; Lo, S. M.-F.; Charmant, J. P. H.; Orpen, A. G.; Williams, I. D., A Chemically Functionalizable Nanoporous Material *Science* **1999,** *283* (5405), 1148-1150.
33. Spek, A., Structure validation in chemical crystallography. *Acta Crystallographica Section D* **2009,** *65* (2), 148-155.
34. Cui, P.; McMahon, D. P.; Spackman, P. R.; Alston, B. M.; Little, M. A.; Day, G. M.; Cooper, A. I., Mining predicted crystal structure landscapes with high throughput crystallisation: old molecules, new insights. *Chemical Science* **2019,** *10* (43), 9988-9997.
35. Braun, D. E.; Griesser, U. J., Why Do Hydrates (Solvates) Form in Small Neutral Organic Molecules? Exploring the Crystal Form Landscapes of the Alkaloids Brucine and Strychnine. *Crystal Growth & Design* **2016,** *16* (11), 6405-6418.
36. Mohamed, S.; Karothu, D. P.; Naumov, P., Using crystal structure prediction to rationalize the hydration propensities of substituted adamantane hydrochloride salts. *Acta Crystallographica Section B* **2016,** *72* (4), 551-561.

Chapter 7 - Conclusions and Outlook

The work presented in this dissertation outlines the importance of understanding structure for the design of materials with controlled structure-property relationship. It is important to understand how intermolecular interactions and packing influence their physiochemical properties. Chapters 2, 3, and 4 demonstrate the versatility of hydrogen and halogen bond as tools for driving co-crystallization.

Increasing the molecular chain length was found to affect the type of intermolecular interactions that were present. The N–H···S=C dimer was found to be a reliable synthon for higher chain length targets (pentyl and hexyl), while the N–H···$N_{thiazole}$ dominated for shorter chain length targets. As shown in Chapter 2, adding a methyl substituent to the thiazole ring does not seem to impact packing in the target structures with shorter alkyl chain length (methyl-isobutyl). However, for targets containing the alkyl chain length (pentyl and hexyl), the presence of methyl substituent clearly results in a changed packing behavior. This underscores how synthon strength and molecular shape both control packing. It is worthwhile to enlarge the target molecule library by adding a variety of substituents such as choro-, nitro and investigate how their presence would affect intermolecular interactions and packing.

In Chapter 3, the structural influence of hydrogen bonding on structure was explored in diethyl *N*,*N*′-[(1,4-phenylenedicarbamothioyl)bis(carbamate)] (**14thiol**) and its ability to form multicomponent crystals. Co-crystallization experiments were conducted using pyridine-based co-formers and two polymorphs, one dioxane solvate, three co-crystals and one co-crystal solvate (THF) were obtained. In addition, conformational analysis showed that the target was able to adopt three primary molecular conformations in the several new multicomponent solid forms. The use of Hirshfeld surface analysis gave insights into the nature of interactions, and it revealed that the high acceptor ability in the co-formers led to the increase in H-bonding interactions (N-H---N) and a decrease in (O---H) contacts in **14thiol** co-crystals. Since this target molecule has demonstrated the ability to form multicomponent crystals, further experiments could be conducted such as setting up cocrystallizations with various solvents as well as using other co-formers like carboxylic acids and halogen bond donors.

Chapter 4 investigated a halogen bonded system for binding preference in the presence of multiple intermolecular interaction sites in three R-*N*-[(3-pyridinylamino) thioxomethyl] carbamates (R= methyl, ethyl, and isobutyl) with fluoroiodobenzenes. Five co-crystals and one co-crystal solvate were obtained. The use of MEP surfaces provided a means for ranking the relative strength of the binding sites (Npyr > C=S > C=O) in order to predict the dominant interactions. The N-H---H hydrogen bond (parent synthon) was

replaced by I---Npyr in 3/6 cases by I---C=S in 4/6 cases and by I---O=C in one case. Interestingly, in two cases, the I---C=S halogen bond coexisted with I---Npyr and I---O=C halogen bonds. Overall, it was found that in such a complex system with various binding options it is challenging to establish binding preference. Halogen-bond donors co-formers proved to be structurally competitive for acceptor sites even in the presence of strong hydrogen-bond donors. It would be interesting to use a set of activated halogen bond donors and study what binding preference is established with stronger donors.

Chapter 5 examined structure property correlations in order to influence thermal expansion (TE) behavior in solid state materials. Intermolecular interactions, molecular packing, and the effect of varying molecular dimensionality (di->tri->tetra) carbamate on TE were discussed. Five target molecules were designed and synthesized: three fluorinated dicarbamates with varying chain lengths, one tri-carbamate and one tetra-carbamate. A series of detailed single crystal structural determinations at 20-K intervals (150-250) allowed us to analyze the thermal expansion at a molecular level. The specific influence of intermolecular interactions was explored based on interaction energies (IEs) using energy framework analysis which confirmed that IEs were highest along the direction of the robust N-H---O=C interactions which subsequently restricted thermal expansion along those directions. Further work could be done in this project by designing

an aromatic system using the same hypothesis to investigate whether the pattern of TE is transferrable from one system to the other.

Finally, in Chapter 6, applications of crystal engineering were explored using hydrogen-bonded organic frameworks (HOF) as molecular containers/hosts for volatile fragrance compounds (cinnamyl alcohol and α-terpineol). In the first example, the HOF successfully captured α-terpineol in its pores via physical encapsulation, as indicated by thermal gravimetric analysis. In the second example, the HOF also captured cinnamyl alcohol by way of H-bonding to the volatile guest compound. It was found that this supramolecular framework, based on trimesic acid, is very suitable for capture and slow release of volatile compounds. Further work could be done for this project, for example the backbone library could be extended with a bigger pore size in order to have more space to accommodate volatile quests such as camphor, menthol and isoborneol.

All in all, the research discussed in this thesis emphasizes the importance of understanding the fundamental work such as intermolecular interaction and assembly molecules in the lattice. Subsequently, this knowledge is crucial for understanding structure-property relationships which ultimately influence the application of materials.

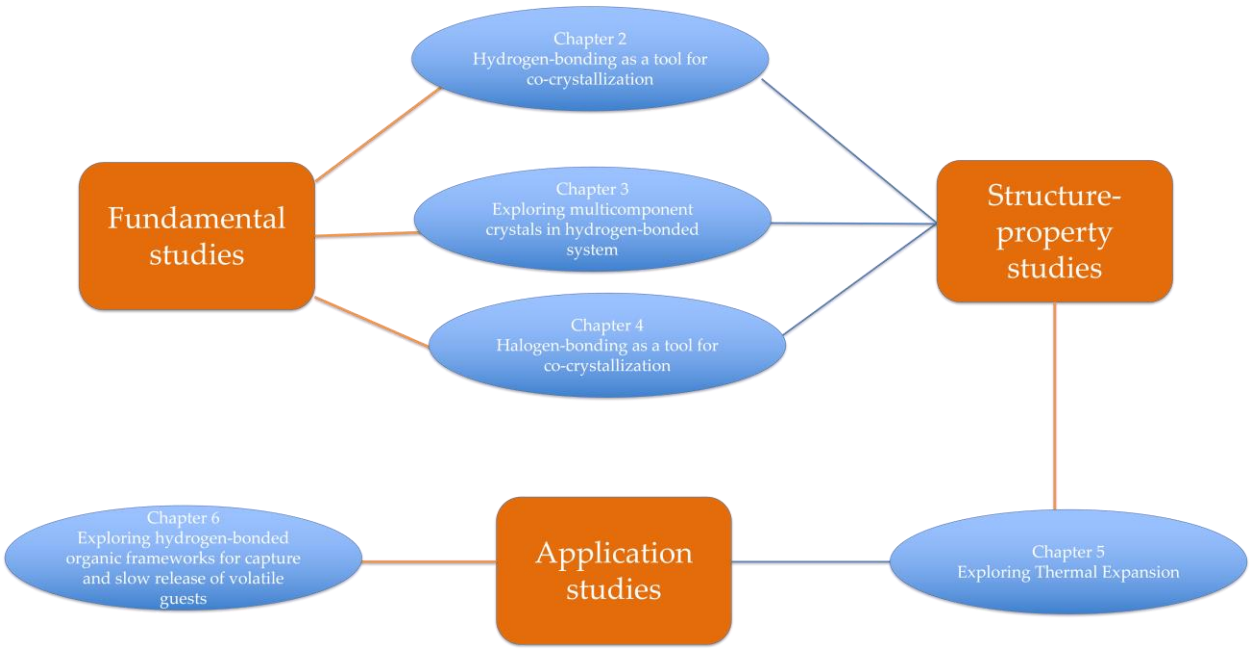

Scheme 7-1 Summary of research discussed in this thesis.

Appendix A - Additional information for Chapter 1

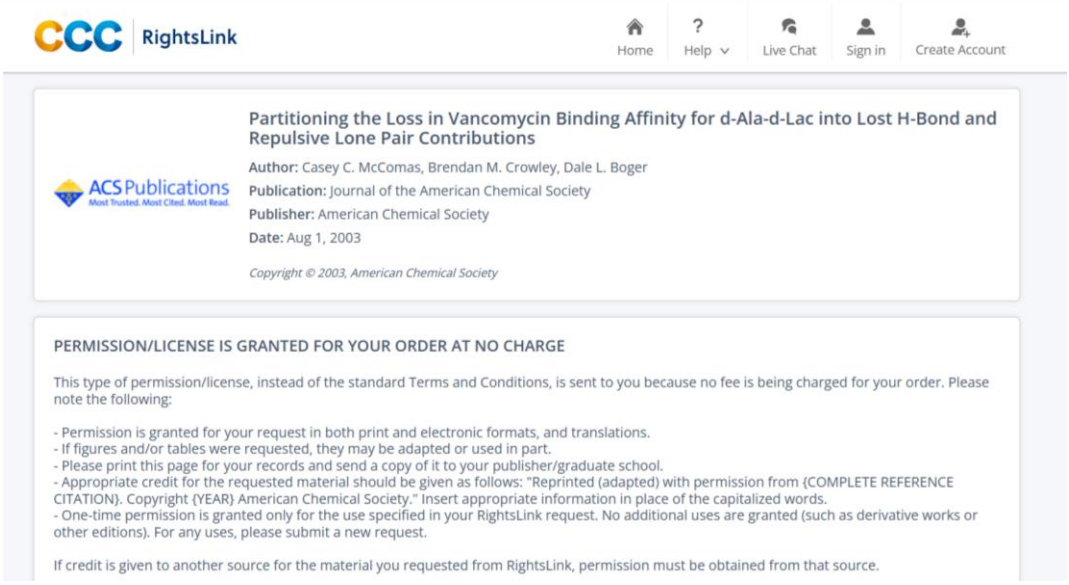

Figure A- 1 Copyrights permission for Chapter 1.

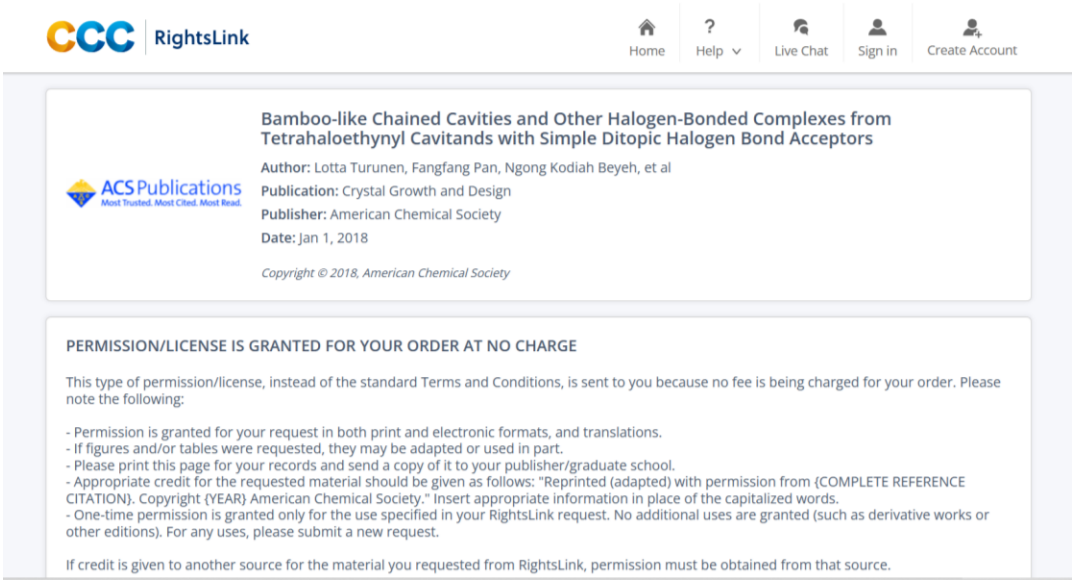

Figure A- 2 Copyrights permission for Chapter 1.

Appendix B- Additional information for Chapter 2

Table B- 1 Crystallographic information for TZ1 -TZ5

Identification code	exp_322	exp_300	exp_319_auto	exp_686	exp_685a
Empirical formula	$C_6H_7N_3O_2S_2$	$C_7H_9N_3O_2S_2$	$C_9H_{13}N_3O_2S_2$	$C_{10}H_{15}N_3O_2S_2$	$C_{11}H_{17}N_3O_2S_2$
Formula weight	217.27	231.29	259.34	273.37	287.39
Temperature/K	220.00(10)	200(2)	220.00(10)	200.00(10)	249.99(10)
Crystal system	monoclinic	monoclinic	monoclinic	orthorhombic	monoclinic
Space group	$P2_1/n$	$P2_1/c$	$P2_1/c$	$Pca2_1$	$P2_1/c$
a/Å	14.82205(19)	11.8602(3)	11.9310(2)	8.05620(10)	8.1539(2)
b/Å	3.97176(6)	8.57369(13)	9.0277(2)	13.9315(2)	11.2824(2)
c/Å	15.43494(19)	11.4064(3)	11.5472(2)	11.54940(10)	31.7937(16)
α/°	90	90	90	90	90
β/°	98.6587(12)	118.170(3)	92.276(2)	90	91.027(3)
γ/°	90	90	90	90	90
Volume/Å^3	898.29(2)	1022.48(4)	1242.76(4)	1296.25(3)	2924.41(18)
Z	4	4	4	4	8
ρ_{calc}g/cm^3	1.607	1.502	1.386	1.401	1.306
μ/mm^{-1}	5.170	4.578	3.825	3.696	3.301
F(000)	448.0	480.0	544.0	576.0	1216.0
Crystal size/mm^3	0.266 × 0.152 × 0.026	? × ? × ?	0.15 × 0.05 × 0.02	0.12 × 0.01 × 0.01	0.14 × 0.1 × 0.03
Radiation	Cu Kα (λ = 1.54184)	CuKα (λ = 1.54184)	Cu Kα (λ = 1.54184)	Cu Kα (λ = 1.54184)	Cu Kα (λ = 1.54184)
2Θ range for data collection/°	7.71 to 154.926	8.458 to 154.612	7.416 to 155.708	6.344 to 159.772	5.56 to 133.182
Index ranges	-18 ≤ h ≤ 18, -4 ≤ k ≤ 5, -13 ≤ l ≤ 19	-15 ≤ h ≤ 14, -10 ≤ k ≤ 9, -14 ≤ l ≤ 14	-15 ≤ h ≤ 12, -11 ≤ k ≤ 11, -14 ≤ l ≤ 14	-10 ≤ h ≤ 10, -17 ≤ k ≤ 17, -14 ≤ l ≤ 11	-9 ≤ h ≤ 9, -13 ≤ k ≤ 13, -35 ≤ l ≤ 37
Reflections collected	9172	8602	12223	11668	6769
Independent reflections	1890 [R_{int} = 0.0197, R_{sigma} = 0.0172]	2136 [R_{int} = 0.0212, R_{sigma} = 0.0188]	2608 [R_{int} = 0.0233, R_{sigma} = 0.0183]	2313 [R_{int} = 0.0268, R_{sigma} = 0.0232]	6769 [R_{int} = ?, R_{sigma} = 0.0199]
Data/restraints/parameters	1890/0/120	2136/0/129	2608/39/201	2313/1/156	6769/34/357
Goodness-of-fit on F^2	1.057	1.108	1.067	1.058	1.060
Final R indexes [I>=2σ (I)]	R_1 = 0.0295, wR_2 = 0.0879	R_1 = 0.0255, wR_2 = 0.0715	R_1 = 0.0324, wR_2 = 0.0876	R_1 = 0.0233, wR_2 = 0.0629	R_1 = 0.0804, wR_2 = 0.2361
Final R indexes [all data]	R_1 = 0.0303, wR_2 = 0.0890	R_1 = 0.0274, wR_2 = 0.0724	R_1 = 0.0344, wR_2 = 0.0889	R_1 = 0.0238, wR_2 = 0.0632	R_1 = 0.0988, wR_2 = 0.2526
Largest diff. peak/hole / e Å^{-3}	0.32/-0.23	0.24/-0.22	0.24/-0.24	0.18/-0.18	0.50/-0.43

Table B- 2 Crystallographic information for TZ6 -TZ10

Identification code	exp_561	exp_562	exp_603	exp_694a	exp_693
Empirical formula	$C_8H_{13}N_3O_3S_2$	$C_8H_{11}N_3O_2S_2$	$C_{10}H_{15}N_3O_2S_2$	$C_{11}H_{17}N_3O_2S_2$	$C_{12}H_{19}N_3O_2S_2$
Formula weight	263.33	245.32	273.37	287.39	301.42
Temperature/K	150.00(10)	150.00(10)	180.00(10)	200.00(10)	200.00(10)
Crystal system	triclinic	monoclinic	monoclinic	monoclinic	monoclinic
Space group	P-1	$P2_1/c$	$P2_1/c$	C2/c	C2/c
a/Å	7.9248(4)	11.6611(5)	11.64354(12)	35.8636(11)	42.0263(7)
b/Å	8.0624(3)	9.3875(3)	9.74677(9)	4.21420(9)	4.22480(10)
c/Å	10.3043(4)	11.0348(5)	11.51756(10)	19.3986(6)	19.2002(4)
α/°	88.516(3)	90	90	90	90
β/°	89.911(4)	111.675(5)	90.6266(9)	109.124(4)	116.840(2)
γ/°	66.137(4)	90	90	90	90
Volume/Å^3	601.86(5)	1122.55(9)	1307.01(2)	2770.02(15)	3041.79(12)
Z	2	4	4	8	8
ρ_{calc}g/cm^3	1.453	1.452	1.389	1.378	1.316
μ/mm^{-1}	0.439	0.458	3.665	3.485	3.198
F(000)	276.0	512.0	576.0	1216.0	1280.0
Crystal size/mm^3	0.112 × 0.086 × 0.054	0.16 × 0.11 × 0.05	0.153 × 0.083 × 0.059	0.112 × 0.061 × 0.007	0.11 × 0.084 × 0.05
Radiation	Mo Kα (λ = 0.71073)	Mo Kα (λ = 0.71073)	Cu Kα (λ = 1.54184)	Cu Kα (λ = 1.54184)	Cu Kα (λ = 1.54184)
2Θ range for data collection/°	5.528 to 60.482	5.742 to 63.138	7.594 to 159.394	5.216 to 144.22	9.212 to 159.826
Index ranges	-10 ≤ h ≤ 10, -11 ≤ k ≤ 10, -13 ≤ l ≤ 10	-16 ≤ h ≤ 15, -13 ≤ k ≤ 13, -15 ≤ l ≤ 13	-14 ≤ h ≤ 14, -12 ≤ k ≤ 12, -9 ≤ l ≤ 14	-44 ≤ h ≤ 43, -5 ≤ k ≤ 3, -23 ≤ l ≤ 23	-52 ≤ h ≤ 48, -5 ≤ k ≤ 5, -24 ≤ l ≤ 24
Reflections collected	7156	10477	12011	18278	18836
Independent reflections	2944 [R_{int} = 0.0220, R_{sigma} = 0.0287]	3095 [R_{int} = 0.0285, R_{sigma} = 0.0294]	2798 [R_{int} = 0.0250, R_{sigma} = 0.0202]	2682 [R_{int} = 0.0569, R_{sigma} = 0.0405]	3257 [R_{int} = 0.0371, R_{sigma} = 0.0283]
Data/restraints /parameters	2944/0/157	3095/0/146	2798/6/195	2682/0/173	3257/0/182
Goodness-of-fit on F^2	1.049	1.067	1.090	1.102	1.059
Final R indexes [I>=2σ (I)]	R_1 = 0.0349, wR_2 = 0.0927	R_1 = 0.0310, wR_2 = 0.0788	R_1 = 0.0290, wR_2 = 0.0786	R_1 = 0.0519, wR_2 = 0.1411	R_1 = 0.0384, wR_2 = 0.1053
Final R indexes [all data]	R_1 = 0.0426, wR_2 = 0.0968	R_1 = 0.0382, wR_2 = 0.0822	R_1 = 0.0305, wR_2 = 0.0800	R_1 = 0.0608, wR_2 = 0.1468	R_1 = 0.0426, wR_2 = 0.1086
Largest diff. peak/hole / e Å^{-3}	0.54/-0.20	0.34/-0.40	0.28/-0.32	0.78/-0.28	0.45/-0.28

Appendix C – Additional Information for Chapter 4

Table C- 1 Crystallographic data for the targets

Compounds	**A1**	**A3**
Identification code	exp_231	Exp_334
Molecular formula	$C_8H_9N_3O_2S$	$C_{11}H_{15}N_3O_2S$
Formula weight (g mol^{-1})	211.24	253.32
Crystal system	orthorhombic	triclinic
Space group (No.)	*Fdd2*	*P- 1* (No. 2)
a (Å)	28.61372(17)	9.5250(3)
b (Å)	19.21403(12)	10.2023(2)
c (Å)	6.92761(4)	14.3104(2)
α (°)	90	73.7596(18)
β (°)	90	78.554(2)
γ (°)	90	78.444(2)
V (Å^3)	3808.70(4)	1293.01(6)
Z	16	4
ϱ_{calc} (g cm^{-3})	1.474	1.301
μ (Cu Kα) (mm^{-1})	2.866	2.195
F (000)	1760.0	536.0
Crystal size (mm)	0.328 × 0.231 × 0.111	0.150 x 0.050 x 0.020
Temperature (K)	200 (10)	140 (2)
Radiation (Å)	CuKα, 1.54184	CuKα, 1.54174
Theta range for data collection	5.547 to 77.019°	3.254 to 77.577°
Index ranges	-35 ≤ h ≤ 36, -23 ≤ k ≤ 23, -8 ≤ l ≤ 8	-11<=h<=12, -12<=k<=12, -18<=l<=16
Final R indices [I>2.0 σ(I)]	R_1=0.0225, wR_2=0.0645	R_1=0.0524, wR_2=0.1537
Final R indices [all data]	R_1=0.0225, wR_2=0.0645	R_1=0.0577, wR_2= 0.1577
Tot ref., uniq. ref, R (int)	16723, 1972, 0.0181	22321, 5358,0.0438
Max. and min. transmission	1.000 and 0.265	1.00000 and 0.74851
Data/restraints/parameters	1972/1/137	5358 / 1 / 322
Goodness-of-fit on F^2	1.072	1.038
Largest diff. peak/hole (e. Å^{-3})	0.192/-0.246	0.688/-0.717

Table C- 2 Crystallographic information of co-crystals obtained.

Compounds	**A1·D1**	**$(A2)_2$·D1**	**A3·D1**	**$(A1)_2$·D2**	**A2·D2**	**$(A3)_2$·D2**
Identification code	exp_335c	exp_248	exp_308	exp_363	exp_351	Exp_393
Empirical formula	$C_{14}F_3\ I_3\ H_9\ N_3\ O_2\ S$	$C_{12}H_{11}F_{1.5}I_{1.5}N_3O_2S$	$C_{17}F_3\ I_3\ H_{15}N_3\ O_2\ S$	$C_{12}F_2\ Cl_3I\ H_{10}N_3\ O_2\ S$	$C_{15}F_4\ I_2\ H_{11}N_3\ O_2\ S$	$C_{14}F_2\ IH_{15}N_3\ O_2\ S$
Formula weight (g mol^{-1})	721.00	480.15	763.08	531.54	627.13	454.25
Crystal system	monoclinic	orthorhombic	triclinic	monoclinic	monoclinic	monoclinic
Space group (No.)	*$P2_1/c$*	*Pnna*	*P- 1* (No. 2)	*$P2_1/c$*	*$P2_1/c$*	*$P2_1/c$*
a (Å)	4.3912(3)	17.4398(3)	9.19100(10)	4.20680(10)	4.40696(4)	19.6991(9)
b (Å)	14.6099(10)	35.2133(6)	11.04700(10)	26.0337(5)	27.4127(3)	4.78474(13)
c (Å)	15.3389(9)	5.09340(10)	12.41600(10)	15.3735(3)	15.48356(14)	20.6316(10)
α (°)	90	90	64.5040(10)	90	90	90
β (°)	96.621(6)	90	88.3510(10)	94.498	91.4598(9)	116.983(6)
γ (°)	90	90	79.9240(10)	90	90	90
V ($Å^3$)	977.50(11)	3127.92(10)	1118.78(2)	1678.50(6)	1869.91(3)	1732.94(15)
Z	2	8	2	4	4	4
ρ_{calc} (g cm^{-3})	2.450	2.039	2.265	2.103	2.228	1.741
μ (Cu Kα) (mm^{-1})	4.945	25.315	34.185	20.875	27.990	15.941
F (000)	664	1832.0	712	1028	1184	892
Crystal size (mm)	0.16 x 0.01 x 0.01	0.155 × 0.06 × 0.035	0.159 x 0.108 x 0.059	0.121 x 0.013 x 0.01	0.098 x 0.052 x 0.033	0.255 x 0.031 x 0.022
Temperature (K)	140.00(10)	170.00(10)	130.00(10)	139.7(6)	140.00(10)	200.00(10)
Radiation (Å)	CuKα, 1.54184	CuKα, 1.54184	CuKα, 1.54184	CuKα, 1.54184	CuKα, 1.54184	CuKα, 1.54184
Theta range for data collection/°	2.674 to 30.814	2.510 to 77.122	3.950 to 77.463	4.457 to 77.733	3.224 to 77.545	2.517 to 77.810
Index ranges	-5<=h<=5, -20<=k<=20, -19<=l<=21	-21 ≤ h ≤ 16, -44 ≤ k≤ 39, -6 ≤ l ≤ 6	-11<=h<=11, -13<=k<=13, -15<=l<=15	-5<=h<=3, -32<=k<=32, -19<=l<=19	-5<=h<=5, -33<=k<=34, -18<=l<=19	-24<=h<=24, -6<=k<=4, -26<=l<=25
Final R indices [I>2.0 σ(I)]	R_1=0.0439, wR_2=0.0439	R_1 = 0.0213 wR_2 = 0.0598	R_1=0.0237 wR_2= 0.0648	R_1=0.0403 wR_2= 0.1071	R_1=0.0198 wR_2= 0.0511	R_1=0.0517 wR_2= 0.1312
Final R indices [all data]	R_1=0.0514 wR_2=0.1130	R_1 = 0.0220 wR_2 = 0.0603	R_1= 0.0239 wR_2= 0.0650	R_1=0.0417 wR_2= 0.1082	R_1=0.0203 wR_2= 0.0515	R_1=0.0575 wR_2= 0.1344
Tot ref., uniq. ref, R (int)	15121, 4704, 0.0596	17973, 3307,0.0256	42499, 4731, 0.0493	26685, 3561, 0.0459	22839, 4000, 0.47941	18918, 3609, 0.0625
Max. and min. transmission	1.00000 and 0.60523	1.00000 and 0.50257	1.00000 and 0.22072	0.920 and 0.327	1.00000 and 0.47941	1.000 and 0.408
Data/restraints/ parameters	4704 / 2 / 236	3307/0/193	4731 / 0 / 265	3561/142/262	4000 / 0 / 246	3609 / 0 / 210
Goodness-of-fit	1.006	1.062	1.050	1.100	1.047	1.118
Largest diff. peak/hole (e. $Å^{-3}$)	1.309/-1.013	0.664/-1.096	1.165/-1.053	1.206/-0.929	0.933/-0.945	1.210/-1.471

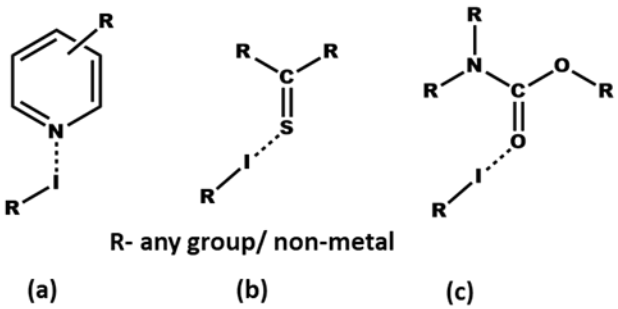

Figure C- 1 Contact descriptor used for CSD search (a) I···Npyr contact, (b) I···S=C contact, and (c) I···O=C contact.

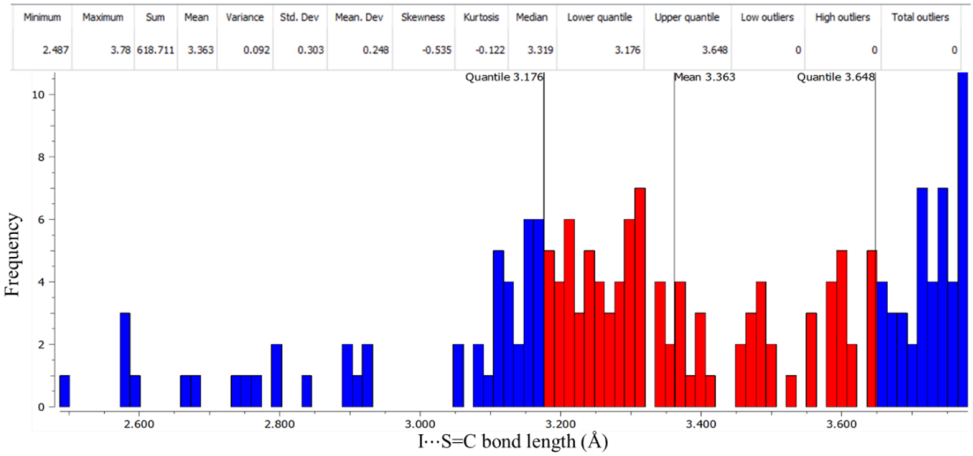

Figure C- 2 Histogram showing bond length against frequency for I···S=C halogen bond.

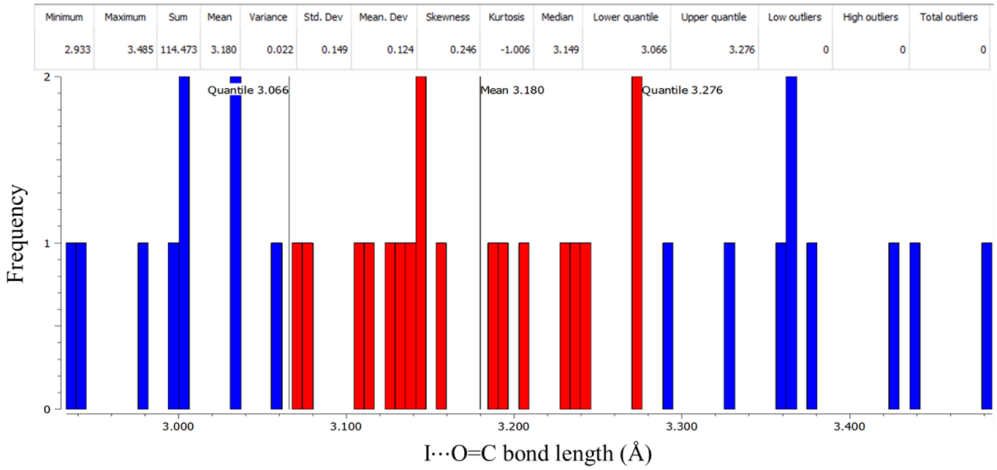

Figure C- 3 Histogram showing bond length against frequency for I···O=C halogen bond.